Control of Cavity Acoustics by Surface Waviness In Landing Configurations

By

BELKALLOUCHE ABDERRAHMANE

Institute of Aeronautics and Space Studies
UNIVERSITY OF BLIDA 1

DOCTOR OF PHILOSOPHY
AERONAUTICAL SCIENCE

Jury Member:

BOUKRAA Salah	Professor, USD Blida 1	President of the jury
REZOUG Tahar	Professor, USD Blida 1	Supervisor
DALA Laurent	Professor, Northumbria University Newcastle, UK	Co-Supervisor
MATAOUI Amina	Professor, USTHB	Examinator
BENKHEDDA Amina	Professor, USD Blida 1	Examinator
ZIDOUNI-KENDIL Faiza	MCA, USTHB	Examinator

ABSTRACT

Aircraft noise is dominant for residents near airports when planes fly at low altitudes such as during departure and landing. Flaps, wings, landing gear contribute significantly to the total sound emission. This paper aims to present a passive flow control (in the sense that there is no power input) to reduce the noise radiation induced by the flow over the cavity of the landing gear during take-off and landing. The understanding of the noise source mechanism, is normally caused by the unsteady interactions between the cavity surface and the turbulent flows as well as some studies have shown tonal noise due to cavity resonances, this tonal noise is dependent on cavity geometry and incoming flow, lead us to use of a sinusoidal surface modification application upstream of a cavity as a passive acoustics control device in approach conditions. It is demonstrated that the proposed surface waviness showed a potential reduction in cavity resonance and in the overall sound pressure level at the majority of the points investigated in the low Mach number. Furthermore, optimum sinusoidal amplitude and frequency were determined by the means of a two-dimensional Computational Fluid Dynamics analysis for a cavity with a length to depth ratio of 4. The noise control by surface waviness has not implemented in real flight test yet, as all the tests are conducted in the credible numerical simulation. The application of passive control method on the cavity requires a global aerodynamic study of the airframe, is a matter of ongoing debate between aerodynamicists and acousticians. The latter is aimed at the reduction of the noise whereas the former fears a corruption of flow conditions. In order to balance aerodynamic performance and acoustics, the use of the surface waviness in cavity leading edge is the most optimal solution. The proposed leading edge modification it has important theoretical basis and reference value for engineering application it can meet the demands of engineering practice. Particularly, to contribute to the reduce the aircraft noise adopted by the "European Visions 2020". The investigate cavity noise with and without surface waviness generation and propagation by employing a hybrid approach, the computation of flow is decoupled from the computation of sound, which can be performed during a post-processing based on Curle's acoustic analogy as implemented in OpenFOAM.

keywords— *Aeroacoutics, Landing Configurations, Cavity Noise, surface waviness, OpenFOAM, Triple Deck.*

RESUME

Pendant plus d'un si?cle de nombreuse recherches ont été effectuées sur l'aérodynamique et l'acoustique des écoulements affleurant une cavité, cependant apr?s la seconde guerre mondiale ces études ont trouvé une large application dans les avions, les soutes à bombes induisent des fluctuations qui peuvent exciter les modes vibratoires de la structure de l'avion. L'oscillation à travers et ou tours des cavités devient une question majeur pour les trappe d'un traine d'atterrissage. Avec une réduction des performances des avions par l'augmentation des trainées, la présence d'une cavité provoque de larges fluctuations de pression, de masse volumique ou de vitesse dans son voisinage ainsi que d'intenses ondes acoustiques. Plusieurs solutions pour contrôler le flux ont été élaborées au fil des ans, des solutions simples passives généralement basées sur des modifications de la géométrie ainsi que des méthodes de contrôle actives qui coutent tr?s ch?re. Les nuisances sonores et les vibrations engendrées par les instabilités rencontrées en écoulement de cavité ont également été le sujet d'un grand nombre d'études visant à leur suppression. Cependant, le besoin de l'industrie aéronautique moderne est de réduire l'acoustique de leurs conceptions pour réduire les nuisances sonores dans l'environnement des aéroports. Notre travail de recherche basée sur le contrôle acoustique de cavité par l'utilisation d'une surface ondulée dans les configurations des trains d'atterrissage. L'acoustique dans la cavité sera atténuée en contrôlons la couche de cisaillement développée en amont du bord d'attaque de la cavité.

Mots clés— *Aéroacoustique, Bruit de Cavité, Couche Limite, Surface Ondulée.*

Conference Articles

1. Mr. BELKALLOUCHE, Prof. REZOUG Tahar and Prof. DALA Laurent
   "Passive control of cavity acoustics via the use of surface waviness at subsonic flow"
   Congres Algerien de Mecanique
   Constantine- Algeria, 26-30 November 2017.

2. Mr. BELKALLOUCHE, Prof. REZOUG Tahar and Prof. DALA Laurent
   "Effets des surfaces ondulees sur le rayonnement sonore des cavites"
   4eme Edition du Congres des Doctorants-FSTGAT.
   USTHB- Alger, 24-25 Avril 2017
   .

3. ISBN 978-973-0-25597-3
   Mr. BELKALLOUCHE, Prof. REZOUG Tahar and Prof. DALA Laurent
   "Control of cavity acoustics by surface waviness in landing configurations"
   Proceedings of the conference, 6th CEAS Air and Space Conference
   Bucharest, ROMANIA 16-20 October 2017.

Journal Articles

https://doi.org/10.1108/AEAT-01-2018-0061
Mr. BELKALLOUCHE, Prof. REZOUG Tahar and Prof. DALA Laurent
"Passive control of cavity acoustics via the use of surface waviness at subsonic flow"
Aircraft Engineering and Aerospace Technology.

.	First Derivation of Time	
∞	Far-Field Values	
0	At initial condition	
t	Time	
x	Projection on X-axis	
y	Projection on Y-axis	
z	Projection on Z-axis	
u	Velocity in X-direction	[m/s]
v	Velocity in Y-direction	[m/s]
w	Velocity in Z-direction	[m/s]
λ	Wave Length	
μ	Dynamic Viscosity	[kg/ms]
ν	Kinematic Viscosity	[m^2/s]
ρ	Density	[kg/m^3]
ε	Perturbation Parameter	[non-dimensional]
D	Cavity Depth	[m]
L	Cavity Length	[m]
W	Cavity Width	[m]
δ	Boundary layer thickness	
f	Acoustic frequency of disturbance	
fm	Frequency of the mth mode	
$p^{'}$	Pressure perturbations	
p_{rms}	Root mean square pressure	
Re	Reynolds number	
St	Strouhal number	
G	Green function	
M_∞	Freestream Mach number	
P_{ref}	$Pref = 2 \times 10^{-5} Pa$, The value adopted as the minimum audible sound pressure variation	

ACRONYMS AND ABBREVIATIONS

CAA	Computaional Aero Acoustics
CFD	Computational Fluid Dynamics
LES	Large Eddy Simulation
RANS	Raynols Averaged Navier-Stokes
N-S	Navier-Stokes
PBiCG	Preconditioned Bi-Conjugate gradient solver for asymmetric matrices
GAMG	Generalized Geometric Algebraic Multi Grid
CN	Crank Nicolson
CFL	Courant Friedrichs Lewy
SIMPLE	Semi-Implicit Method for Pressure-Linked Equations
PISO	Pressure-Implicit Split Operator
SPL	Sound Pressure Level
PSD	Power Spectral Density
OASPL	Overall Sound Pressure Level
FFT	Fast Fourier Transform
OpenFOAM	Open Field Operation And Manipulation
CFD	Computational Fluid Dynamics
GCI	Grid Convergence Index
GIS	Grid-Induced separation
SGS	Sub-Grid Scale

TABLE OF CONTENTS

List of Tables

Table **Page**

List of Figures

Figure **Page**

CHAPTER 1

INTRODUCTION

Airframe noise refers to the noise generated by all components of the aircraft except the propulsion system (Noise in the context of this studied is undesired sound particularly that generated by a fluid flow). With the implementation of quieter jet propulsion systems, airframe noise becomes especially significant for larger, modern commercial aircraft.

Thus, the radiation of airframe noise will be a necessary component of the development of future commercial aircraft, particularly in the subsonic fleet. Earlier investigations indicated that there are many sources that contribute to airframe noise. One such component is cavity noise. Flow over cavities on solid surfaces became a topic of interest in the late 1950s and early 1960s with the introduction of high speed combat aircraft. The primary concerns at that time were the buffeting of the cockpits and the drag induced by flow over bomb bays and landing gear compartments, Figure 1.1. Effective noise control focuses on reducing the noise from these sources as near of the source as possible.

Noise suppression involves the reduction of noise sources efficiency and ability to convert kinetic energy to sound power, the interruption of sound transmission, the accelerated dissipation of acoustic energy into heat, or the active cancellation of sound waves using out-of-phase waves. These strategies can be implemented by a variety of passive, active, and reactive devices ranging in complexity from simple ear plugs to sophisticated anti-sound systems.

Cavity flows contains a wide range of physical phenomenon like unsteady shear

Figure 1.1: Bomb bays and landing gear.

layer, vortex shedding, recirculation eddies, instabilities and three dimensional effects. In many experimental studies, it has been observed, the interactions between the cavity surface and the turbulent flows produces intense acoustic tones, this tonal noise is dependent on cavity geometry and incoming flow. for that wide control techniques have been tested in order to reduce the cavity acoustic tones with variable results. Both active and passive control systems have been used. Passive control devices are the easiest to implement and a wide variety of systems were tested, in particular: spoilers, mass injection and modification of the cavity leading and/or trailing edge. These concepts sometimes proved to be very effective in reducing energetic tones but, in general, they did not succeed in suppressing multiple acoustic modes simultaneously.

The main objective of this work is to reduce the cavity flow noise using sinusoidal surface modification application upstream of a cavity. In these conditions the growth of some oscillation modes can be suppressed. The effect of a surface waviness in incompressible cross flow parallel to the leading edge of the cavity is a passive device that proved to be very efficient, as shown first by (Garry, Dala, 2009) [29].

Noise Generation Sound ordinarily refers to audible pressure fluctuations in the ambient air. However, sound can propagate as well in liquids and solids, and its frequencies can be lower (infrasonic waves below 20 Hz) or higher (ultrasonic waves above 20 kHz) than those that can stimulate the human ear and brain to the sensation

of hearing.

Sound can be generated by the vibrations of solid surfaces such as the strings of violins and similar musical instruments or the diaphragms of loudspeakers. It can also be generated by flow oscillations either directly or, more effectively, as a result of interactions with solid surfaces.

In 1952, Lighthill focused on the sources of sound in the absence of vibrating surfaces and termed the genre "sound generated aerodynamically". The field is now known as aeroacoustics or, in water applications, hydroacoustics.

Audible sound levels vary over an enormous range, and therefore a relative logarithmic scale is typically used to express the sound's power, level of pressure fluctuations or intensity (energy flux or product of pressure and velocity perturbations). Sound measured in decibels (dB) is computed from the relation: 10 log (X/Y), where X is either the sound power, the mean-square pressure fluctuations, or the mean sound intensity, and Y is a corresponding reference value typically related to the threshold of hearing. More subjectively, sound can also be measured in phons, where a loudness level of N phons is judged by the average ear to be as loud as a pure tone of frequency 1 kHz at a sound-pressure level of NdB. There is also the sone scale, which is a linear measure of loudness that is normalized so that 1 sone is a sound whose loudness level is 40 phons. A sound of 10 sones is 10 times as loud as a sound of 1 sone, and the audible sounds lie in a range of$\approx 0-100$ sones. Finally, there is the perceived noise decibel (PNdB), the A-weighted sound level (dBA), B-weighted, C-weighted,

Noise Effect The noise, defined as unwanted, excessive, uncomfortable sound, is a major problem in day to day life. Researchers have known for years that exposure to excessively loud noise can cause changes in blood pressure as well as changes in sleep and digestive patterns all signs of stress on the human body. The very word "noise" itself derives from the Latin word noxia, which means injury or hurt. For humans, unprotected exposure to sound levels above 100 dB for more than 15 minutes can cause hearing damage, and permanent hearing loss results when exposed to sound levels above 110 dB. The threshold of pain is between 130 and 140 dB.

ICAO Noise Certification Requirements The environmental regulations are concerned with the noise levels at and around airports during the take-off and landing situations. The international civil aviation organization (ICAO) annex 16 is the one involved with setting the standards of noise levels for aircraft and engine manufacturers.

Figure 1.2 shows the measurement points that the ICAO are concerned with. They are the approach point (area before the landing), sideline (on the runway), and take-off point (area surrounding the take-off of the plane). At these locations, the aircraft should meet its specific noise limit which depends on the aircraft's maximum takeoff weight and the number of engines.

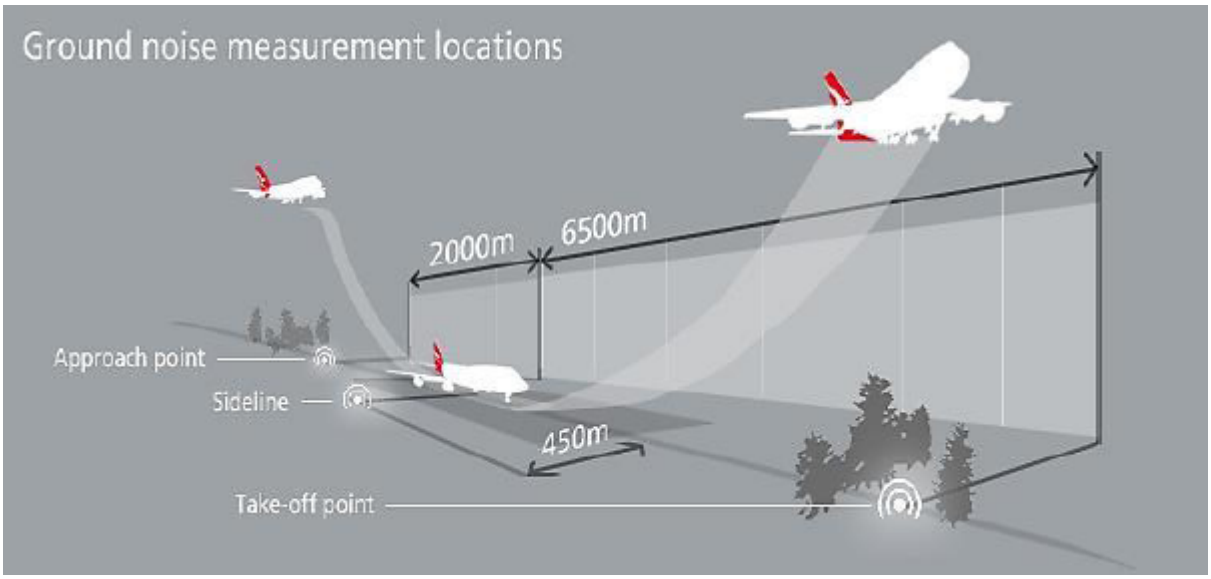

Figure 1.2: ICAO Noise Measurement Points.

Before a newly designed aircraft can be certified for commercial use, it must complete a standard set of procedures to allow for the evaluation of its acoustic signature. The certification process is divided into three procedures: lateral full power (takeoff), flyover, and approach. During takeoff, the engines are running at full power and therefore constitute the primary noise source. Alternately, during approach, the engines are running at relatively low power, resulting in airframe noise levels being comparable to engine noise levels

Outline The contents of this thesis are organised as follows:
Chapter 2 : This chapter is devoted to discuss about the literature related to cavity flows and the description about the inflow condition.

Chapter 3 : This chapter starts with the description about Aeroacoustics which includes acoustic analogy and the procedures that are followed to determine the sound pressure level of the noise generated by the cavity flow.

Chapter 4 : provides a general overview of main features of the OpenFOAM solver. The chapter description of the governing equations of Large Eddy Simulation.

Description of boundary conditions is also included. The test cases, geometries, meshing, challenges while performing simulations are also discussed in this chapter for both cases two and three dimensional cavity.

Chapter 5 : The chapter show the use of the Triple Deck theory to solve the equations of boundary layer. many test cases, geometries, meshing, numerical solution of the non-linear Triple-deck equations, which serve to identify the effects of frequency and the height (Amplitude) of the wave in the distribution of the displacement and pressure are discussed..

Chapter 6 : Results are summarised and analysis of both the baseline and the modified configuration were carried out. At the end of this chapter results obtained from acoustic analogy are presented and analysed

Chapter 7 : In this final chapter of the thesis, observations and conclusions are laid.

CHAPTER 2

INVESTIGATION OF FLOW PHENOMENA FOR CAVITY FLOW

There are several types of researchers who study flows past cavities. Aerodynamicists are concerned with the drag due to a cavity, which may serve as a bay for weapons or special cameras, or a landing gear well on an aircraft. Aeroacousticians study the sound waves generated by the self-induced oscillations of the flow inside a cavity, which can affect the avionics and the people on board. Fluid dynamicists are interested in the complex structure of the flow in a cavity. There exist both experimental and computational investigations on the flow fields of two and three dimensional rectangular cavities. Although work has been conducted from the subsonic to hypersonic regimes, most of the effort has been concentrated on the supersonic speed regime. In the subsonic and transonic regime, static pressure data have been sparse.

2.1 Leading parameters

Karamcheti [33] reported that there is a minimum cavity length needed for generation of cavity noise, depending on the Mach number of the flow and whether the approaching boundary layer is turbulent. If the cavity length is less than the minimum length, the flows will not oscillate. The dependence of cavity noise amplitude on various cavity geometric and flow parameters is seriously lacking.

In view of the wide variety of configurations, and the numerous primary or secondary parameters which drive cavity oscillations, it seems neccessary to draw some classifications.

2.1.1 Cavity geometry

Figure 2.1-(a) illustrates the length L, depth D and width W in an experimental setup with respect to the stream wise flow direction and the Figure 2.1-(b) carries details showing the incoming boundary layer at the leading edge of the cavity, shear layer over the cavity and the pressure perturbation from the trailing edge of the cavity due to the impingement of the shear layer on the corner of the downstream of the cavity. Eddy or eddies are created inside the cavity depending on various parameters which will be dicussed inside the chapter.

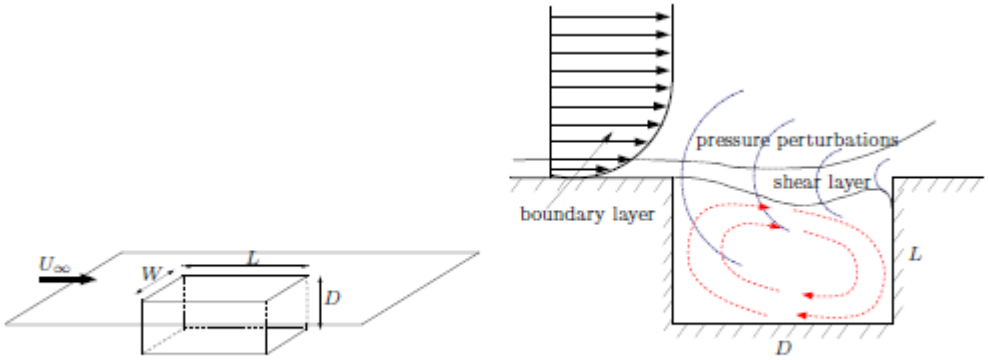

(a) Cavity geometry and parameters (b) Schematic diagram of cavity flow

Figure 2.1: Cavity flow [22]

2.1.1.1 Ratio of length over depth L/D

In the literature, vastly different values of length-to-depth ratio (L/D) have been quoted to define the cavity flow types. For instance: L/D < 7 for open and L/D > 13 for closed cavity flow is reported by Stallings and Wilcox [63] whereas L/D < 10 for open and L/D > 13 for closed cavity flow is reported in the work of Plentovich [47]. Similarly, Dix and Bauer [14] quote L/D < 9 for open and L/D > 13 for closed cavity flow whereas Srinivisan and Baysal [61] quote L/D < 3 for open and L/D > 10 for closed cavity flowfields. Tracy and Plentovich [69] investigated the variations in the values of L/D and concluded that the vast disagreements in the literature were due to the dependence of

the cavity flow type on Mach number as well as L/D. Four different types of cavity flows at subsonic speed have been identified depending on the value of this ratio are shown in Figure 2.2, separation point at the upstream of the cavity and stagnation point at the downstream of the cavity with dividing streamline for the open cavity at subsonic velocity. For the closed cavity at the subsonic speed, a separation point occurs at the leading edge of the cavity, impingement point and second separation point are at the bottom of the cavity with a stagnation point at the trailing edge of the cavity. In the this closed cavity configuration, the profile of the dividing stream line starts from the bottom of the cavity. Open cavities refer to flow over cavities where the boundary layer separates at the upstream corner and reattaches near the downstream corner. Open cavities may further be divided into shallow and deep cavities. The cavities with aspect ratio L/D > 1 may considered as shallow and for L/D < 1 the cavities may be considered deep. Cavities are closed when the separated layer reattaches at the bottom of the cavity and again separates ahead of the downstream wall of the cavity. The other important parameters that affect cavity flow types are incoming boundary layer thickness (δ), ambient density (ρ), viscosity (μ), and speed of sound (a_0). When the cavity is very elongated, it can be modeled in a first approximation by

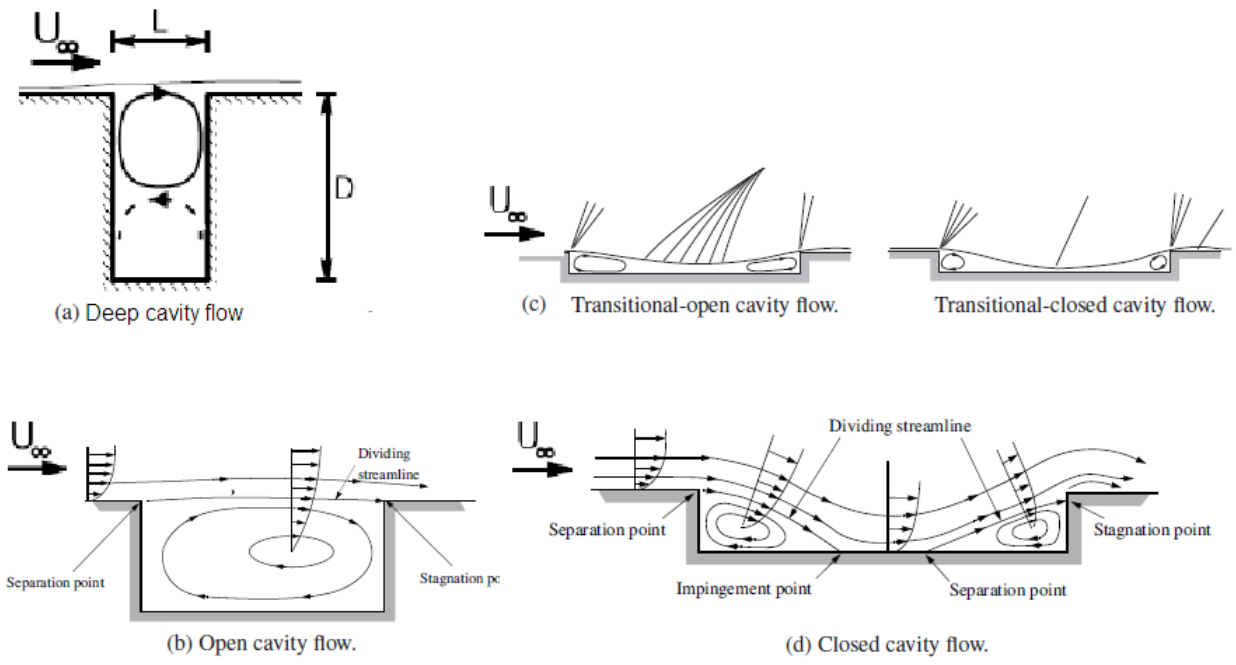

Figure 2.2: Schematic of deep (a), and shallow cavities: open (b), transitional (c), and closed (d) [17]

a backward-facing step followed by a decoupled forward-facing step. Thus, when the mean flow reattaches the floor of the cavity, the cavity is qualified to be closed. The flow then separates again as it approaches the rear-wall of the cavity. The cavity is termed open in the other limit. In this flow regime, the oncoming boundary layer separates from the leading edge and forms a free shear layer which spans the mouth of the cavity and impinges at the trailing edge of the cavity. Between these two states, a transitional flow regime can occur, which exhibits characteristics that are indicative of both the open and closed flow regimes. The extensive measurements show that open-cavity flow are observable in cavities with L/D ratios on the order of 6 to 8. The pressure distributions on the cavity walls are used to discriminate between different flow regimes. Schematics representing of Cavity flow types and corresponding pressure distributions are shown in Figure 2.3.

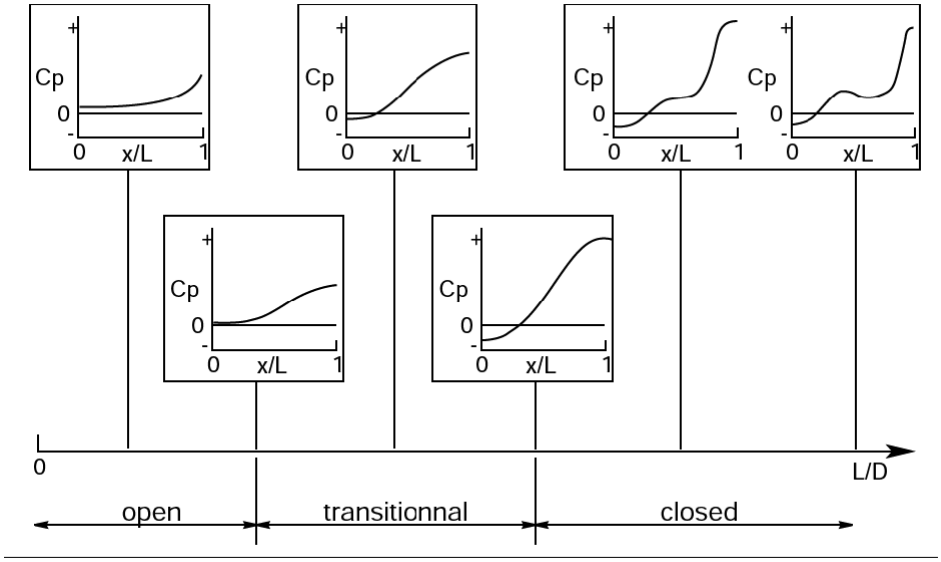

Figure 2.3: Classification of cavities as a function of the evolution of pressure coefficient at the cavity floor. From Tracy et al. [48]

2.1.1.2 Ratio of length over width L/W

Another important geometrical parameter is the length-to-width L/W ratio. Ahuja and Mendoza [5] conducted experiments on the effect of cavity dimensions, boundary layer, and temperature on cavity noise for subsonic flows with turbulent boundary layer upstream of the cavity. They determined that the ratio L/W, provided a transition

between two-dimensional (L/W < 1) and three-dimensional flow (L/W > 1) and observed that the intensity of the oscillations are reduced by changing from a two dimensional to a three-dimensional cavity and the three-dimensional cavity flow produce lower levels of cavity feedback tones (as much as 15 dB) compared to two-dimensional cavity flow, with no change in tonal frequency.

At each of the four tested velocities, and for two length-to-depth ratios (namely 1.08 and 2), Block [7] noticed that the narrower cavities (higher L/W) generate the more sharply defined tonal spectra. In some situations, the self-sustained oscillations are not present for the wider cavity, whereas intense tones are induced when the width is decreased. The wide and narrow cavities peak at the same frequency, so that the resonance frequency is not related to the width. This last point is also checked in the measurements of Ahuja and Mendoza [5].

Figure 2.4 [57] shows the effect of width on cavity oscillations at Reynolds number $R_{e_{\delta_0}} = 2.86 \times 10^3$ and $\frac{d}{\delta_0} = 10$ where Non-dimensional Frequency $\frac{fb}{U_e}$ is plotted against non-dimensional width $\frac{b}{\delta_0}$. There was a slow increase in non-dimensional frequency as $\frac{b}{\delta_0}$ increased. as the critical value of $\frac{b}{\delta_0} = 8.15$ was reached, oscillations jumped to a higher mode.

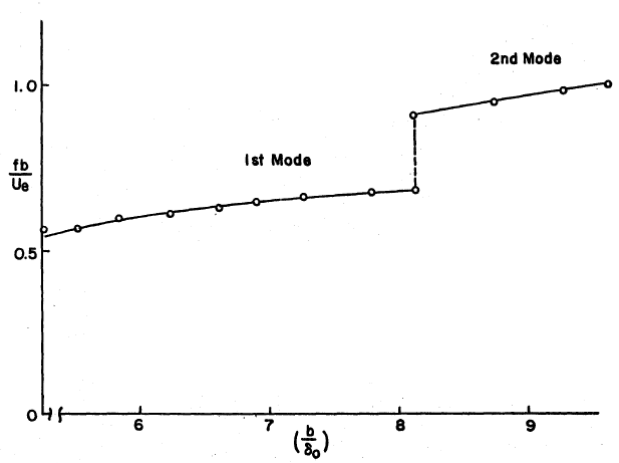

Figure 2.4: Effet of Width on Non-dimensional Frequency at $R_{e_{\delta_0}} = 2.86 \times 10^3$ and $\frac{d}{\delta_0} = 10$ [57]

2.1.2 Incoming flow

The influence of the freestream flow velocity has been investigated in the majority of the experimental studies. The cavity flow physics and its resonance depend on several

flow parameters.

2.1.2.1 Mach number

The effects of Mach number on non-dimensional frequency $\frac{fb}{U_e}$ have been studied by many investigations for both laminar and turbulent boundary layers. On the basis of high speed shadow-graphs of cavity oscillation, Rossiter [54] speculated that periodic vortices are shed at the upstream corner in sympathy with the pressure oscillation produced by interaction of the vortices with the downstream corner. Based on this idea Rossiter derived a formula for the oscillation frequency.

Heller [**?**] and Covert studied shallow cavities over a wide range of Mach numbers and correlated a great many experimental results with Rossiter's formulation of cavity oscillation frequency, the vortices shed from the upstream cavity corner are assumed to convect at a constant phase velocity through the shear layer, resulting in a linear phase distribution.

The increase in Mach number affects the critical L/D ratio. Critical L/D refers to a particular ratio beyond which the flow behaves completely as a closed cavity flow, and below which it behaves as an open cavity flow [62].

2.1.2.2 Boundary layer thickness

Colonius [10] states that the momentum thickness θ_0 at the leading edge of the cavity plays a vital role in the selection of the modes and in governing the growth of the shear layer. They also found $\frac{L}{\theta}$ for lower limit for the cavity resonance to be approximately $\frac{L}{\theta} \approx 80$. When the ratio of the cavity length to the momentum thickness of the incoming boundary layer ($\frac{L}{\theta}$) is in the range $80 < \frac{L}{\theta} < 120$, the self-sustained oscillations take place in the shear layer mode. When $\frac{L}{\theta}$ exceeds 120, another mode of cavity oscillation has been observed, but has received much less attention, and is relatively poorly understood. In incompressible experiments for an axi-symmetric cavity, Gharib and Roshko [23] observed a wake mode, where the oscillating flow over the cavity resembles the wake behind a bluff body, rather than a free shear layer. Flow features in this wake mode were qualitatively very different from those in the shear-layer mode described by Rossiter, and wake mode was accompanied by a large increase in drag. Similar dramatic increases in drag had been previously observed by Fox [21] as the cavity length was increased, in flows with thin laminar upstream boundary layers, and Roshko [53] observed an intermittency analogous to the large fluctuations of drag which occur on a bluff cylinder in the critical range of Reynolds

number, where the flow may be switching between shear-layer mode and a type of wake mode.

Grace et al [25] performed measurements of both laminar and turbulent upstream boundary layers cases with low Mach number. They found no evidence of self-sustained oscillations in streamwise velocity data obtained using a hotwire or in wall pressure fluctuation data obtained using a microphone when an incoming boundary layer is turbulent. They examined mean and turbulent flow fields in a shallow cavity with aspect ratio $\frac{L}{D} = 4$. The laminar cases with $\frac{L}{\theta} = 130$ and 190 and the turbulent cases with $\frac{L}{\theta} = 78$ and 86 were performed with corresponding Reynolds number, $R_{e_\theta} = \frac{\rho_\infty U \theta_0}{\mu}$ were 2892, 3949 for laminar cases and 6318, 12627 for turbulent cases respectively.

Sarohia [57] stated that the parameters cavity depth D and initial momentum thickness θ_0 at the leading edge also are as important as the cavity length L, for a fixed value of the edge velocity U_e, depth D and Width W, there exists a maximum value of shear thickness $\delta_{0_{max}}$ above which the cavity does not oscillate. As the shear layer thickness δ_0 is decreased ($\delta_0 < \delta_{0_{max}}$), the frequency of cavity oscillations increases.

2.1.2.3 Reynolds number

For fixed upstream geometry, a change in the Reynolds number will cause an associated change in the boundary layer at the leading edge of the cavity. So it is possible that sufficiently large changes in Reynolds number may still indirectly effect the nature of the resonance through a change in the upstream boundary layer. Certainly a change from a laminar to turbulent boundary layer is known to effect the resonance (Karamcheti) [32]. Figure 2.5 shows the results of the effect of Reynolds number $R_{e_{\delta_0}}$ on non-dimensional frequency $\frac{fb}{U_e}$.

2.2 Theories from experiments

Earlier experimental investigations and theoretical studies have laid out the fundamentals of cavity noise generation mechanisms. Many studies have identified that for intense tonal noise generation arise from discrete frequency oscillations, the mechanism can be either:

1. a feedback mechanism in which the shear layer generated at the upstream edge of the cavity impinges on the downstream cavity edge, generating acoustic waves

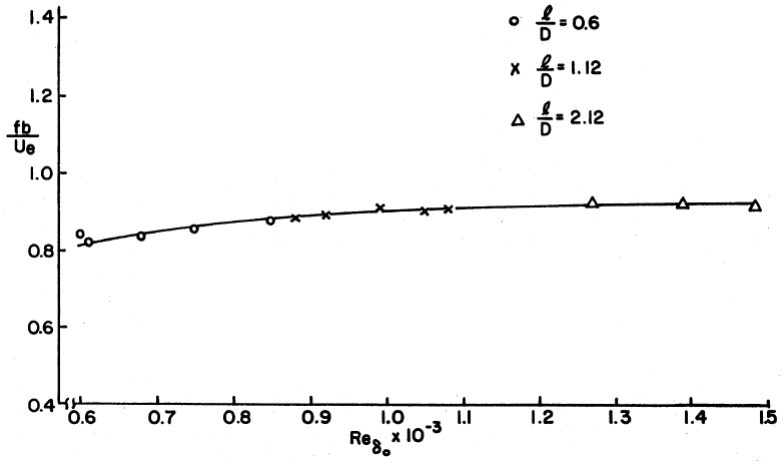

Figure 2.5: Effet of Reynolds Number on Non-dimensional Frequency at $\frac{b}{\delta_0} = 12.76$, (Sarohia) [57]

that propagate upstream and further excite the shear layer growth, as shown schematically in Figure 2.6; Or

2. an acoustic resonance in which the cavity is driven by the unsteady pressure across its mouth in normal modes for deep cavities.

Flow-induced cavity noise is a very complex phenomenon. The flow is unsteady and highly three-dimensional, even for a cavity of low length to width ratio. Krishnamurty published his work on the acoustic radiation from two-dimensional rectangular cutouts in aerodynamic surfaces [39]. This work was motivated by the need to understand the flow field in bomb bays used for the internal carriege of weapons and the open cockpits.

It was observed in experiments. the acoustic field influenced by five main parameters :

- Mach number. The radiation become more intense as the Mach number is increased.
- a minimum length was required for an acoustic field to occur.
- as the L/D ratio of the cavity was increased (from L/D=1), the intensity of the acoustic radiation was observed to increase at first before it gradually diminished.

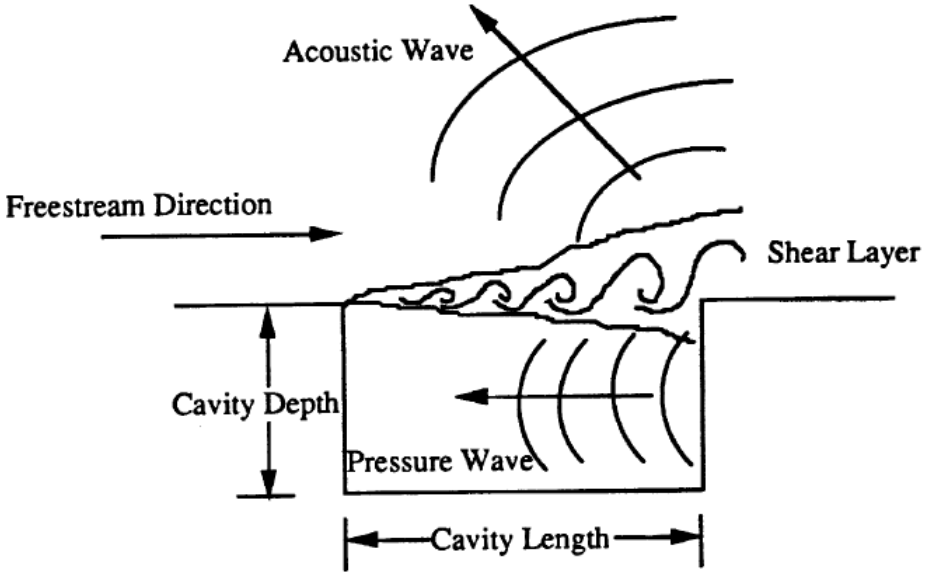

Figure 2.6: A schematic representation of the feedback mechanism for noise generation in a shallow cavity [5]

- a laminar boundary layer upstream provided a clear and well-defined acoustic field, while the field obtained from a turbulent boundary layer was weak and diffused.
- the wavelength of the acoustic radiation increased with the cavity length.

Krishnamurty recognised that the oscillating shear layer impinging on the aft wall of the cavity was a key element in the production of the acoustic radiation.

2.2.1 Frequency measures

Since the early investigations on feedback loop phenomena for cavities, or other impinging shear layers, numerous semi-empirical relationships have been proposed to adapt the typical phase relationship to experimental observations. The frequency f at a given value of M_∞ and T_0 was found to be inversely proportional to the gap breadth b Eq. (2.1):

$$f = \alpha \frac{1}{b} \tag{2.1}$$

The constant of proportionality α was different for laminar and turbulent layers and was usually lower for turbulent layers. In the laminar case Krishnamurty measured the

frequencies at a Mach number of 0.815 and a stagnation temperature of 116.8^0F is presented in Figure 2.7. The dominant frequency and the first harmonic are shown. The harmonic frequency is twice the corresponding dominant frequency. The range of gap breadths covered for the measurementswas from 0.1 inch to 0.5 inch. It may be noted that most of the frequencies measured for this case were in the ultrasonic range. In the turbulent case the measurements of frequency with turbulent boundary layer are differed from those of the laminar case. while in the laminar case only a single domain frequency was observed at a given gap width an Mach number, in the turbulent case two frequencies of nearly equal strength were recorded [39].

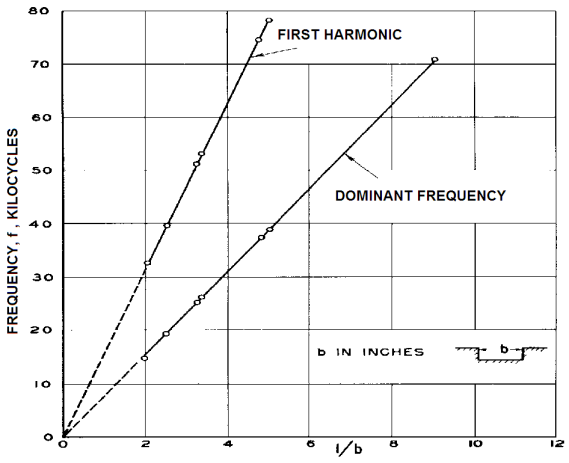

Figure 2.7: Results of frequency measurments for laminair case forrang of gap breadths from 0.1 to 0.5 inch. $M_\infty = 0.815$; $T_0 = 116.8^0F$. [39]

2.2.2 Nondimensional frequency

Obviously one would like to from a dimensionless frequency or Strouhal number. The measurements have shown that the frequency f is related to b, the breadth of the cavity. To form a Strouhal number a characteristic velocity has to be chosen.If one uses U_∞, the free-stream velocity, one has

$$S = f\frac{b}{U_\infty} \tag{2.2}$$

It has been seen that, for a given free-stream velocity Mach number M_∞ and stagnation temperature T_0.

$$fb = Constant = \alpha \tag{2.3}$$

The constant α is then a function of M_∞ and possibly T_0.

$$S = \alpha \frac{1}{U_\infty} = \alpha \frac{1}{a_0} \frac{1}{\frac{U_\infty}{a_0}} \tag{2.4}$$

The variation of S with Mach number for a turbulent boundary layer is shown in Figure 2.8. Krishnamurty recorded two frequencies of equal magnitude with the *high* frequency almost double the *low* frequency.

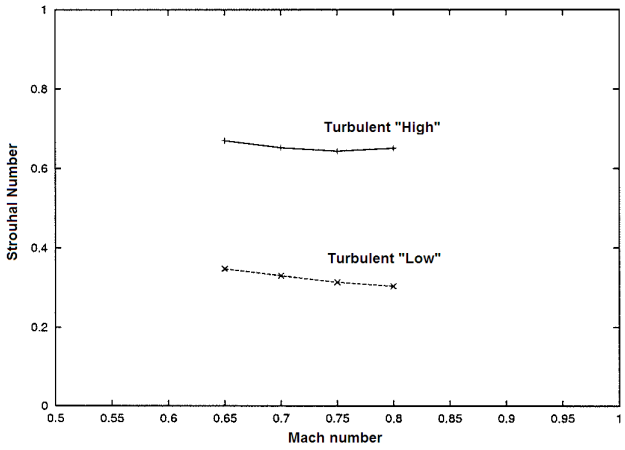

Figure 2.8: Variation of Strouhal Number with Mach Number (Krishnamurty)[39]

2.2.2.1 Rossiter modes

In 1964, Rossiter [54] advanced on the findings of krishnamurty [39]. more then two frequencies were observed and he suggested that these frequencies indicated a feedback mechanism.

A sound pulse is generated when these vortical structures reaches the downstream edge, then propagates upstream and excites the shear layer formation. A vortex travels across the cavity in time $\frac{L}{U_c}$, where U_c is the convection velocity of the vortical structures, whereas the sound radiates back to the upstream edge in time $\frac{L}{c_0}$, c_0 denoting the speed of sound. The feedback pressure wave must attain the upstream edge just at the right instant to reinforce the periodic shedding, so that the frequency f satisfies the feedback equation Eq. (2.5):

$$\frac{L}{U_c} + \frac{L}{c_0} = \frac{n}{f} \tag{2.5}$$

where n is an integer representing the number of vortices in the shear layer.

A semi-empirical formula was proposed for predicting the discrete tones detected in the experiments. Rossiter proposed that vortices which are shed from the cavity leading edge are convected downstream until they interact with the aft cavity wall, generating acoustic pulses. These acoustic pulses propagate upstream in the cavity eventually reaching the front cavity wall. At this time they induce separation of the shear layer which results in the shedding of another vortex, completing the feedback loop. Based on this description a formula was proposed to predict the frequencies, given by Eq. (2.6):

$$f_m = \frac{U_\infty}{L} \frac{m - \gamma}{M_\infty + \frac{1}{\kappa}} \tag{2.6}$$

The Figure 2.9 illustrate typical spectra for cavity with open flow as well as a section of the resonant range classification presented in corresponding to the cavity dimensions of interest for this study.

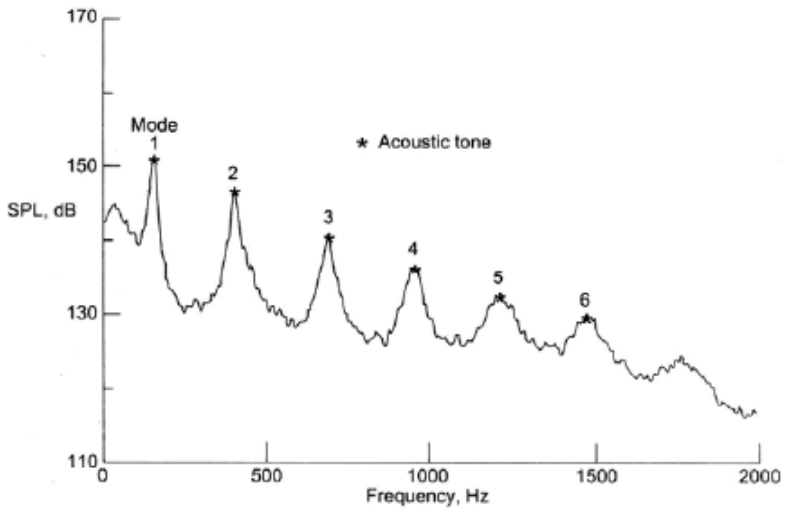

Figure 2.9: Typical Spectral View of Rossitor Modes [48].

where m is an integer index for the frequency of interest (m=1,2,3...), γ is constant for a fixed L/D and κ represents the ratio of the speed of the vortices to the free-stream speed. where κ is empirical constant, $\kappa = 0.57$ yields a fairly good collapse with the experimental data. For shallower cavities (L/D from 4 to 10), Rossiter adjusted the constant γ, by using the values of Table 2.1.

The sequence of frequencies is the same as that found by Brown [9] in his classic experiments on the 'edge-tone' which occurs when a wedge is placed in a laminar

L/D	γ
4	0.25
6	0.38
8	0.54
10	0.58

Table 2.1: Values of γ as a function of the length-to-depth ratio L/D, from Rossiter [54]

jet issuing from a narrow slit. The parameter γ accounts for the time lag that occurs between a vortex being shed from the front of the cavity and an acoustic disturbance being generated at the aft wall. It is assumed that the acoustic radiation initiates vortex shedding at the leading edge, whilst the impact of the vortices on the aft cavity wall is the generating mechanism for new acoustic waves. In the shallower cavities (length/depth ratios from 4 to 10) there are generally two or more peaks of similar magnitude in the amplitude spectra. The agreement for a range of Mach numbers between the frequencies predicted and measured by Rossiter is shown to be close in Figure 2.10.

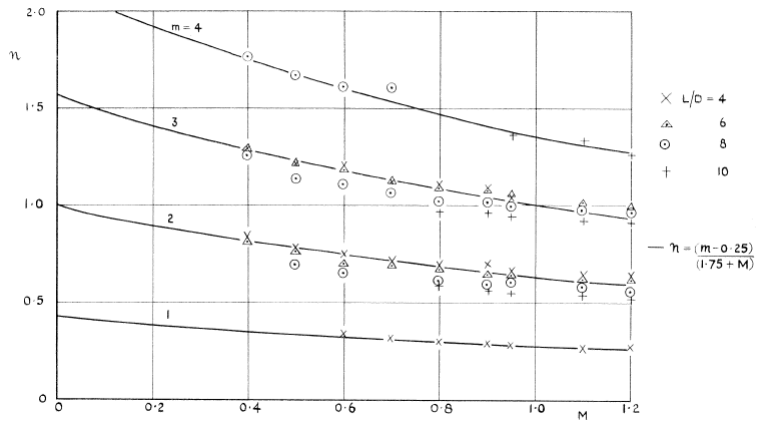

Figure 2.10: Frequency of periodic pressure fluctuations in shallower cavities [54].

Rossiter suggested a physical interpretation for his formula by analogy with the edge-tone phenomenon. The acoustic waves generated at the downstream corner will induce the shedding of vortices at the upstream corner. This vorticity is in turn responsible for the acoustic emission as it interacts with the downstream corner. λ_a denotes the acoustic wavelength and λ_v the aerodynamic wavelength, that is the spacing between two vortices. At the initial time t = 0, the phase of the upstrem-propagating acoustic wave is supposed to be zero, and the cavity spans n_a complete

wavelengthes λ_a. At this time, there is a vortex located at a distance $\alpha_v \lambda_v$ downstream of the downstream corner, as depicted in Figure 2.11(a).

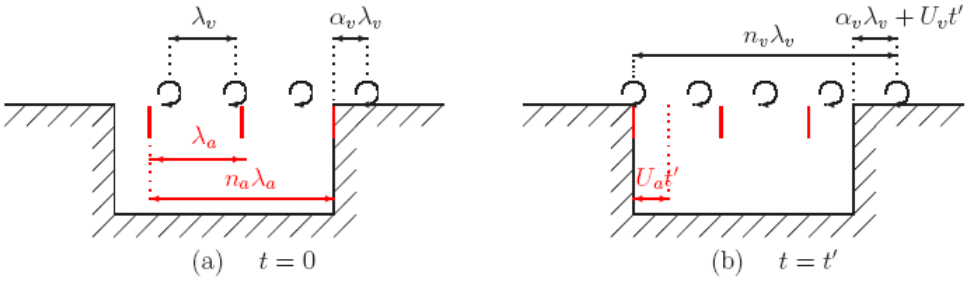

Figure 2.11: Simplified model of the flow over a cavity, [54][57]

At the time $t = t^{'}$, a wavefront reaches the upstream corner, synchronized with the shedding of a new vortex. The vortices have been convected over a distance $U_v t^{'}$, and the vortex downstream of the downstream corner is now located at $\alpha_v \lambda_v + U_v t^{'}$, as indicated in Figure 2.11(b). For the n_v vortices above the cavity opening, we can write Eq. (2.7):

$$n_v \lambda_v = L + \alpha_v \lambda_v + U_v t^{'} \tag{2.7}$$

In the same period of time, the acoustic wavefronts have propaged over $U_a t^{'}$ in the supstream direction, so that Eq. (2.8):

$$L = n_a \lambda_a + U_a t^{'} \tag{2.8}$$

Eliminating $t^{'}$, this yields:

$$\frac{U_v}{U_a} n_a \lambda_a + (n_v - \alpha_v)\lambda_v = L(1 + \frac{U_v}{U_a}) = kL(\frac{1}{k} + M\frac{c_\infty}{U_a}) \tag{2.9}$$

where c_∞ is the sound speed above the cavity, k is the ratio $\frac{U_v}{U_\infty}$, and M the Mach number $\frac{U_\infty}{c_\infty}$. The oscillation frequency $f = \frac{U_v}{\lambda_v} = \frac{U_a}{\lambda_a}$ is introduced to lead:

$$\frac{fL}{U_\infty} = \frac{(n_a + n_v - \alpha_v)}{(\frac{1}{k} + M\frac{c_\infty}{U_a})} \tag{2.10}$$

A comparison with the empirical formula Eq. (2.6) indicates that the physical model is compatible with the experimental data if we choose: $n_a + n_v = m$; $\alpha_v = \gamma$; $k = \kappa$; $c_\infty = U_a$;

2.2.2.2 Bilanin and Covert's model

In 1973, Bilanin and Covert [6], discuss their work in some detail. This analysis consists of three parts: the analysis of the shear layer stability: the calculation of the interior acoustics of a rectangular cavity; and the prediction of the cavity oscillation frequency. In the first part of the calculation, the shear layer is modeled as a vortex sheet that is only dependent upon the depth of the cavity. With this assumption, the effect of shear layer impingement at the downstream edge of the cavity is eliminated, and the separation of upstream and downstream edge effects and the pressure field from the upstream edge have little effect on the vortex sheet except near the upstream edge. Therefore, the only boundary conditions required in the stability analysis are the rigid wall boundary condition at the floor of the cavity, the kinematic and dynamic boundary conditions at the shear layer interface, and the outgoing radiation boundary condition above the shear layer. According to the photographs taken by Krishnamurty [39], the shear layer impingement generates an acoustic source at the downstream edge of the cavity. Hence, in the second part of the analysis, Bilanin and Covert [6] assumed a mass addition and removal at the downstream edge of the cavity as the cause of the acoustic source. The velocity potential for a two-dimensional acoustic monopole in a static medium is defined as

$$\Phi = Be^{-i\omega t} H_0^{(1)}[(\frac{\omega}{a_-})|r - r_0|] \tag{2.11}$$

where B represents the strength of the source, ω is the radian frequency of the source, a_- is the local speed of sound inside the cavity, $H_0^{(1)}$ is the zeroth order Hankel function of the first kind, and r_0 is the source position vector. To approximate the velocity potential inside the cavity without violating the boundary conditions on the solid walls, the velocity potentials for each acoustic source in the image system are summed together, given by

$$\Phi = Be^{-i\omega t} \sum_{m=0}^{1} \sum_{n=-\infty}^{\infty} H_0^{(1)} \frac{\omega}{a_-} \sqrt{[x - (2n+1)L]^2 + (y + 2mD)^2} \tag{2.12}$$

The summation over n is for the contribution from the sources located at $x = \pm L, \pm 3L, ...$, and the summation over m is for the sources located at y = 0 and y =-2D. The pressure field can be related to the velocity potential by

$$P = i\omega\rho_-\phi \tag{2.13}$$

where ρ_- is the density of the flow field inside the cavity. Since it is assumed that the acoustic pressure field forces the vortex sheet at the upstream edge of the cavity,

an expression for the pressure at the origin is required. By setting x = y = 0. assuming a symmetry condition along the y-axis, and using an approximation for Hankel functions of large argument, their asymptotic representation yields

$$P = 2i\omega\rho_{-}Be^{-i\omega t}(\sum_{m=0}^{1}\sum_{n=0}^{N-1}H_0^{(1)}S_2\sqrt{(2n+1)^2+(\frac{2m}{L/D})^2}+R) \tag{2.14}$$

where

$$R = 2e^{i\frac{\pi}{4}}\cos(S_2)\sum_{n=N}^{\infty}\frac{1}{\pi n S_2}e^{2iS_2 n} \tag{2.15}$$

N is the number of acoustic monopole sources used along each y = constant line, since it is not realistic to use an infinite number of sources, and S_2 is a Strouhal number defined by $S_2 = \frac{\omega L}{a_{-}}$. The phase of the pressure given by Equation 2.14 has been evaluated for N = 2, which corresponds to four image sources, and $\frac{L}{D}$ ratios of 4 and ∞. It was found that the error incurred for the phase of the pressure at the upstream edge of the cavity by neglecting R and all sources except the one located at the downstream edge is small for cavities with $\frac{L}{D}$ ratios greater than 4. Therefore, in Bilanin and Covert's study, calculations were made with only a single source at the downstream edge of the cavity, implying the assumption of a very shallow cavity. The derived frequency model is similar to the model given by Rossiter in Equation 2.6.

The shear layer is modeled as an infinitely thin vortex sheet, and an acoustic monopolar source is located at the downstream corner. To full fill the model, a pressure line source is imposed at the upstream corner in order to represent the excitation of the shear layer by the pressure disturbances. Fixing the phase relationship to 2π between the two corners, the following expression is derived

$$St = \frac{n-\frac{3}{8}-\frac{\phi}{2\pi}}{\frac{\alpha_r U_\infty}{\omega}+M\frac{c_+}{c_-}} \tag{2.16}$$

which is formally identical to formula (2.10), if we choose: $\alpha = \frac{3}{8}+\frac{\phi}{2\pi}$ and $\kappa = \frac{\omega}{\alpha_r U_\infty}$ where ϕ and $2\pi\times\frac{3}{8}$ correspond to the phase lags, respectively due to the upstream and downstream edges, ω and α_r are the radian frequency and the real part of the complex wavenumber of the unstable vortex sheet solution respectively and U_∞ is the velocity outside the cavity. This formula takes the compressibility factor into account through the ratio $\frac{c_+}{c_-}$ between the exterior and interior sound speeds. It is important to point out that the constant α is not restricted to a phase lag due to the complex impingement process on the downstream corner, but is also the expression of the

correction at the upstream edge during the initial phase of the vortex shedding. In the

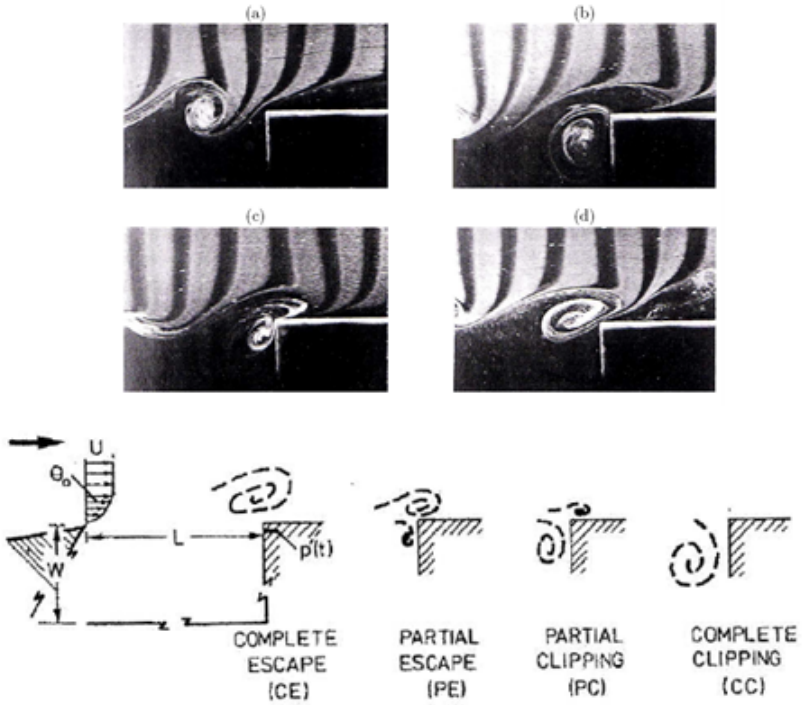

Figure 2.12: Classes of possible of vortex-corner interactions. From Rockwell and Knisely [50]

study by Bilanin and Covert [6], the internal cavity wave structure is uncoupled from the shear layer motion in order to simplify the analysis. It is assumed that the cavity internal pressure modes force the shear layer only at the upstream edge and, therefore, only the downstream wave motion of the shear layer is considered. To eliminate this assumption, Heller and Bliss [28] introduced the concept of the "pseudopiston" effect Figure 2.12 [50]. This is similar to the replacement of the downstream cavity wall with an oscillating piston. The mass addition and removal creates pressure fluctuations that travel upstream in the cavity, and further amplifies the vortices shed at the upstream edge. In this manner, the internal cavity acoustic wave is coupled with the shear layer motion, and the feedback loop is complete.

2.2.2.3 Heller and Bliss model

In 1971, Heller, Holmes and Covert [27] took into account the effect of variations of the sound speed for high Mach numbers M > 1.2. The modified formula for the sound

speed follows:

$$\frac{c_{[cavity]}}{c_\infty} = \sqrt{1 + r\frac{\gamma - 1}{2}M^2} \tag{2.17}$$

where γ is the ratio of specific heats, and r the thermal recovery coefficient, defined as:

$$r = \frac{T_c - T_\infty}{T_0 - T_\infty} \tag{2.18}$$

where T_∞, T_0 and T_c are the free-stream static temperature, the stagnation temperature, and the temperature inside the cavity, respectively. They found 0.8 < r < 1 with an increase of r with increasing Mach numbers.

A description of the events occurring in an open cavity which was based on wave propagation was put forward by Heller and Bliss in 1975 [**?**]. The experimental study recorded information about frequencies, mode shapes and acoustic levels for different $\frac{L}{D}$ ratios and Mach numbers. Palliative devices were also investigated. Despite basing the description on acoustic wave propagation, use was made of the equation developed by Rossiter. The tones detected in the experiments fell on the curves that are associated with the resonant modes, as defined by the Rossiter equation, modified to account for the higher sound speed in the cavity as

$$f_m = \frac{U_\infty}{L}\frac{m - \alpha}{\frac{M_\infty}{\sqrt{1+[(\gamma-1)/2]M_\infty^2}} + \frac{1}{\kappa}} \tag{2.19}$$

where γ is the ratio of specific heats and f_m is the modified resonant frequency corresponding to the mth mode. Heller and Bliss determined from their experiments that the constants α and κ are 0.25 and 0.57. respectively. It was previously estimated that for cavities with a $\frac{L}{D}$ ratio of 4 or greater, the difference between the unmodified Rossiter formula and experiments should be within 10% [27]. Although the derivation of the Rossiter equation was based on vortex shedding, Heller and Bliss did not consider this for their modified equation and instead focussed on wave propagation. Figure 2.13-1 indicates a pressure wave moving downstream and approaching the trailing wall. This wave produces an outward deflection of the shear layer that allows fluid to leave the cavity at the trailing edge. Upstream, a pressure wave, which previously had been travelling upstream, is reflected from the forward wall and now also moves downstream. In Figure 2.13-2, the upstream wave continues to travel downstream. The downstream wave, however, has reflected from the aft wall and propagates upstream through the relatively inactive fluid within the cavity. This wave moves supersonically with respect to the freestream and so a compression wave is generated in the external

flow. At the rear bulkhead, the shear layer lies below the cavity lip, resulting in mass addition to the cavity. The forward and rearward propagating waves intersect near the centre of the cavity and, after interacting, maintain their respective directions as shown in Figure 2.13-3. At the aft bulkhead, the shear layer continues to inject fluid into the cavity, thus creating a recirculating flow. In Figure 2.13-4, the aft wave is seen to lift the shear layer above the downstream lip, resulting in mass removal, while the forward wave is about to impact the front bulkhead and complete the oscillation cycle that began with the situation depicted in Figure 2.13-1.

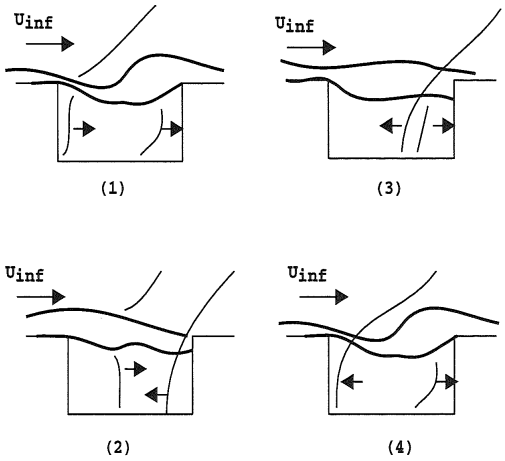

Figure 2.13: Schematic Representation of Cavity Oscillation Cycle [27]

2.2.2.4 Tam and Block's model

Block [7] wanted to generalize the work of Bilanin and Covert by taking into account the effect of the finite depth D of the cavity. To this end, she used image sources to represent the reflexions by the cavity walls. The new formula still bears some similarities with Rossiter's formula, but the ratio $\frac{L}{D}$ appears now explicitly:

$$St = \frac{n - \frac{1}{4} - \frac{\beta}{2\pi} - \frac{\phi}{2\pi}}{\frac{1}{\kappa} + M(1 + \frac{0.514}{\frac{L}{D}})} \tag{2.20}$$

where β represents the phase lag between the acoustic source and positive motions of the shear layer at the downstream edge, and ϕ is the phase lag between the arrival of the wavefront on the upstream edge and the shedding of new instabilities. This phase lag ϕ is identical to ϕ in the Bilanin and Covert formula (2.16), but whose value is not explicitely given. That is why Block suggested that it is negligible, as in the Rossiter

model. The phase lag at the downstream edge is fixed at $\beta = -\frac{\pi}{2}$, yielding $\frac{\beta}{2\pi} = \frac{1}{4}$, as in the Rossiter formula. The compressibility factor is taken at 1 since subsonic velocities are of interest. The term $(1 + \frac{0.514}{\frac{L}{D}})$ estimates the variation of the slope of the phase as a function of $\omega\frac{L}{c}$. This dependence is a straight line for $\frac{L}{D}\,\mathrm{sup}\,1$, whose slope is related to $\frac{L}{D}$. The final formula of Block is:

$$St = \frac{n}{\frac{1}{\kappa} + M(1 + \frac{0.514}{\frac{L}{D}})} \tag{2.21}$$

2.3 Shear and wake mode

For the low Mach number flows, the cavity has been classified as shear mode or wake mode according to the shear-layer on the cavity. In a shear layer mode, the length of the cavity plays an important role. According to Rossiter [54], the oscillations generated are driven by the vortices from the shear layer. The wave length of this periodic oscillation is usually close to the cavity length or $\frac{1}{N}$ of the cavity length. The oscillation of the shear layer is confined within a narrow region near the straight line between the leading and trailing edge of the cavity. The recirculation flow inside the cavity is usually relatively quiescent and the interaction between the shear layer and flow inside the cavity is weak. In a cavity with shear-layer mode, the shear layer spans the mouth of the cavity and stagnates at the downstream wall. Both fluid-resonant and fluid-dynamic regimes can be found in the cavity with shear-layer mode. When the shear layer oscillates in the shear layer mode, multiple discrete and high magnitude peaks will be present in the pressure spectra. These peaks are the cavity tones. There is usually one tone with higher magnitude than the rest of the spectrum as it so that it possesses most of the energy. This tone is referred to as the dominant tone or the fundamental frequency. Karamcheti [33] discovered that the frequency of the dominant tone is inversely proportional to the cavity length. As the length or depth of the cavity (relative to the upstream boundary-layer thickness) and/or Mach and Reynolds numbers is increased, there is a substantial change in the behaviour of the cavity oscillations. Under these conditions, the flow is characterized by a large-scale shedding from the cavity leading edge. As noted in the introduction, Gharib and Roshko [23] were the first to understand this transition in detail, and used the term wake mode to describe the resulting flow regime. The shed vortex has dimensions of nearly the cavity size, and as it is forming, irrotational free-stream fluid is directed into the cavity, impinging on the cavity base. The vortex is shed from the leading edge and

ejected from the cavity in a violent event. The vortex is large enough to cause flow separation upstream of the cavity during its formation, and again in the boundary layer downstream of the cavity as it convects away.

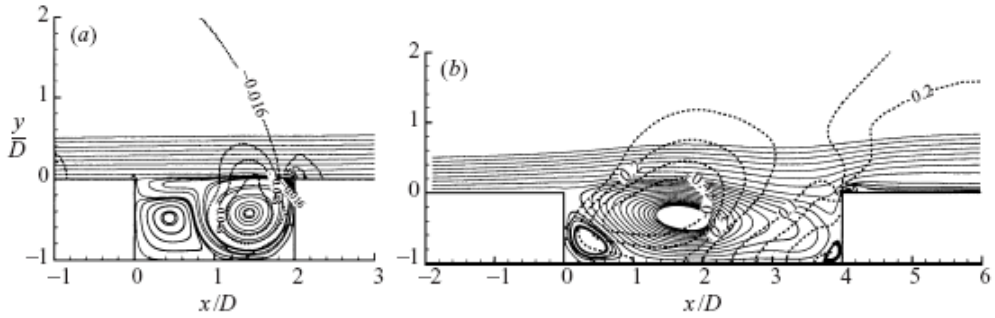

Figure 2.14: Time-averaged flow for (a) shear-layer mode and (b) wake mode. Mean streamlines (solid lines) are superposed on contours of contant C_p (dashed lines) [55]

Figure 2.14 contrasts the time-averaged flow for runs shear-layer mode and wake mode. The mean streamlines in the wake mode are significantly deflected above the cavity, and show that on average the boundary layer upstream of the cavity sees an adverse pressure gradient. On average the flow in the cavity is strongly recirculating, and there is an impingement of the recirculating flow on the rear wall. The region of high pressure near the back corner of the cavity resembles that observed by Fox [20] in his high-drag flow regime. Variations in the average coefficient of pressure are also quite large, reaching a minimum of about -0.5 where the flow is expanding into the cavity, to about 0.3 in the impingement region on the rear step.

2.4 Cavity-related flow oscillations

The understanding of cavity-related flow oscillations was simplified by Rossiter and Naudascher [51]. They divides them into three categories:

2.4.1 Fluid-elastic oscillations

They occur when a cavity surface itself is forced into oscillation 2.15. In other words, this regime encompasses flows that are affected by the elastic boundaries of the cavity.

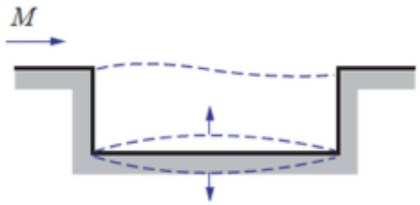

Figure 2.15: Fluid-resonant oscillations [18]

2.4.2 Fluid-resonant oscillations

In 1958-62, Plumblee et al. [49] proposed that the periodic pressure fluctuations in cavities are due to an acoustic resonance excited by the unsteadiness in the turbulent boundary layer approaching the cavity.

These are caused when a self sustaining oscillation in the flow has a wavelength of the same order as one of the cavity dimensions. This regime couples the acoustic modes of the cavity and shear layer over the deeper cavities and for the cavities subject to high Mach number flow.

2.4.3 Fluid-dynamic oscillations

These are related to the cavity feedback resonance mechanism. This regime involves shear-layer instability amplification due to feedback from interaction of the shear layer. These interactions occurs for low-speed flow past shallow cavities.

CHAPTER 3

COMPUTATIONAL AERO-ACOUSTICS

3.1 Generalities

Aerodynamic noise occurs because of two basically different phenomena. The first is impulsive noise, which is a result of moving surfaces or surfaces in non-uniform flow conditions. The displacement effect of an immersed body in motion and the non-stationary aerodynamic loads on the body surface generate pressure fluctuations that are radiated as sound. This kind of noise is deterministic and relatively easy to extract from aerodynamic simulations because the required resolution in space and time to predict the acoustics is similar to the demands from the aerodynamic computation.

The other noise mechanism is the result of turbulence and therefore arises in nearly every engineering application. Turbulence is by its very nature stochastic and therefore has a broad frequency spectrum. Interestingly enough, turbulent energy is converted into acoustic energy. Athird phenomenon is the case of combustion noise,which is a result of the chemical reactions and the subsequent introduction of energy into the flow.

Like Computational fluid dynamics (CFD), the sound generated by fluid flows, is an area of research that has received an increasing amount of attention during the past decade. Most of the research has been aimed at high-Mach-number applications, with jet noise being the most typical case of interest. For a long time the works was mostly based on analytical and experimental studies, but the astonishing advances in computer technology have made a numerical approach feasible. That approach is

called Computational Aero-Acoustics (CAA),

A variety of approaches are available to compute the flow data and to estimate the radiated noise from the flow. Computational techniques for flow-generated sound can be classified into two broad categories:

1. The direct approach computes the sound together with its fluid dynamic source field by solving the governing equations without modelling, this approach needs high quality grids. Direct approach are comparable to the Direct Numerical Simulation (DNS) in the Computational Fluid Dynamics (CFD).

2. In the hybrid approach, the computation of flow is decoupled from the computation of sound, the sound sources are extracted from the turbulence solved in the fluid dynamic simulation, which can be performed during a post-processing stage based on Aero-Acoustic Analogy. The problems that exhibit a one-way coupling between the flow and the acoustics. In the case of a one-way coupling the flow is independent of the acoustic part, hence no energy is fed back into the flow from the acoustic wave propagation. An advantage behind one-way coupled problems is that they can be separated into two different problems, one part being the flow induced source field while the other one is propagation of sources.

Figure 3.1 shows the main computational approaches used to evaluating the sound field generated by turbulent flows.

The far-field sound is obtained by integral or numerical solutions of acoustic analogy equations using computed source field data. From the Figure 3.2, the flow region is dominated by hydrodynamic phenomena. The pressure fluctuations which are present in this region is due to turbulence or large structures. Consider a source region of characteristic length scale L_{source} containing individual sources (eddies) of size l_{ed}. The far field is a region where the turbulence is less and the mean flow field is typically homogeneous. The far field and the source region is separated by a distance d. The only phenomena in this region is acoustic wave propagation. In the integral forms of acoustic analogies, the use of leading-order terms in an acoustic far-field expansion (with respect to $\frac{\lambda_{ac}}{d}$, where λ_{ac} is the acoustic wavelength) leads to much simpler evaluations of sound. For small amplitudes and low Mach numbers M, far-field can be described by a linear homogeneous wave equation. The near-field which is overlapped by the other two regions. This region becomes important as both hydrodynamics and acoustics are present. A source region is said to be acoustically compact if its extent is much smaller than the acoustic wavelength, or $\frac{l_{ed}}{\lambda_{ac}} \ll 1$ or $\frac{L_{source}}{\lambda_{ac}} \ll 1$. Given that

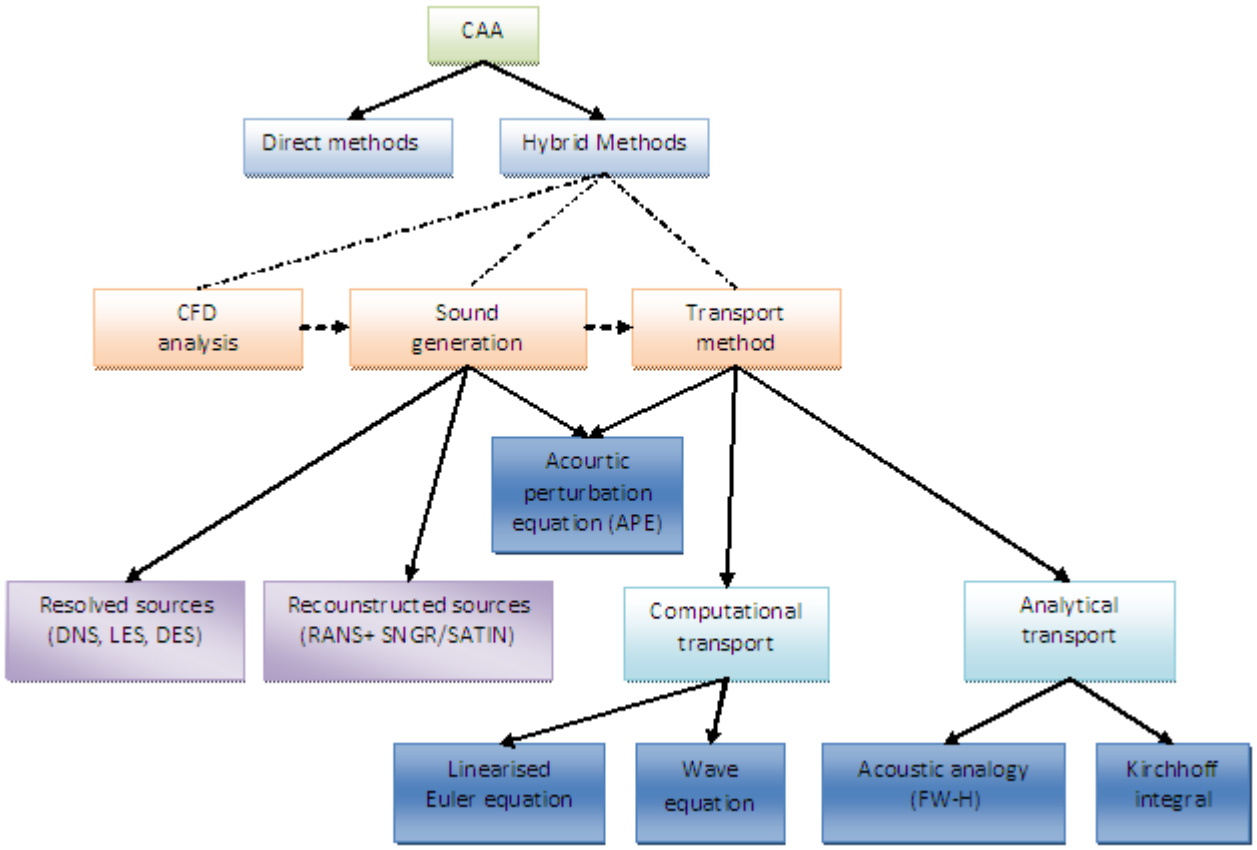

Figure 3.1: Noise prediction methods.

$\lambda_{ac} = \frac{l_{ed}}{M}$, it is apparent that low Mach number flows are more likely to be acoustically compact [71].

The pressure perturbations $p^{'}$ ($p^{'} = p - p_0$) which propagate as waves and which can be detected by the human ear. For harmonic pressure fluctuations the audio range is:

$$20Hz \leq f \leq 20kHz \tag{3.1}$$

The Sound Pressure Level (SPL) measured in decibel (dB) is defined by:

$$SPL = 20\log_{10}(\frac{p^{'}_{rms}}{p_{ref}}) \tag{3.2}$$

where $p_{ref} = 2 \times 10^{-5} Pa$ for sound propagating in gases The sound intensity $\langle I \rangle = \langle I.n \rangle$ is defined as the time averaged energy flux associated to the acoustic wave, propagating in direction n.

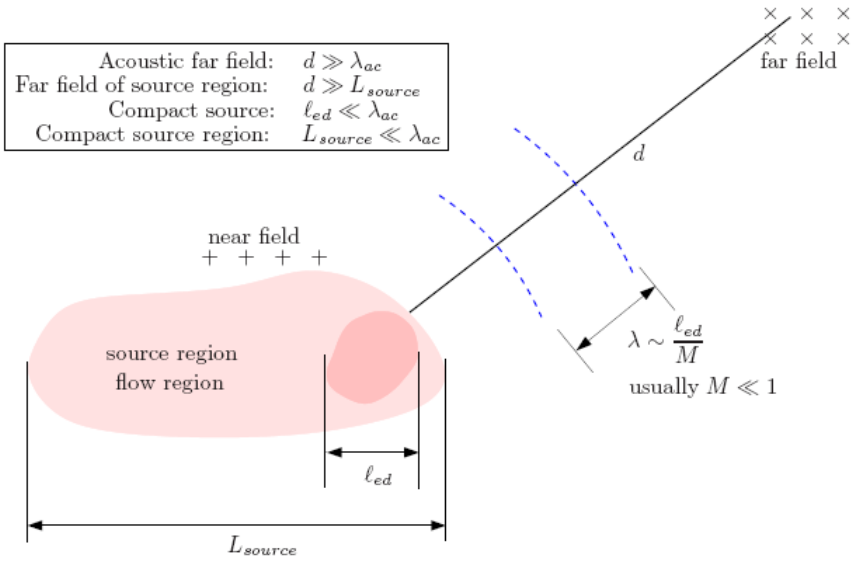

Figure 3.2: Schematic of sources and sound scales [71]

The intensity of radiation is the rate at which energy is transmitted across a unit area of a plane parallel to that wave front. For a simple harmonic wave of frequency f the intensity I is given by the relation:

$$I = \frac{1}{2}\frac{P^2}{\rho_e a} \tag{3.3}$$

where a is the local speed of sound, P the maximum amplitudes of the pressure , ρ_e is the equilibrium value of the local density of the medium and I is expressed in ergs per square centimetre per second. in the decibel scale the intensity is given by its level relative to the reference level 10^{-9} arg per centimetre per second. Thus,

$$I_{db} = 10\log_{10}\frac{I}{I_{ref}} \tag{3.4}$$

where I_{db} is the intensity in decibels and the reference intensity $I_{ref} = 10^{-12} W m^{-2}$ in air, $\log_{10}$ erg square centimeter per second. Hence,

$$I_{db} = 90 + 10\log_{10} I \tag{3.5}$$

3.2 Acoustic analogies

The technique of the acoustic analogies was established by Sir James Lighthill [40] who published in 1952 his " acoustic analogy ". This represents one of the first theories on

aerodynamic noise generation for describing the radiation of the sound field generated by a turbulent flow and since then multiple times used for aero-acoustic problems. Lighthill (1952) transformed the Navier-Stokes and continuity equations to form an exact, inhomogeneous wave equation (namely the Lighthill equation 3.12) whose source terms are important only within the turbulent region. He argued that sound is a very small component of the whole motion and that, once generated, its back-reaction on the main flow can usually be ignored. The properties of the unsteady flow in the source region may then be determined by neglecting the production and propagation of the sound, a reasonable approximation if the Mach number M is small, and there are many important flows where the hypothesis is obviously correct, and where the theory leads to unambiguous predictions of the sound. Lighthill was initially interested in solving the problem, illustrated in Figure 3.3-a, of the sound produced by a turbulent nozzle flow. However, his original theory actually applies to the simpler situation shown in Figure 3.3-b, in which the sound is imagined to be generated by a finite region of rotational flow in an unbounded fluid. This avoids complications caused by the presence of the nozzle. The fluid is assumed to be at rest at infinity, where the mean pressure, density, and sound speed are respectively equal to p_0, ρ_0, a_∞. Lighthill compared the equations for the production of acoustic density fluctuations in the real flow with those in an ideal linear acoustic medium that coincides with the real fluid at large distances from the sources.

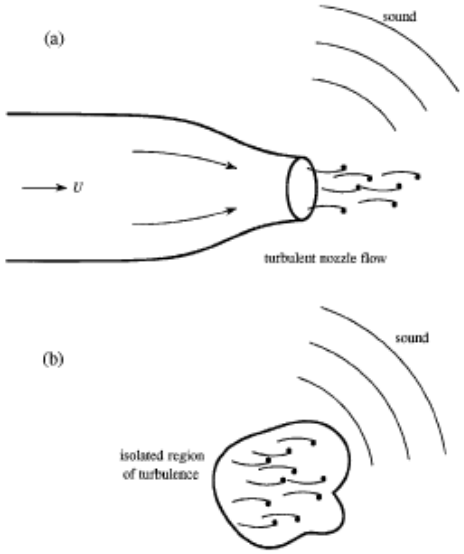

Figure 3.3: Lighthill's Analogy for a Turbulent Jet

The theory formulated by Lighthill in 1952 is considered as the starting point of

modern Aero-Acoustics. It relies on an analogy between the full non linear flows and the linear theory of acoustics. The conservation equations are rewritten to form the following inhomogeneous wave equation.

3.2.1 Lighthill's acoustic analogy

Lighthill considered that the acoustic waves result from small scale, localised turbulent structures, and that they propagate in an homogeneous medium at rest where density ρ and speed of sound a_∞ are constant. Acoustic fluctuations are then governed by the classical acoustic wave equation outside of the source zone. Considering the conservation of mass and momentum equations, Lighthill gives a reformulation of the fluid dynamics equations in such a way that he obtains a wave equation for the acoustic density fluctuations with a source term on the right hand side.

The first step consists to derive the mass conservation equation

$$\frac{\partial \rho}{\partial t} + \frac{\partial}{\partial x_i}\left(\rho u_i\right) = 0 \tag{3.6}$$

with respect to time. The following equation is obtained:

$$\frac{\partial^2 \rho}{\partial t^2} + \frac{\partial^2}{\partial t \partial x_i}\left(\rho u_i\right) = 0 \tag{3.7}$$

Then the term $a_\infty^2 \frac{\partial \rho}{\partial x_i}$ is introduced in each side of the momentum conservation equation (in the conservative form):

$$\frac{\partial}{\partial t}\left(\rho u_i\right) + \frac{\partial}{\partial x_j}\left(\rho u_i u_j\right) = -\frac{\partial}{\partial x_j}\left(P\delta_{ij} - \tau_{ij}\right) \tag{3.8}$$

- δ_{ij}= tensor of Kronecker
- τ_{ij}= viscous stress tensor

$$\frac{\partial}{\partial x_j}\left(P\delta_{ij}\right) = \frac{\partial P}{\partial x_i} \tag{3.9}$$

It comes:

$$\frac{\partial}{\partial t}\left(\rho u_i\right) + a_\infty^2 \frac{\partial \rho}{\partial x_i} = -\frac{\partial}{\partial x_i}\left(\rho u_i u_j + \left(P - a_\infty^2 \rho\right)\delta_{ij} - \tau_{ij}\right) \tag{3.10}$$

By taking the divergence of the equation 3.10:

$$\frac{\partial^2}{\partial x_i \partial t}\left(\rho u_i\right) + a_\infty^2 \Delta \rho = -\frac{\partial^2}{\partial x_i \partial x_j}\left(\rho u_i u_j + \left(P - a_\infty^2 \rho\right)\delta_{ij} - \tau_{ij}\right) \tag{3.11}$$

and then, substracting 3.7, the wave equation is obtained for the acoustic density:

$$\frac{\partial^2 \rho}{\partial t^2} - a_\infty^2 \Delta \rho = \frac{\partial^2 T_{ij}}{\partial x_i \partial x_j} \tag{3.12}$$

where ρ is the density, a_∞ is the ambient sound speed and $T_{ij} = \rho u_i u_j + \left(P - a_\infty^2 \rho\right) \delta_{ij} - \tau_{ij}$ is known as the Lighthill stress tensor, u_i p, τ_{ij} being the velocity components, the pressure and the viscous stresses respectively.

No assumptions has been made at this point and Eq. 3.12 is exact. A distinction has been made between the sound sources and the propagation of sound sources. The left hand side is an ordinary wave operator whereas the right hand side is the acoustic source terms. For Lighthill's equation to be applicable the right hand side should be known as well as decoupled from the acoustic field. From eq. 3.12, three fundamental processes of noise sources can be identifyed in a turbulent flow:

- the unsteadiness of the non linear convective forces included in the tensor $\rho u_i u_j$ (and more generally, in the Reynolds stresses tensor), can be neglected except where the motion is turbulent.
- the so-called "entropy noise", which is present when transformations are no more isentropic or when the flow is not homoentropic $\left(\frac{ds}{dt} \neq 0\right)$ In these cases: $P - a_\infty^2 \rho = \rho \left(a^2 - a_\infty^2\right) \neq 0$
- the fluctuations of the viscous stress tensor τ_{ij}, is linear in the perturbation quantities, and properly accounts for the attenuation of the sound; in most applications the Reynolds number in the source region is very large.

Noise computation using Lighthill's equation with inclusion of mean flow - acoustics Lighthill's equation is used to compute the noise produced by subsonic flows. The objective is to show that, although this equation is based on a wave equation in a medium at rest, mean flow effects on sound propagation, included in Lighthill's source term, can be properly taken into account by numerical approches. The source terms are evaluated from the unsteady compressible flow motion equations, which provide also a reference sound field.

3.2.2 The solution of the Lighthill equation in free space

The use of the integral formalism is very convenient to obtain Lighthill's equation solution.

3.2.2.1 Definition of Green's function

The Green function is the solution of the inhomogeneous linear differential equation for which the inhomogenity is concentrated at one point, both in time and space. From a mathematical point of vue, the Green function G corresponds to the system response to a pulse. For the present inhomogeneous wave equation:

$$\frac{\partial^2 G}{\partial t^2} - a_0^2 \frac{\partial^2 G}{\partial x_i^2} = \delta\left(\overrightarrow{x} - \overrightarrow{y}\right)\delta(t-\tau) \tag{3.13}$$

The Dirac pulse δ is produced at the source point $\overrightarrow{y}$ at time τ, and the Green function G is determined at the observation $\overrightarrow{x}$ point at time t, the Green function is generally noted G_0.

3.2.2.2 Properties of the Green function

- The Green function (and a fortiori G_0) has to respect the causality condition, occur after the pulse has been released. This implies:

$$\left.\begin{array}{l} G\left(\overrightarrow{x},t/\overrightarrow{y},\tau\right)=0 \\ \frac{\partial}{\partial t}G\left(\overrightarrow{x},t/\overrightarrow{y},\tau\right)=0 \end{array}\right\} t<\tau \tag{3.14}$$

- Another important point is that the Green function respects the reciprocity relationship:

$$G\left(\overrightarrow{x},t/\overrightarrow{y},\tau\right)=G\left(\overrightarrow{y},-\tau/\overrightarrow{x},-t\right)(interchangeability of the source and the observer) \tag{3.15}$$

It is then possible to show that the Green function is the solution of the following equation :

$$\frac{\partial^2 G}{\partial t^2} - a_\infty^2 \frac{\partial^2 G}{\partial x_i^2} = \delta\left(\overrightarrow{x} - \overrightarrow{y}\right)\delta(t-\tau) \tag{3.16}$$

$\overrightarrow{x} \leftrightarrow \overrightarrow{y} and t \leftrightarrow \tau$ which is a direct consequence of the symmetry of the Dirac function $\delta(t-\tau)$, of the reciprocity relationship, and of the interchangeability of the variables.

3.2.2.3 Free space Green's function

To determine G_o, we first consider the Fourier transform of G_o, defined by:

$$\hat{G}_0 = \int_{-\infty}^{+\infty} G_0 \, e^{-j\omega t} dt \tag{3.17}$$

From Eq. 3.16:

$$-a_\infty^2 \left[\frac{\partial^2 \hat{G}_0}{\partial x_i^2} + k^2 \hat{G}_0 \right] = \int_{-\infty}^{+\infty} \delta\left(\vec{x} - \vec{y}\right) \delta(t-\tau) e^{-j\omega t} dt \tag{3.18}$$

with $k = \frac{w}{a_\infty}$ and then As $\int_{-\infty}^{+\infty} \delta(t-\tau) e^{-j\omega t} dt = e^{-j\omega\tau}$
it yields:

$$\frac{\partial^2 \hat{G}_0}{\partial x_i^2} + k^2 \hat{G}_0 = -\frac{1}{a_\infty^2} \delta\left(\vec{x} - \vec{y}\right) e^{-j\omega\tau} \tag{3.19}$$

The free field Green function can then be defined in the temporal domain

$$G_0\left(\vec{x}, t / \vec{y}, \tau\right) = \frac{1}{4\pi a_\infty^2} \delta\left(t - \tau \frac{r}{a_\infty}\right) \tag{3.20}$$

with $r = \left|\vec{x} - \vec{y}\right|$ and $t = \frac{r}{a_\infty}$ retarded time (transit time from the source to the observer)

3.2.2.4 Solution of the Lighthill equation

Let us at first recall the equation giving the acoustic field (characterized by the acoustic density r) created by a source located at the point $\vec{y}$ at time t (Lighthill's equation)

$$\frac{\partial^2 \rho}{\partial t^2} - a_\infty^2 \Delta\rho = \frac{\partial^2 T_{ij}\left(\vec{y}, \tau\right)}{\partial x_i \partial x_j} \tag{3.21}$$

which can also be written as, according to the reciprocity theorem

$$\frac{\partial^2 \rho}{\partial \tau^2} - a_\infty^2 \frac{\partial^2 \rho}{\partial {y_i}^2} = \frac{\partial^2 T_{ij}\left(\vec{y}, \tau\right)}{\partial y_i \partial y_j} \tag{3.22}$$

Moreover, we have seen that

$$\frac{\partial^2 G_0}{\partial \tau^2} - a_\infty^2 \frac{\partial^2 G_0}{\partial y_i^2} = \delta\left(\vec{x} - \vec{y}\right) \delta(t-\tau) \tag{3.23}$$

it yields

$$\frac{\partial^2 G_0}{\partial \tau^2}\rho - a_\infty^2 \rho \frac{\partial^2 G_0}{\partial y_i^2} - G_0 \frac{\partial^2 \rho}{\partial \tau^2} + a_\infty^2 G_0 \frac{\partial^2 \rho}{\partial {y_i}^2} = \begin{array}{l} \rho\left(\overrightarrow{y},\tau\right)\delta\left(\overrightarrow{x}-\overrightarrow{y}\right)\delta(t-\tau) \\ -G_0\left(\overrightarrow{x},t/\overrightarrow{y},\tau\right)\frac{\partial^2 T_{ij}(\overrightarrow{y},\tau)}{\partial y_i \partial y_j} \end{array} \tag{3.24}$$

By integrating over a volume V (with respect to $\overrightarrow{y}$ and in time, from t_0 to t, where t_0 is the temporal origin for the observer, and then can be associated to the initial condition of the phenomenon for the observer (for instance the time at which the signal emitted by the source at the time τ is received by the observer), one obtains:

$$\begin{array}{l} \int_{t_0}^{t}\iiint_V \left[\frac{\partial^2 G_0}{\partial \tau^2}\rho - G_0\frac{\partial^2 \rho}{\partial \tau^2}\right] d\overrightarrow{y}\,d\tau - a_\infty^2 \int_{t_0}^{t}\iiint_V \left[\rho\frac{\partial^2 G_0}{\partial y_i^2} - G_0\frac{\partial^2 \rho}{\partial {y_i}^2}\right] d\overrightarrow{y}\,d\tau = \\ \int_{t_0}^{t}\iiint_V \rho\left(\overrightarrow{y},\tau\right)\delta\left(\overrightarrow{x}-\overrightarrow{y}\right)\delta(t-\tau) d\overrightarrow{y}\,d\tau - \int_{t_0}^{t}\iiint_V G_0\left(\overrightarrow{x},t/\overrightarrow{y},\tau\right)\frac{\partial^2 T_{ij}(\overrightarrow{y},\tau)}{\partial y_i \partial y_j} d\overrightarrow{y}\,d\tau \end{array} \tag{3.25}$$

According to the following property of the Dirac function
$\int g(a)\delta(b-a)da = g(b)$ we have
$\int_{t_0}^{t}\iiint_V \rho\left(\overrightarrow{y},\tau\right)\delta\left(\overrightarrow{x}-\overrightarrow{y}\right)\delta(t-\tau) d\overrightarrow{y}\,d\tau = \rho\left(\overrightarrow{x},t\right)$
and then

$$\rho\left(\overrightarrow{x},t\right) = \begin{array}{l} \int_{t_0}^{t}\iiint_V G_0\left(\overrightarrow{x},t/\overrightarrow{y},\tau\right)\frac{\partial^2 T_{ij}(\overrightarrow{y},\tau)}{\partial y_i \partial y_j} d\overrightarrow{y}\,d\tau \\ +\int_{t_0}^{t}\iiint_V \left[\frac{\partial^2 G_0}{\partial \tau^2}\rho - G_0\frac{\partial^2 \rho}{\partial \tau^2}\right] d\overrightarrow{y}\,d\tau \text{.....(a)} \\ -a_\infty^2 \int_{t_0}^{t}\iiint_V \left[\rho\frac{\partial^2 G_0}{\partial y_i^2} - G_0\frac{\partial^2 \rho}{\partial {y_i}^2}\right] d\overrightarrow{y}\,d\tau \text{.....(b)} \end{array} \tag{3.26}$$

Partial integration of (a) with respect to time
We have
$\rho\frac{\partial^2 G_0}{\partial \tau^2} - G_0\frac{\partial^2 \rho}{\partial \tau^2} = \frac{\partial}{\partial \tau}\left(\rho\frac{\partial G_0}{\partial \tau}\right) - \frac{\partial \rho}{\partial \tau}\frac{\partial G_0}{\partial \tau} - \left[\frac{\partial}{\partial \tau}\left(G_0\frac{\partial \rho}{\partial \tau}\right) - \frac{\partial G_0}{\partial \tau}\left(\frac{\partial \rho}{\partial \tau}\right)\right] = \frac{\partial}{\partial \tau}\left[\rho\frac{\partial G_0}{\partial \tau} - G_0\frac{\partial \rho}{\partial \tau}\right]$
and then

$$(a) = \int_{t_0}^{t}\iiint_V \frac{\partial}{\partial \tau}\left[\rho\frac{\partial G_0}{\partial \tau} - G_0\frac{\partial \rho}{\partial \tau}\right] d\overrightarrow{y}\,d\tau = \begin{array}{l} \left[\iiint_V \left(\rho\frac{\partial G_0}{\partial \tau} - G_0\frac{\partial \rho}{\partial \tau}\right) d\overrightarrow{y}\right]_{\tau=t} \text{.....}(\alpha) \\ -\left[\iiint_V \left(\rho\frac{\partial G_0}{\partial \tau} - G_0\frac{\partial \rho}{\partial \tau}\right) d\overrightarrow{y}\right]_{\tau=t_0} \text{.....}(\beta) \end{array}$$

According to the causality condition, the term (a) is equal to zero: t_0 write $t = \tau$ has not physical meaning, t_0 being the transit time of the signal from the source to the

observer (we can't have $t_0 < 0$), we have $t = \tau + t_0 \Rightarrow t > \tau$ and then $G_0 = 0$ and $\frac{\partial G_0}{\partial \tau} = 0$
Partial integration of (b) with respect to space We have
$\rho \frac{\partial^2 G_0}{\partial y^2} - G_0 \frac{\partial^2 \rho}{\partial y^2} = \frac{\partial}{\partial y}\left(\rho \frac{\partial G_0}{\partial y}\right) - \frac{\partial \rho}{\partial y}\frac{\partial G_0}{\partial y} - \left[\frac{\partial}{\partial y}\left(G_0 \frac{\partial \rho}{\partial y}\right) - \frac{\partial G_0}{\partial y}\left(\frac{\partial \rho}{\partial y}\right)\right] = \frac{\partial}{\partial y}\left[\rho \frac{\partial G_0}{\partial y} - G_0 \frac{\partial \rho}{\partial y}\right]$ and then (by Green's theorem)

$$(b) = -a_\infty^2 \int_{t_0}^{t} \iiint_V \frac{\partial}{\partial y_i}\left[\rho \frac{\partial G_0}{\partial y_i} - G_0 \frac{\partial \rho}{\partial y_i}\right] d\vec{y}\, d\tau = -c_0^2 \int_{t_0}^{t} \iint_\Sigma \left(\rho \frac{\partial G_0}{\partial y_i} - G_0 \frac{\partial \rho}{\partial y_i}\right) n_i d\sigma d\tau$$

The following form of the solution is obtained:

$$\rho\left(\vec{x},t\right) = \begin{array}{l} \int_{t_0}^{t} \iiint_V \frac{\partial^2 T_{ij}(\vec{y},\tau)}{\partial y_i \partial y_j} G_0\left(\vec{x},t/\vec{y},\tau\right) d\vec{y}\, d\tau \\ -a_\infty^2 \int_{t_0}^{t} \iint_\Sigma \left(\rho\left(\vec{y},\tau\right)\frac{\partial G_0}{\partial y_i} - G_0 \frac{\partial \rho(\vec{y},\tau)}{\partial y_i}\right) n_i d\sigma d\tau \ldots\ldots\ldots(C) \\ -\left[\iiint_V \left(\rho\left(\vec{y},\tau\right)\frac{\partial G_0}{\partial \tau} - G_0 \frac{\partial \rho(\vec{y},\tau)}{\partial \tau}\right) d\vec{y}\right]_{\tau=t_0} \ldots\ldots\ldots\ldots(d) \end{array} \tag{3.27}$$

- The surface integral (c) disappears for boundary conditions corresponding to those of the physical problem. That is of course the case of G_0 in a free space, as G_0 is defined in such a way that $G_0 \to 0$ when $r \to \infty$, and so on $\sum$.

- The term (d) represents the initial conditions effects at $t = t_0$. For a phenomenon not dependant of the initial condition, (steady state or permanent phenomenon, in statistical point of view), so that $t_0 \to -\infty$ (d) is equal to zero.

Then we have

$$\rho\left(\vec{x},t\right) = \int_{t_0}^{t} \iiint_V \frac{\partial^2 T_{ij}\left(\vec{y},\tau\right)}{\partial y_i \partial y_j} G_0\left(\vec{x},t/\vec{y},\tau\right) d\vec{y}\, d\tau \tag{3.28}$$

where the expression of the Green function in free space is
$G_0\left(\vec{x},t/\vec{y},\tau\right) = \frac{\delta\left(t-\tau-r/a_\infty\right)}{4\pi r a_\infty^2}$
with $r = \left|\vec{x} - \vec{y}\right|$ Then we have

$$\rho\left(\vec{x},t\right) = \frac{\partial^2}{\partial x_i \partial x_j} \iiint_V \frac{T_{ij}\left(\vec{y}, t - \frac{r}{a_\infty}\right)}{4\pi r c_0^2} d\vec{y} \tag{3.29}$$

This is strictly an alternative, integral equation representation of Equation 3.12; it provides a useful prediction of the sound only when T_{ij} is known.

Far field approximation In the acoustic far field, the only characteristic length scale of the phenomenon is the wavelength. It is then possible to the problem of the estimation of the space derivative ($\frac{\partial}{\partial x_i}$) at the observer by the estimation of the characteristic frequency (or the characteristic time) of the radiated noise.

Effectively, we have in the far field

- $\frac{1}{|\vec{x}-\vec{y}|} \cong \frac{1}{|\vec{x}|}$ as $|\vec{x}| \gg |\vec{y}|$
- secondly $\frac{1}{\partial x_i} \cong -\frac{x_i}{a_\infty |\vec{x}|}\frac{\partial}{\partial t}$

which allows to write, for the acoustic density

$$\rho(\vec{x},t) = \frac{x_i x_j}{4\pi a_\infty^2 |\vec{x}|^2}\frac{1}{a_\infty^2}\frac{\partial^2}{\partial t^2}\iiint_V \frac{T_{ij}\left(\vec{y}, t-\frac{|\vec{x}|}{a_\infty}\right)}{|\vec{x}|}d\vec{y} \tag{3.30}$$

Hence, if viscous dissipation is neglected we make the approximation $T_{ij} \approx \rho_0 v_i v_j$

3.2.3 Curle's Analogy: the influence of solid boundaries

As an extension to Lighthill's acoustic analogy, Curle [13] proposed a formal solution to Lighthill's analogy in 1955 to include the influence of the solid static boundaries.

In practice, surfaces are often present in turbulent flows. The presence of surfaces strongly modify the sound production.

- changes in the radiated acoustic field in comparison with the previous case of free turbulent flows
- extension of the integral formulation to the case of wall-bounded turbulent flows

We assume a solid body, placed normally to a mean flow:

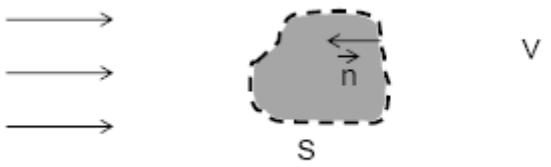

The volume V is the entire space occupied by the fluid, and V is delimited by a surface S enclosing the body. $\vec{n}$ is the outer normal to the volume V at the surface S, directed towards the body.

$$\rho\left(\overrightarrow{x},t\right) = \begin{array}{l} \int_{t_0}^{t} \iiint_V \frac{\partial^2[T_{ij}(\overrightarrow{y},\tau)]}{\partial y_i \partial y_j} G_0\left(\overrightarrow{x},t/\overrightarrow{y},\tau\right) d\overrightarrow{y}\, d\tau \\ -c_0^2 \int_{t_0}^{t} \iint_S \left[\rho\left(\overrightarrow{y},\tau\right)\frac{\partial G_0}{\partial y_i} - G_0 \frac{\partial \rho(\overrightarrow{y},\tau)}{\partial y_i}\right] n_i\, d\sigma d\tau \end{array} \tag{3.31}$$

and finally:

$$\rho\left(\overrightarrow{x},t\right) = \begin{array}{l} \int_{-\infty}^{t} \iiint_V T_{ij} \frac{\partial^2 G_0}{\partial y_i \partial y_j} d\overrightarrow{y}\, d\tau \\ -\int_{-\infty}^{t} \iint_S G_0 \frac{\partial}{\partial \tau}\left(\rho\, u_i\right) n_i\, ds d\tau \\ -\int_{-\infty}^{t} \iint_S \left(\rho\, u_i\, u_j + p\,\delta_{ij} - \tau_{ij}\right) \frac{\partial G_0}{\partial y_i} n_i\, ds d\tau \end{array} \tag{3.32}$$

Far field approximation First, with the use with the reciprocity theorem and secondly, with the symmetry property in time of Green's functions and using the far field approximation and by definition of G_0 we obtain

$$\rho\left(\overrightarrow{x},t\right) = \begin{array}{c} \frac{x_i x_j}{4\pi a_0^4 |\overrightarrow{x}|^3} \frac{\partial^2}{\partial t^2} \iiint_V \left[T_{ij}\right] d\overrightarrow{y} \\ -\iint_S \frac{1}{4\pi a_0^2 |\overrightarrow{x}|} \frac{\partial}{\partial t}\left[\rho\, u_i\right] n_i\, dS \\ +\frac{x_j}{4\pi a_0^3 |\overrightarrow{x}|^2} \frac{\partial}{\partial t} \iint_S \left[\rho\, u_i\, u_j + p\,\delta_{ij} - \tau_{ij}\right] n_i\, ds \end{array} \tag{3.33}$$

- the first integral (volumic integral) represents the noise due to the turbulence in the source volume, similarly to the case of a free turbulent flow ;
- the second integral (surfacic integral) results from a volume injection through the surface S enclosing the body, which can be due to a flow through a porous surface or to pulsations of the body ;
- the third integral (surfacic integral) results from the momentum flux through the surface S and from the surface stresses on S (pressure and viscosity forces)

Interpretation for a compact rigid body In this case, $u_i = 0$ at the surface. The only surface integral remaining is then simply the instantaneous force Fi exerted by

the flow on the body:

$$\rho\left(\vec{x},t\right)=\frac{x_i x_j}{4\pi a_0^4\left|\vec{x}\right|^3}\frac{\partial^2}{\partial t^2}\iiint_V\left[T_{ij}\right]d\vec{y}+\frac{x_j}{4\pi a_0^3\left|\vec{x}\right|^2}\frac{\partial}{\partial t}\underbrace{\iint_S\left[p\,\delta_{ij}-\tau_{ij}\right]n_i\,ds}_{F_i} \tag{3.34}$$

3.2.4 Ffowcs-Williams Hawkings analogy

FH-W analogy is an extended version of Lighthill analogy. It introduces the so called source surfaces, which are taken into account when computing the sound pressure level at the observer. Those surfaces can be set as surfaces of solid body (impermeable) or as a any free surface located in domain (permeable). In contradiction to Lighthill analogy, FH-W analogy allows the motion of the bodies inside fluid domain, that fact extends its applicability to predict noise generated by rotors. Analogy is govern by equations below:

$$\frac{1}{a_0}\frac{\partial^2\left(\rho-\rho_0\right)}{\partial t^2}-\nabla^2\left(\rho-\rho_0\right)=\frac{\partial}{\partial t}\left[Q_n\,\delta(f)\right]-\frac{\partial}{\partial x_i}\left[L_i\,\delta(f)\right]+\frac{\partial^2}{\partial x_i\,\partial x_j}\left[T_{ij}H(f)\right] \tag{3.35}$$

Where Q_n and L_i are defined as:

$$Q_n=Q_i\,\hat{n}_i=\left[\rho_0 v_i+\rho(u_i-v_i)\right]\hat{n}_i \tag{3.36}$$

$$L_i=L_{ij}\,\hat{n}_i=\left[P_{ij}+\rho\,u_i\left(u_j-v_j\right)\right]\hat{n}_i \tag{3.37}$$

The source surface mentioned before(also called integration surface) is described as f(x,t)=0 and $\hat{n}_i=\nabla f$ is a unit normal vector pointed out from surface f. In equations 3.36 and 3.37 v_i denotes the velocity of surface f, while u_i is the velocity of the fluid at the integration surface. If the source surface is equal to the solid body surface then $u_i=v_i$. In equation 3.37 there is a compressible stress tensor:

$$P_{ij}=(p-p_0)\delta_{ij}-\tau_{ij} \tag{3.38}$$

Formulation 1A For a complex geometry it is hard to find the direct solution of equation 3.35. Therefore some numerical formulations of FH-W analogy were introduced. One of them is formulation 1A proposed by Farassant [19] [8]. It is suitable for moving solid bodies in fluid at rest. That formulation was developed to improve prediction of noise generated by helicopter rotor. The acoustic pressure $p'^{\text{Äô}}$ that is generated by

solid body with subsonic velocity, measured by observer in position x and time t is given by:

$$p^{'}(x,t) = p^{'}_{T}(x,t) + p^{'}_{L}(x,t) \tag{3.39}$$

$$4\pi p^{'}_{T}(x,t) = \int_{f-0} \left[\frac{\dot{Q}_n + Q_n}{r(1-M_r)^2} \right]_{ret} ds + \int_{f-0} \left[\frac{Q_n \left(r\dot{M}_r + a_0(M_r - M^2) \right)}{r^2(1-M_r)^3} \right]_{ret} ds \tag{3.40}$$

$$4\pi p^{'}_{T}(x,t) = \int_{f-0} \left[\frac{\dot{L}_r}{r(1-M_r)^2} \right]_{ret} ds + \int_{f-0} \left[\frac{L_r - L_m}{r^2(1-M_r)^3} \right]_{ret} ds + \int_{f-0} \left[\frac{L_r \left(r\dot{M}_r + a_0(M_r - M^2) \right)}{r^2(1-M_r)^3} \right]_{ret} ds \tag{3.41}$$

Where M denotes Mach number of a source, with components $M_i = \frac{v_i}{a_0}$, the dot $(.)$ means time derivative with respect to emission time τ. Other components of equations 3.40 and 3.41 are following:

$$\begin{gathered} M_r = M_i r_i \quad \dot{M}_r = \frac{\partial M_i}{\partial \tau} r_i \\ Q_n = Q_i \hat{n}_i \quad \dot{Q}_n = \frac{\partial Q_i}{\partial \tau} \hat{n}_i \quad Q_{\dot{n}} = Q_i \frac{\partial \hat{n}_i}{\partial \tau} \\ L_n = L_{ij} \hat{n}_i \quad \dot{L}_r = \frac{\partial L_i}{\partial r} \hat{r}_i \quad L_r = L_i \hat{r}_i \quad L_M = L_i M_i \end{gathered} \tag{3.42}$$

Subscript ret means that the integral is evaluated at the emission time. The retarded time equation has a form presented below:

$$g = \tau_{ret} - t + \frac{r}{a_0} = 0 \tag{3.43}$$

Where $r = |x - y(ret)|$ is a distance between observer and the source at the emission time.

CHAPTER 4

DOMAIN GENERATION METHODOLOGY

4.1 Introduction

The geometrical parameters of the cavity model in paper are displayed in Figure 4.1 (a- baseline Cavity geometry and b- wavy cavity geometry), they are taken from the computational domain of Garry Hughes and Laurent Dala [29]. Different surface modifications were simulated by varying the amplitude and frequency of surface waviness was constructed using OpenFOAM program.

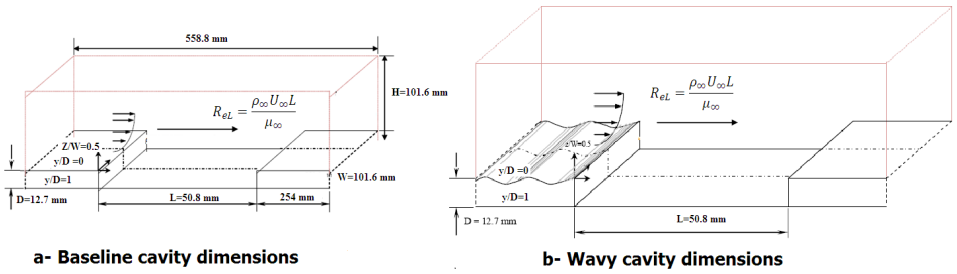

Figure 4.1: Cavity geometry reproduced from [29]

4.2 Open Field Operation And Manipulation - OpenFOAM

OpenFOAM [3] is a acronym for Open Source Field Operation And Manipulation. It is a C++ toolbox that provides a platform for the development of customized numerical solvers related to continuum mechanic problems using the finite volume method. It is released under the Open Software GNU General Public License [2]. The code was originally developed by Henry Weller at Imperial College in London. The commercial Computational Fluid Dynamic (CFD) codes StarCD [4] and Fluent (ANSYS [1]) also originates from this college.

Numerical analysis of aerospace and defence applications requires a significant level of code flexibility to make the desired changes to existing subroutines or to develop new routines. OpenFOAM consist of many solvers, utilities and libraries that provide an ideal platform of development. Its object oriented code architecture allows for re-use of existing code blocks and objects and therefore eases the overhead of new development. OpenFOAM provides a good alternative to commercial software since it has been extensivly validated and there is no direct costs involved to operate it.

In order to work with OpenFOAM, the user needs to be familiar with the file structure, since there is no Graphical User Interface (GUI). The general structure of OpenFOAM is divided into three main directories; a System, Constant and Initial and boundary conditions "0" directory Figure 4.2:

- The System directory contains at minimum the controlDict, fvSchemes, and fvSolution. The controlDict controls parameters such as start/end time, step size, when and what files to output etc. fvSchemes and fvSolution dictates what discretization schemes to use, equation solvers and tolerances respectively.
- In the constant directory, turbulence and material properties are specified. The file LESProperties contains the option to choose a LES turbulence model. transportProperties contains the possibility to specify the value of the kinematic viscosity ν. Editing the file turbulenceProperties enables changes in the constants of the different turbulence models. As shown in Figure 4.2, there is a yet another subfolder in the constant directory. This subfolder contains all information about the mesh and the only file to be edited is the file boundary. In this file, the user has to set the physical type of the different surface patches (wall, symmetryPlane, patch).

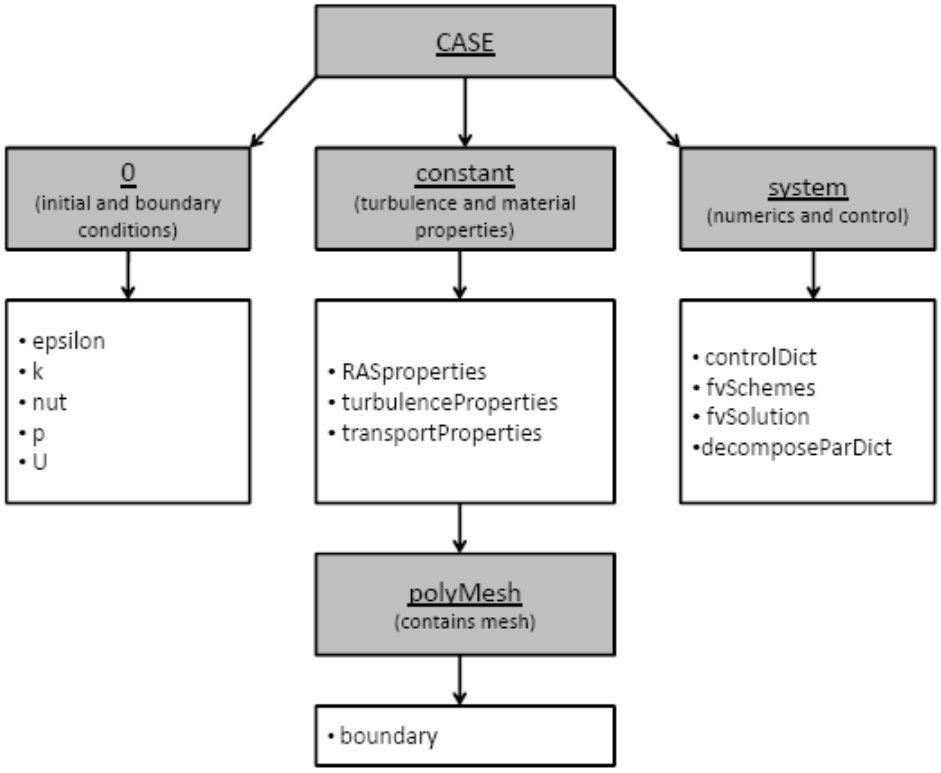

Figure 4.2: OpenFOAM case structure

- The "0" directory contains files in which the initial conditions for the different variables and surface patches can be specified.

More detailed information, especially regarding the different possibilities for adjustment, can be found in the OpenFOAM User Guide [3].

4.2.1 Spatial and Temporal Discretization

4.2.1.1 Spatial

The Poisson equation for pressure is solved by GAMG (Generalized Geometric-Algebraic Multi-Grid) algorithm, while the linear equation for velocity is solved by PBiCG algorithm (Preconditioned Bi-Conjugate gradient solver for asymmetric matrices). Linear interpolation is used to obtain the physical quantities at the surface centers of the cells. SnGradSchemes is a user defined variable in OpenFOAM that allows the user to chose what surface normal grad scheme to use. Gaussian integration is a second order discretization scheme and is defined in the fvSchemes dict together

with the choice of interpolation scheme. In the Gaussian integration values from cell centers need to be interpolated to face centers. A linear interpolation scheme is used for this.

4.2.1.2 Temporal

OpenFOAM provides a wide range of temporal discretization schemes varying in accuracy and computational cost. During a steady state simulation the SteadyState option can be specified in the fvSchemes for the time scheme, and the time derivative will be "switched off". For a transient problem the solution is time dependent and a solution will be found by a time-marching method. The Crank-Nicolson (CN) method averages properties between time steps where both the old and new values are used. CN uses a weighted average between spatial steps where for an equal contribution close resemblance can be found to central-differencing schemes. The Crank-Nicolson method is often used for parabolic equations. Crank-Nicolson is conditionally bounded and comes with a time constraint. Since it is not a pure explicit method CN does not have as strict of a time step for stability. The solver makes it possible to dynamically adjust the time step in runtime based on the specified maximum Courant-Friedrichs-Lewy (CFL) number, which reduces the initial relaxation time and find a suitable time step for temporal accuracy as well as stability.

$$CFL = \frac{|u| \triangle t}{\triangle x} \leqslant 1 \tag{4.1}$$

The CFL condition is a necessary condition for stability but does not ensure a stable solution.

4.2.2 Pressure and Velocity Coupling

PISO and SIMPLE are two algorithms commonly used in OpenFOAM to solve the equations for velocity and pressure. PISO is a semi-implicit method that stands for Pressure-Implicit Split Operator and is developed for transient problems. SIMPLE on the other hand, or Semi-Implicit Method for Pressure-Linked Equations, is a steady-state algorithm. PIMPLE is a merged version of the PISO-SIMPLE algorithms. Both SIMPLE and PISO are discretized using a staggered velocity field. H.K Versteeg [1995] [70] presents a grafic figure of the discretized volume where scalar variables are defined on the nodes (black dots) while velocities are defined between nodes in Figure 4.3.

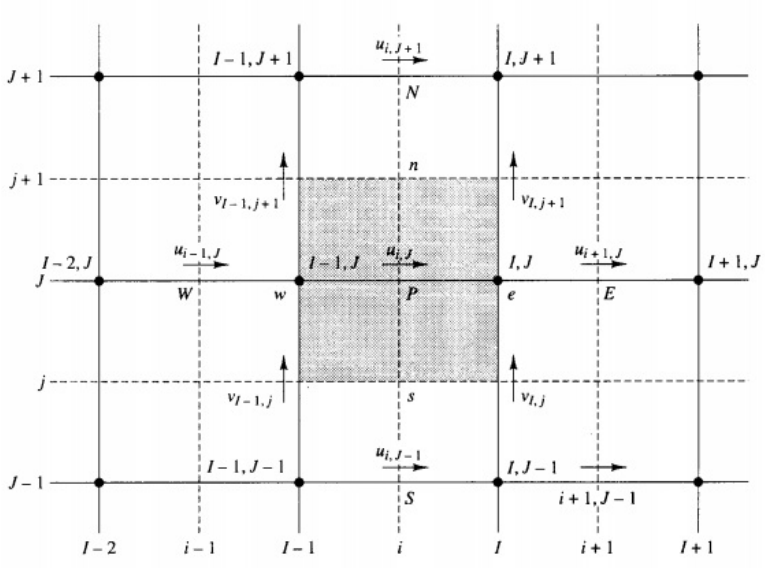

Figure 4.3: Staggered grid for velocity components

4.2.2.1 SIMPLE Algorithm

SIMPLE, or the Semi-Implicit Method for Pressure-Linked Equations, is a steadystate algorithm based on work by Patankar and Spalding (1972)[46]. The SIMPLE algorithm uses a guess-and-correct method [H.K Versteeg, 1995][70] where in its initial stage SIMPLE approximates the velocity field using the momentum equation and a guessed pressure field p^*. The discretized u- and v-momentum equations are:

$$\begin{aligned} a_{i,J}u^*_{i,J} &= \sum a_{nb}u^*_{nb} + (P^*_{I-1,J} - P^*_{I,J})A_{i,J} + b_{i,J} \\ a_{I,j}v^*_{I,j} &= \sum a_{nb}v^*_{nb} + (P^*_{I,J-1} - P^*_{I,J})A_{I,J} + b_{I,J} \end{aligned} \tag{4.2}$$

where $a_{i,J}$ and a_{nb} are coefficients. The correct pressure field p, relates to the guessed pressure field p^* and the correction, $p^{'}$, in the following way;

$$p = p^* + p^{'} \tag{4.3}$$

Many times under-relaxation is used to reduce the risk of divergence. Under-relaxation reduces the amount the guessed pressure field is corrected by $p^{'}$, and the new pressure field can be calculated in a following way

$$p^{new} = p^* + \alpha_p p^{'} \tag{4.4}$$

Here α_p is the under-relaxation factor and it is for the present case set to 0.33. From the guessed pressure field, and the discretized momentum equation u^* and v^* velocities

are solved for.

$$u = u^* + u' \quad v = v^* + v' \tag{4.5}$$

$$p^* = p \quad u^* = u \quad v^* = v \tag{4.6}$$

4.2.2.2 PISO Algorithm

The PISO (Pressure Implicit with Splitting of Operators) is an efficient method to solve the Navier-Stokes equations in unsteady problems. The main differences from the SIMPLE algorithm are the following:

- No under-relaxation is applied.
- The momentum corrector step is performed more than once.

PISO has shown to require less computational time over SIMPLE in order to converge the solution up to the exact same level of tolerance. The PISO algorithm is summarized in Figure 4.4. As it can be seen, the main characteristic of this coupling scheme is certainly the presence of not one, but two corrections on the pressure field. Another characteristic not shown on this figure is the fact that no under-relaxation is required. This last property partly explains the reduced computational cost of PISO over SIMPLE.

4.2.3 The creation of geometry and mesh

The geometry and the computational mesh was created in OpenFOAM software environment using the appropriate commands, checked in a graphical environment Paraview and subsequently modified or approved and then it went through the numerical calculation. The geometry and mesh is created directly by blockMesh command. The appropriate command creates geometry and mesh in a few steps:

- Creates points placed in a 3D coordinate system;
- Links these points into blocks;
- Divides the blocks into individual cells according to parameters specified by the user;
- Sets boundary conditions.

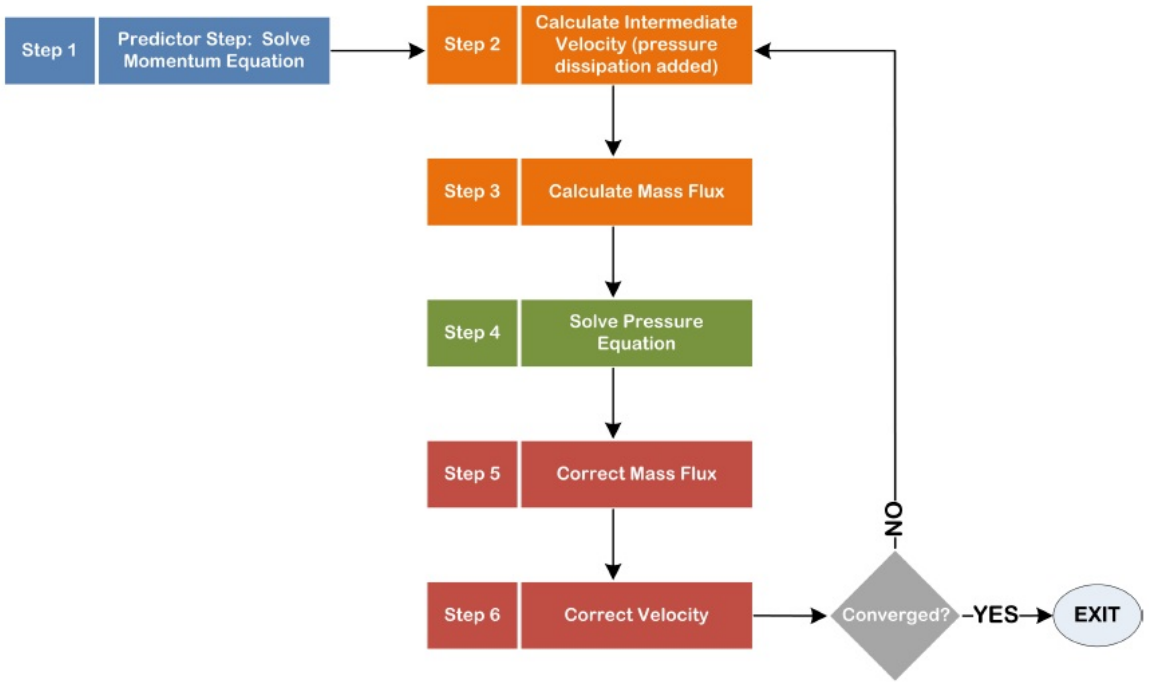

Figure 4.4: Representation of the PISO segregated algorithm for pressure-velocity coupling

4.2.4 Boundary Conditions

OpenFOAM has vast libraries of boundary conditions that can be used. Boundary conditions can also be augmented from existing source code or newly developed. three classes of boundary conditions are defined: basic, derived and constraint conditions.

4.2.4.1 Basic boundary conditions

are independent from any other utilities and all the mathematical equation to used this library is in its root source code. Example of this is the *fixedValue* condiction and the *zeroGradient* condictions ars shown in Figure 4.5.

the *fixedValue* condition enforced a fixed value on the boundary, while the *zeroGradient* condition obtains the boundary value from the internal node.

4.2.4.2 Derived boundary conditions

are dependent on either the basic boundary condition specification or an another external library. the *inletOutlet* condition is an example of an outlet derived boundary where a *fixedValue* condition is enforce on the boundary if the flux is out of the domain.

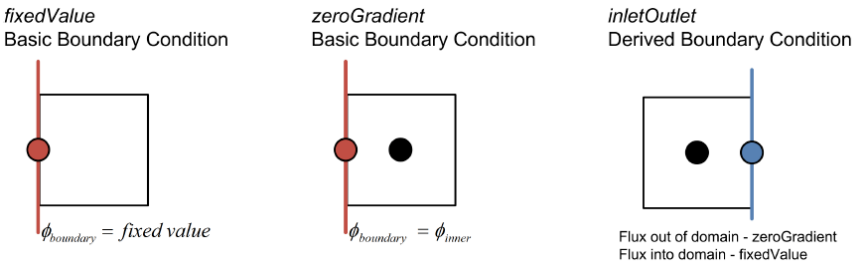

Figure 4.5: Boundary condition definition for *fixedValue*, *zeroGradient* and *inletOutlet*

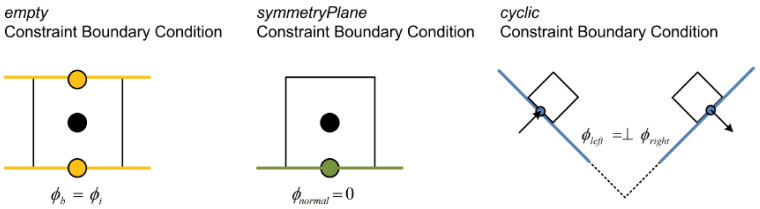

Figure 4.6: Boundary condition definition for *empty*, *symmetryPlane* and *cyclic*

4.2.4.3 Constraint type boundary conditions

allows for reduction of dimensions or computational domain due to axis-symmetry, symmetry or two dimensionality Figure 4.6. The *empty* condition allow for the reduction of dimensions where no solution is required on the empty patch. A *symmetryPlan* condition is used at the mirror line of a symmetrical object to reduce the size and extend of the computational domain. This condition sets all the normal components of vectors to zero. The *cyclic* condition requires that a pair of boundaries be identified and treats these patches as if it is physically connected. This allows for the reduction of the computational grid in axis-symmetrical cases.

Two special boundary conditions were also used as shown in Figure 4.7. This condition allows for less stringent pressure conditions on the outlet boundary where the boundary value assigned is a function of the inner node and a far-field ghost node. Interpolation between the inner node and the ghost node is used to obtain the value for the boundary.

4.2.5 Aero-Acoustics Implementation

Hybrid methods are applicable for problem with only one-way coupling between flow and acoustics. That is, the flow is independent of the acoustics. By doing this, the problem is divided into two sections, with one being the flow solution and other, the

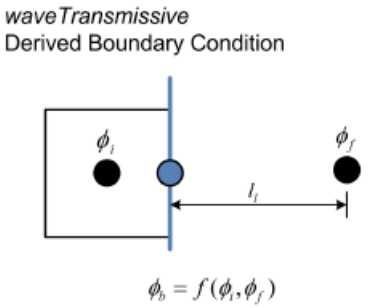

Figure 4.7: Boundary condition definition for *waveTranmissive*

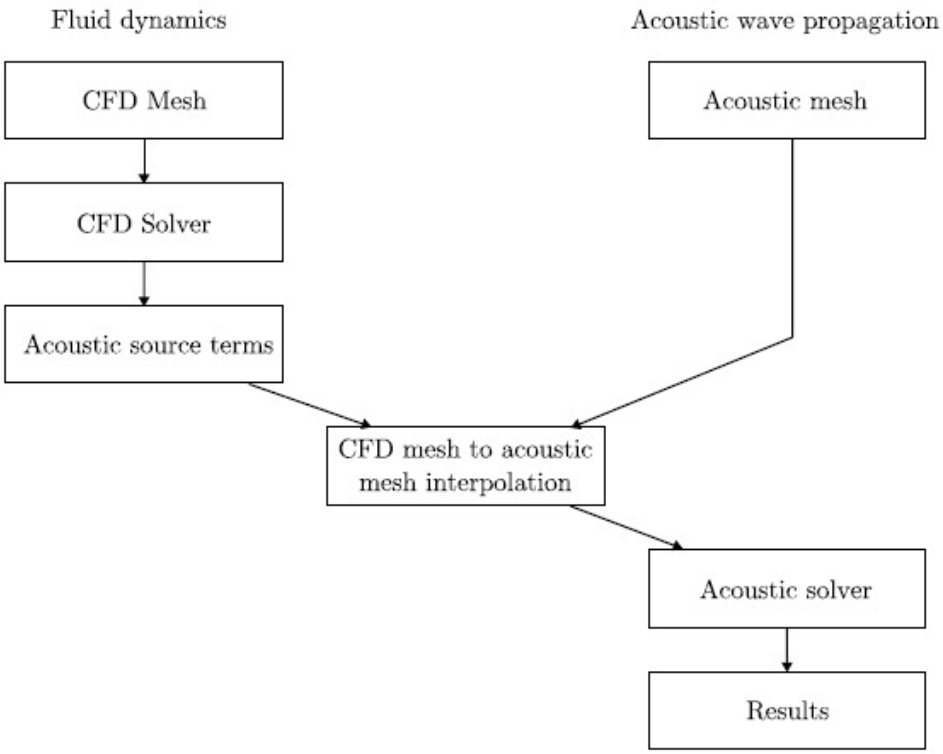

Figure 4.8: Overview of the implemented method

propagation of sound waves. The methodology is described in Figure 4.8. Implementing Curle's analogy to compute the sound region assumes that the generation of sound can be decoupled from its propagation . The aerodynamic quantities are transiently recorded using a CFD mesh. Since sound is the propagation of unsteady, small, pressure fluctuations it is of paramount importance that the mesh is fine enough to capture this phenomena. For the purpose of this work one mesh was used for both the CFD as well as the acoustic computation.

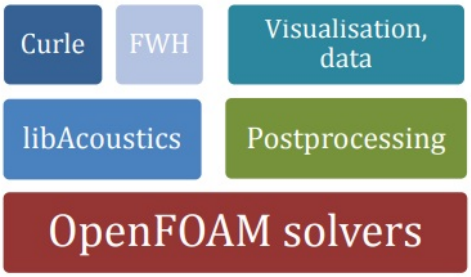

Figure 4.9: The hierarchy of the OpenFOAM solvers and the place of the libAcoustics library [16]

4.2.5.1 The architecture of the libAcoustics library

libAcoustics is on the same level as post-processing utilities of the package (see Fig.4.9) [16]. It was implemented in the OpenFOAM as dynamical library in real time together with solvers. The library can use both solution data and solver data when calculation continues and the last option is preferred because large amount of different information about solution is converted in specific files. These files are the result of applying the acoustic analogy and contain only pressure fluctuation at certain points (see Fig. 4.10) .

The simulation using libAcoustics library needs the following data and parameters [16]:

- User data. The user must define following input data before simulation: name of the patches or face sets, which are used for integration, names of the pressure and density fields, start and end time, frequency range, observer (microphone) position, sound speed, characteristic length, FastFourier Transform settings for obtaining SPL data. For instance, when using Curle analogy, user should set a type name "Curle" in functionObject dictionary.
- Force distribution on the surface of the body. This type of data is obtaining during the simulation and functionObject gets necessary pressure distribution and face normal vector using relevant OpenFOAM basic classes and object.
- Time derivative numerical scheme. The numerical scheme for boundary force time derivative can be of two different types: Euler and upwind.
- Sound observer settings. The reference pressure and observer position are saved in separate objects in the different class soundObserver and thus need to be

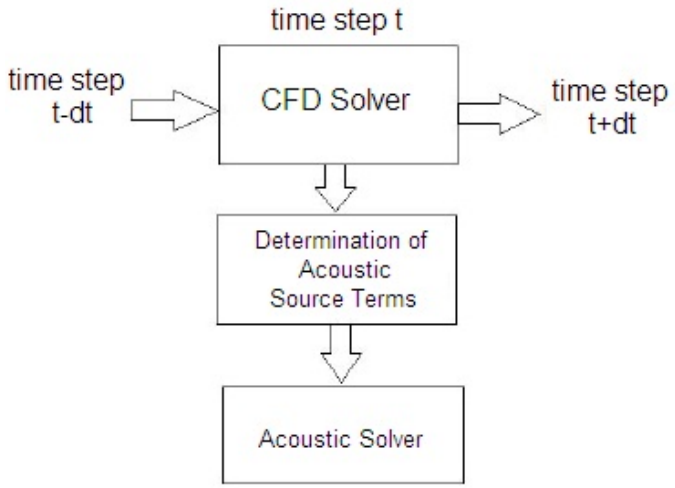

Figure 4.10: Solution methodology

set in separate sub-dictionary. The separation of the soundObserver data allows to generalize different types of analogies and enhance code re-use when new analogies will be implemented. Also in soundObserver sub-dictionary user must set parameters for objects of the Fast-Fourier Transform class FoamFftwDriver from third-party library Fftw3. The FoamFftwDriver process pressure fluctuations obtained from analogy and returns list of the frequencies and amplitudes for given acoustic pressure. Then SPL is calculated in the output file that is saved at the end.

- Saving data sequence. The library uses OFstream OpenFOAM class to save data on the hard drive. Pressure fluctuations and noise SPL data are saved in specific files for each observer.
- Parameters of parallel mode calculation. In the case of using parallel algorithms we need to take into account the following points: a) The patches could be in the different sub-domains; to provide simulations we need to go through all processors and collect all necessary data using special callings; b) Fast-Fourier-Transform and writing operations could be executed on a single processor.

4.2.5.2 Time to Frequency Domain Transformation

Since the acoustical solver works in frequency domain and the CFD solver works in the time domain the data transferred between the solvers (the acoustical source terms)

needs to be transformed. This is done by computing the Discrete Fourier Transform (DFT) of the source terms in each node. Computing the DFT directly from its definition is computationally very expensive. Instead an approximate algorithm is usually used. These algorithms are called the Fast Fourier Transform or FFT.

4.2.6 Running OpenFOAM codes in Parallel

The method of parallel computing used by OpenFOAM is known as domain decomposition, in which the geometry and associated fields are broken into pieces and allocated to separate processors for solution. The first step required to run a parallel case is therefore to decompose the domain using the decomposePar utility. There is a dictionary associated with decomposePar named decomposeParDict which is located in the system directory of the tutorial case. In this case, each processor executes the same program on its own set of data. At some stage each processor needs data that exists in other subdomains, then communication between processors is performed to synchronize the data.

4.2.7 Optimisation process

The concept is numerically optimised to achieve an optimum geometry of two-dimensional surface waviness. The process proved to be robust whether starting the optimisation from clean geometry. There are many optimisation approaches for different applications, from the method of trial-and-error to advanced adjoint optimisation algorithms. The most common is the genetic or evolutionary algorithm which is based on Darwin's theory of natural selection: only the fittest individuals survive and provide their genetic code to the following generation. The Single-Objective Optimization based on the OASPL is used to finding global solution with decreased the SPL tones. The flowchart of the optimisation loop is shown in Figure 4.11.

After obtaining the new mesh from the baseline geometry, simulation of the flow through the cavity is performed using pisoFoam solver. The optimisation is performed entirely within shall script. Geom. is the geometry Function which creation automatically a new geometries based on the two input (Amplitude and cycle). A automatic mesh method is set up by blockMesh mesher, witch is applied to each new geometry. the pisoFoam solver implemented in OpenFOAM are used to aerodynamic solver. The modules pass information along to each subsequent module in serial.

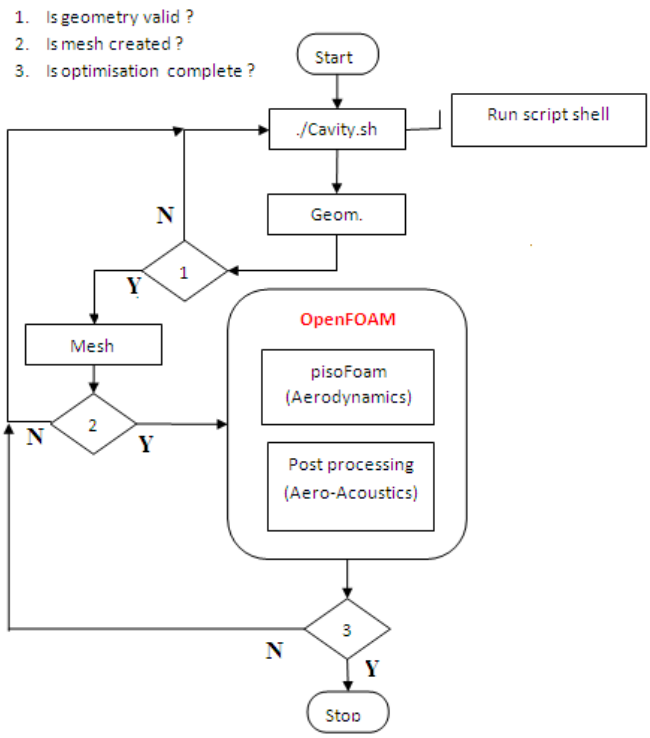

Figure 4.11: Single-objective optimization (SOO) methodology: evaluation and optimization

4.3 Two Dimensional simulations

All simulations were performed on the cavity of aspect ratio $L/D = 4$. Through out the work, the length of the cavity is maintained as 50.8 mm and depth of the cavity as 12.7 mm. Figure 4.12 illustrates the schematic diagram of two dimensional domain adopted to simulate cavity flows. The flow is from left to right hand side. The domain extends between $0 \leq x/D \leq 44$ and $-1 \leq y/D \leq 8$. The computational domain extends to 20D and 20D upstream and downstream of the cavity leading and trailing edges, respectively. The Table 4.1 summaries the details related to the geometry of the two dimensional cavity.

4.3.1 Computational Mesh

The mesh is a very important part of the calculation; in the evaluation of a CFD simulation it is necessary to improve the mesh to generate a good simulation. To do that some dimensionless number are used, Figure 4.13 shows the computational domain and the grid structure for the cavity. The following figure and table are respectively a

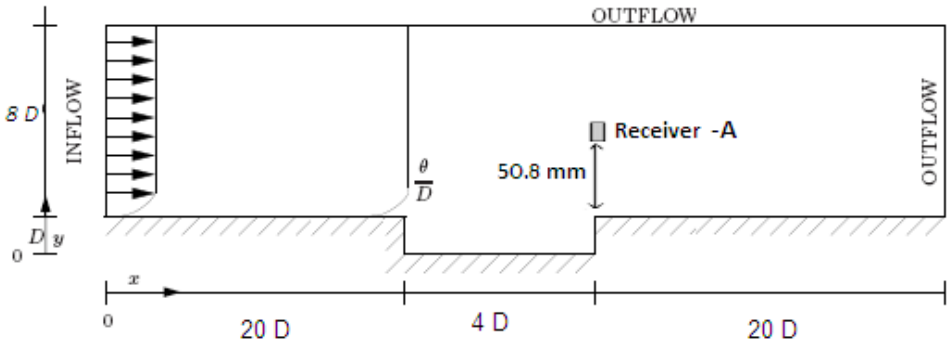

Figure 4.12: Schematic diagram of the computational domain

Total length of the domain	558.8 mm
Height of the domain	101.6 mm
Cavity length L	50.8 mm
Cavity depth D	12.7 mm
Aspect ratio of the cavity $\frac{L}{D}$	4

Table 4.1: Details of the Geometry

scaled sketch of the cavity section and sub-divided into blocks with labeled edges and table of the meshing parameters associated to the different edges.

While running a 2-D simulation OpenFOAM does not support strictly 2-D cases and the depth of the domain size is therefore specified as 1. This "additional" volume created by a front and back plane will later on be defined as empty and yield a 2-D domain.

For applications with complex, inhomogeneous flows and flow-induced noise radiation, the most promising and commonly used numerical technique is to adopt a hybrid approach. In such an approach, the sound-generation and sound propagation processes are considered separately. The general idea is to alternate as fast as possible between a "noise generation" fine mesh criteria to a "noise propagation" coarser one. This is achieved by making sure that the highly turbulent zones are meshed with the fine criteria.

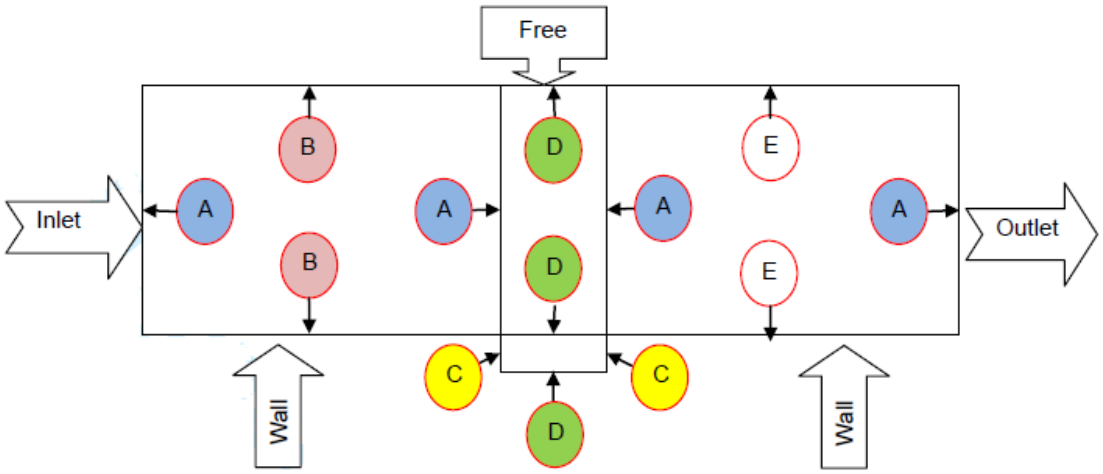

Edges	A	B	C	D	E
Nodes	101	254	150	150	88
grid size	72192				
Mesher Type	quadrilateral mesh				
y-plus	$y^+ = \frac{\sqrt{\frac{\tau_\omega}{\rho}}y}{\nu}$			y^+_{max}	117
				y^+_{mean}	0.2
Omega	$\Omega = \frac{NE}{ND} = \frac{Number\ of\ elements}{Number\ of\ nodes}$			0.99	
Courant-Friedrichs-Lewv (CFL)	$C = \frac{u_x \Delta t}{\Delta x} + \frac{u_y \Delta t}{\Delta y}$			C_{max}	0.59
				C_{mean}	0.09

Figure 4.13: Side View of the Meshing Domain Sub-divided Into Four Blocks with Labeled Edges

4.3.2 Large Eddy Simulations

The solver use traditional Large Eddy Simulations (LES) wall model in conjunction with an acoustic analogy, in order to predict the aeroacoustic behavior of cavity flow. The idea underlying LES is so called convergent evolution. Behavior of the large-scale eddies depends strongly on the forces acting on the flow and on initial and boundary conditions; they are flow-dependent. Small-scale eddies are generally in dependent from what is happening on the larger scales; they are flow-independent. Hence large eddies are directly resolved while small eddies are modeled. To perform the simulation with LES method in CFD are used the continuity and momentum equation, below are present the continuity and momentum equations without filtering.

$$\frac{\partial p}{\partial t} + \frac{\partial(\rho u_i)}{\partial x_i} = 0 \tag{4.7}$$

$$\frac{\partial}{\partial t}(\rho u_i) + \frac{\partial}{\partial x_j}(\rho u_i u_j) = -\frac{\partial p}{\partial x_i} + \frac{\partial}{\partial x_j}[\rho\nu(\frac{\partial u_i}{\partial x_j} + \frac{\partial u_j}{\partial x_i})] \tag{4.8}$$

Filtering operation is applied to continuity and momentum equations

$$\frac{\partial p}{\partial t} + \frac{\partial(\rho \bar{u}_i)}{\partial x_i} = 0 \tag{4.9}$$

$$\frac{\partial}{\partial t}(\rho \overline{u}_i) + \frac{\partial}{\partial x_j}(\rho \overline{u_i u_j}) = -\frac{\partial \overline{p}}{\partial x_i} + \frac{\partial}{\partial x_j}[\rho\nu(\frac{\partial \overline{u}_i}{\partial x_j} + \frac{\partial \overline{u}_j}{\partial x_i})] \tag{4.10}$$

To reduce the momentum filter equation are used the following considerations :

1. The product of filter velocities is $\overline{u_i u_j} = \overline{u}_i \overline{u}_j + \overline{u}_i^{'} \overline{u}_j^{'}$;
2. The subgrid stress tensor, which is the Reynolds stress tensor is $\tau_{ij}^{'} = \rho u_i^{'} u_j^{'} = \rho(\overline{u_i u_j} - \overline{u}_i \overline{u}_j)$;
3. The filtered strain tensor rate is $\overline{S}_{ij} = \frac{1}{2}(\frac{\partial \bar{u}_i}{x_j} + \frac{\partial \bar{u}_j}{\partial x_i})$;
4. The filtered viscous stress tensor is $\overline{\tau}_{ij} = 2\rho\nu\bar{S}_{ij}$.

The result of the reduction of the momentum filter equation is :

$$\frac{\partial}{\partial t}(\rho \overline{u}_i) + \frac{\partial}{\partial x_j}(\rho \overline{u_i u_j}) = -\frac{\partial \overline{p}}{\partial x_i} + \frac{\partial}{\partial x_j}[\rho\nu(\overline{\tau}_{ij} - \tau_{ij}^{'}) \tag{4.11}$$

Spectrum of turbulent eddies in the Navier-Stokes equations is filtered :

1. The filter is a function of grid size;
2. Eddies smaller than the grid size are removed and modeled by a subgrid scale (SGS) model;
3. Larger eddies are directly solved numerically by the filtered transient N-S equation.

Leonard (1974) proposes a model it as the application of a convolution filter to the exact solution. The filtered part $\bar{u}$ of the variable u is defined by the following convolution operator (denoted by the symbol * hereafter) :

$$\overline{u}(x,t) = \int_{-\infty}^{t} \int_{-\infty}^{+\infty} G(\overline{\Delta},\overline{\theta},|x-x^{'}|,t-t^{'})u(x^{'},t^{'})dx^{'}dt^{'} = G(\overline{\Delta},\overline{\theta},) * u(x,t) \tag{4.12}$$

where $G(\overline{\Delta},\overline{\theta},|x-x^{'}|,t-t^{'})$ is the kernel of the filter. The two arbitrary parameters $\overline{\Delta}$ and $\overline{\theta}$ are the cutoff length and the cutoff time, respectively. It can be proven that G must depend on the distance $|x-x^{'}|$ to preserve certain symmetries of the Navier-Stokes equations. The small-scale subgrid part $u^{'}$is then defined as :

$$u^{'}(x,t) = u(x,t) - \bar{u}(x,t) \tag{4.13}$$

Next it is generated a filtration to reduce them for Explicit LES and Implicit LES:

1. Explicit (i.e., associated with the application of a convolution filter to the DNS solution).

2. Implicit (i.e., imposed by numerical errors, the computational mesh, or modeling errors) or even a blending of these two possibilities. The numerical filter: the numerical error, which is not uniformly distributed over the resolved frequencies, can also be interpreted as a filter. When local numerical methods such as finite element, finite volume, or finite difference methods are used to solve the governing equations, the numerical error is observed to be an increasing function of the wave number. Consequently, the dynamics of the highest frequencies resolved on the computational grid are only poorly captured, and these scales can be considered as being filtered.(M. Hahn et al , 2005)[29],(Thornber et al, 2008)[68] and (Drikakis et al. ,2009)[15].

The subgrid stress tensor is expressed as: $\tau_{ij}^{'} = \rho(u_i\bar{u}_j - \overline{\bar{u}_i\bar{u}_j} + \tilde{\tau}_{ij}^{'})$, where the tensor $\tilde{\tau}_{ij}^{'}$ is considered equal to subbgrid dissipation scale action. High-resolution methods are most commonly associated with compressible flow solutions. Their introduction to incompressible flow solutions was most directly impacted by their use with a projection method by Bell, Colella, and Glaz (1989), as well as with the artificial compressibility method by Drikakis, Govatsos, and Papantonis (1988). (FERNANDO F. et al., 2007)[26].

One Equation Eddy Model Most one equation models are solving one equation for their own subgrid-scale quantity, which also based on the eddy-viscosity concept.

One such typical scale like kinetic energy k_{SGS}, is defined as the subtracting of kinetic energy and the resolved kinetic energy:

$$k_{SGS} = \overline{K} - k_{RES} = \frac{1}{2}\tau_{ij} \tag{4.14}$$

The transport equation for SGS turbulent energy can be derived by first subtracting the filtered equations of motion from their resolved parts to give a relation to the fluctuating component of velocity $u^{'}$. And then multiply the result by the sub-grid velocity vector to give the equation, which was first formulated by Yoshizawa [72] as:

$$\frac{\partial k_{SGS}}{\partial t} + \frac{\partial}{\partial x_j}(\overline{u}_i k_{SGS}) = \frac{\partial}{\partial x_j}[(\nu + \nu_{SGS})\frac{\partial k_{SGS}}{\partial x_j}] + 2\nu_{SGS}\overline{S}_{ij}\overline{S}_{ij} - \frac{1}{\overline{\Delta}}C_e k_{SGS}^{\frac{3}{2}} \tag{4.15}$$

$$\nu_{SGS} = C_k k_{SGS}^{\frac{1}{2}}\overline{\Delta} \tag{4.16}$$

The production term $2\nu_{SGS}\overline{S}_{ij}\overline{S}_{ij}$ in this equation is equivalent to the SGS dissipation in the equation for the resolved turbulent kinetic energy k_{RES}. Δ is taken to be the power average of the grid sizes in all directions, $\Delta = (\Delta_x\Delta_y\Delta_z)^{\frac{1}{3}}$. Default values of model coefficients C_e and C_k are given in OpenFoam as C_e = 1.048 and C_k = 0.094.

4.3.3 Initial and boundary conditions

Free stream variables for each length-to-depth ratio were set everywhere in the domain as the initial condition for the unsteady flow with $M = 0.3$ and $R_e = 3.2 \times 10^{-5}$. The results presented here were normalized on the following conditions: Air at 20^0C and 1 bar; Dynamic viscosity $\mu = 1.82 \times 10^{-5} Nsm^{-2}$, Density $\rho = 1.19 kgm^{-3}$. The boundary conditions are defined in the Table 4.2. Furthermore, time dependency is a crucial factor of this study due the unsteadiness of the flow field consisting of random and periodic pressure fluctuation occurring within the cavity. Each time step was set as 0.25×10^{-5} seconds with initial time equal to zero and a the maximum time duration was set as 49500 time steps, cumulating a simulation time of 0.4975 seconds.

Figure 4.14 shows the density of mesh resolution near the walls and in the cavity region. The boxed region which is highlighted at the upper left corner represents the high mesh density. It is the region where the shear layer and other important mechanisms begin for hydrodynamics and aeroacoustics.

The Virtual microphones positions are also depicted for visual inspection in the xy plane in Figure 4.15.

Boundary	Velocity	Pressure	nuSgs
Inlet	timeVaryingUniformFixedValue; M=0.3	zeroGradient	zeroGradient
outlet	zeroGradient	totalPressure	zeroGradient
cavity and bottom	Wall; No-Slip	zeroGradient	zeroGradient
Top	Free-Stream	zeroGradien	zeroGradient
front/back	empty	empty	empty

Table 4.2: Boundary conditions

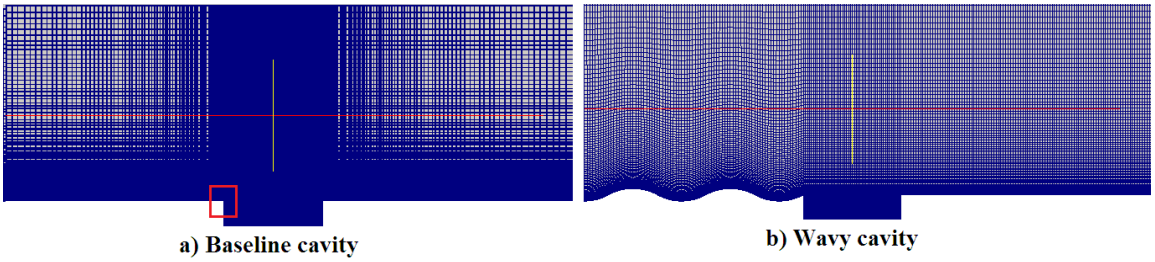

Figure 4.14: Mesh density: a) Baseline cavity b) Wavy cavity

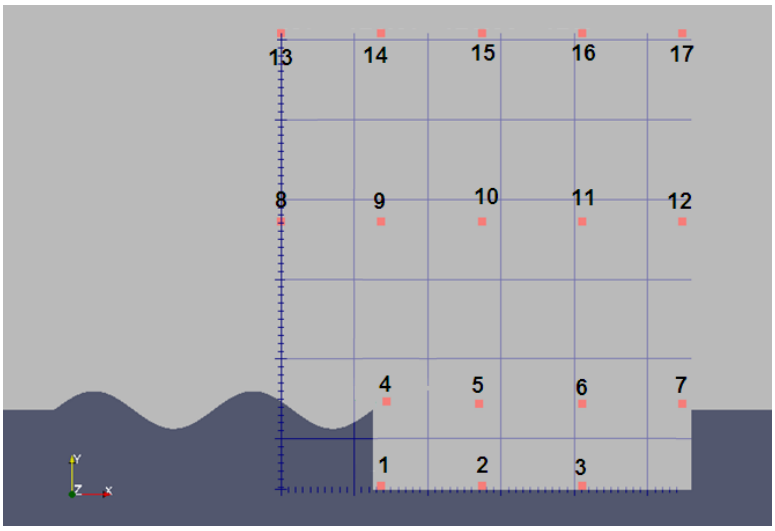

Figure 4.15: Microphone positions

4.4 Three Dimensional simulations

Figure 4.16 illustrates the schematic diagram of three dimensional computational domain adopted to simulate cavity flows for the fate case. The flat case mesh replicates the two-dimensional parameters detailed in section 4.3. The 3rd dimension mesh has been obtained using the consecutive extrusions by normal element. The flow is from

Edges	A	B	C	F	E	G	N
Nodes	101	254	150	150	88	25	25
Grid Size	4.289.400						
Mesher type	Quadrilateral mesh						

Table 4.3: Meshing Parameters

left to right hand side, the computational domain extends to 20D and 20D upstream and downstream of the cavity leading and trailing edges, respectively.

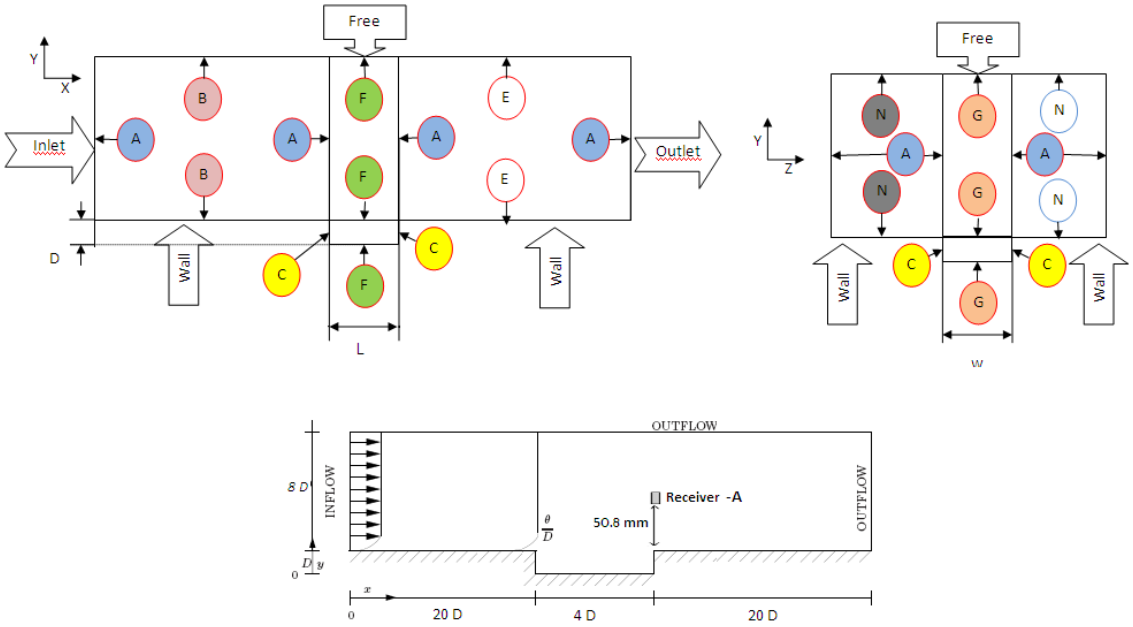

Figure 4.16: Side and front View of the Meshing Domain Sub-divided Into Four Blocks with Labelled Edges

The sound is the propagation of unsteady, small, pressure fluctuations it is of paramount importance that the mesh is fine enough to capture this phenomena. The table 4.3 detailed the meshing parameters associated to the different edges of the cavity section sub-divided into blocks.

The Computational mesh for the wavy case was generated to keep the same grid resolution defined for the baseline case. Figures (4.17, 4.18) show the Mesh topology for both baseline and wavy case respectively.

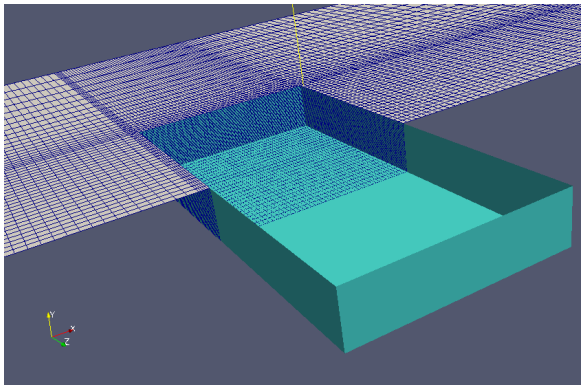

Figure 4.17: Baseline case mesh

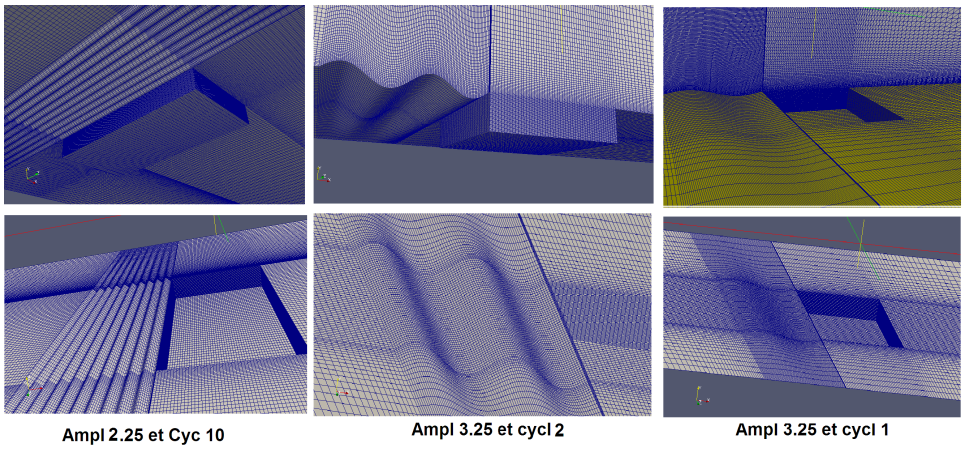

Figure 4.18: wavy case mesh

The microphone positions are also depicted for visual inspection in the xyz plane in Figure 4.19.

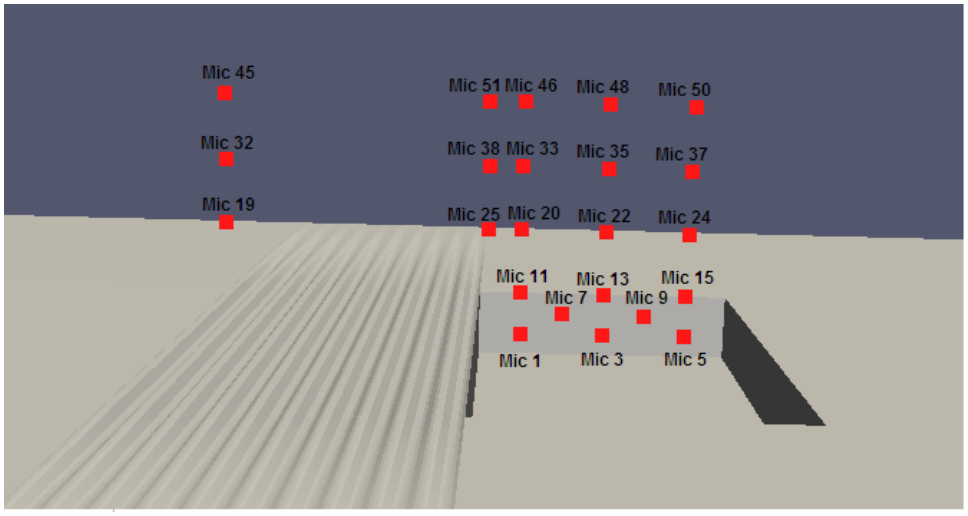

Figure 4.19: Microphone positions

4.4.1 Detached Eddy Simulation

Detached eddy simulation (DES) was originally formulated for the Spalart Allmaras model and is a hybrid approach which combines classical RANS and LES models. It bases on the idea to cover boundary layers by a RANS model and to switch to LES model in separated flow regions, which are typically characterised by larger turbulent structures. In other words, it allows a much coarser domain discretization than LES and therefore a reduced computational time, but still offers some of the advantages of an LES method in separated regions.

4.5 wake mode

Three-dimensionality has been shown to play a role in suppressing the wake mode. Large eddy simulations by Shieh and Morris [59] showed that two-dimensional cavities in wake mode return to shear-layer mode when three-dimensional disturbances are present in the incoming boundary layer. Similarly, recent work by Suponitsky et al. [66] showed that the development of a three-dimensional flow field, generated by the introduction of the random in flow disturbance into a two-dimensional cavity oscillating in wake mode, yielded the transition to the shear-layer mode, regardless of the amplitude and shape of the in flow disturbance.

CHAPTER 5

APPLICATION OF TRIPLE DECK THEORY TO SUBSONIC FLOW OVER A SURFACE WAVINESS

5.1 Introduction

The main physical ideas underlying Triple-Deck theory were laid down by Lighthill (1953) [41] treated interaction mathematically by perturbing a parallel flow, linearizing the Navier equations around it, and produced a coherent self-consistent theory of interaction that divides the region of interest into three parts: the inviscid flow outside the boundary layer, the displaced boundary layer in which the perturbations are governed by linearized compressible Euler equations, and an inner part close to the wall in which the perturbations are governed by incompressible boundary-layer equations.

Then, Gadd (1957) developed an approximate theory to extend the Lighthill's analysis to the nonlinear case. Stewartson (1969)[64], Stewartson and Williams (1969)[65] and Messiter (1970)[45] extended Lighthill's theory to nonlinear interactions and used the Gadd approximate to developed the Triple-Teck theory to overcome the singularities present in the boundary-layer solutions at the point of separation and at the edge of the flat plate. Hunt (1971)[30] and Smith (1973)[60], using order of magnitude arguments, investigated the structure of an incompressible flow at high Reynolds number past a hump on an otherwise smooth surface. In these cases The Triple-deck theory is able to accurately describe the interaction between the boundary layer flow and inviscid flow

outside the boundary layer. Triple-deck theory was extended to include unsteady flows by Schneider (1974)[58]. Here it was noted that the flow in the viscous lower deck was the most sensitive to unsteady perturbations to the flow and deduced the characteristic time within the lower deck. The flow in the main and upper decks was seen to remain quasi-steady. The asymptotic foundation of two-dimensional, steady-state Triple-Deck theory (for incompressible and compressible flows) is reviewed by Zeytounian (2002)[73]. Diesperov and Korolev (2003)[34] investigated the transonic flow past a small hump on a flat plate by solving the Triple-Deck equations with the interaction governed by the nonlinear $Kármán$ - Guderley equation in the upper deck. They were able to demonstrate the existence of closed pockets of supersonic regions in the outer flow in conjunction with separation in the lower deck. Recently, Lipatov and Koroteev have published a series of papers (see for instance Lipatov (2006)[42], Koroteev and Lipatov (2009[35], 2012[**?**], 2013[37])) in which micro-electro-mechanical-system (MEMS) devices are modelled as small flat-plate localised heating elements located in the boundary layer. The work of Mengaldo et al. (2015)[44] who looked at subsonic and transonic flows over roughness elements, suggests that Triple-Deck theory is able to correctly capture the main qualitative physics in practical aeronautical applications, although there are some differences in the quantitative results when compared to the full Navier-Stokes computations.

Our interest lies in trying to gain a better understanding, from a mathematical perspective, of how surface waviness can be used to change the flow properties. For aircraft, if we take the typical Reynolds numbers to be large and assume the characteristic size of a wing fuselage to be 4 m, then the size of the interaction region in the Triple-Deck theory is approximately 1 cm.

In the following analysis Section 1, we will examine a problem not with single hump, but with a multiple humps (wall waviness), periodic perturbation with the Triple-Deck scaling $y = hR^{-\frac{5}{8}}F(R^{-\frac{3}{8}}x)$ extending from a distance L_0 downstream from the leading edge. In Section 2, the appropriately scaled governing equations and boundary conditions are introduced, and the Triple-Deck structure described. The important lower-deck equations are derived in Section 3. In Section 4, the results of these nonlinear calculations are examined for increasing amplitude h, wavelength and incoming velocity.

5.2 Problem formulation

We consider laminar, incompressible, two-dimensional, steady flow past a flat plate on which there is a surface waviness has dimensions that are small compared with those of the boundary layer along the plate, described by the Navier-Stokes equations. The incoming flow is uniform and, therefore, irrotational. We assume that the perturbation produced by the boundary layer on the inviscid flow is of order ε for the velocity components and for the pressure. In addition, the small deformation of the wall induces a perturbation formally of the same order (Figure 5.1). We use an orthonormal axis system (x, y) with all the quantities are non-dimensionalised by using the free stream velocity U_∞ and the abscissa L_0 of the surface waviness location.

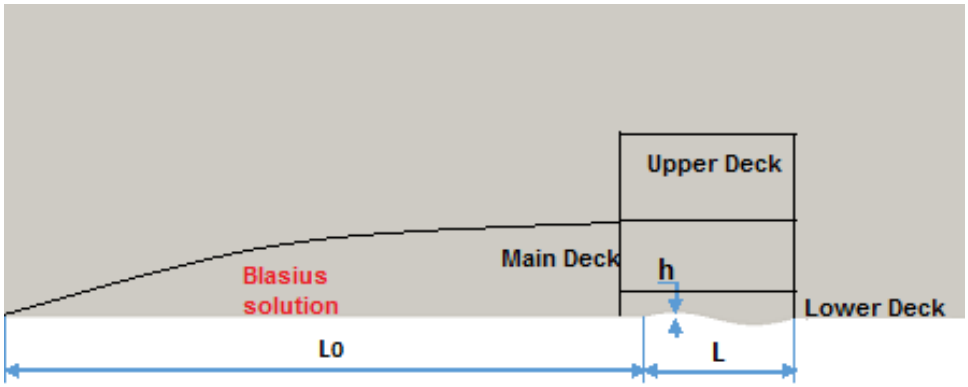

Figure 5.1: Model problem (flat plate deformed by a surface waviness)

We use the following dimensionless variables with the asterisk denoting dimensional quantities and ∞ free-stream values:

$$x = \frac{x^*}{L_0}, \qquad y = \frac{y^*}{L_0}, \qquad u = \frac{u^*}{U_\infty}, \qquad v = \frac{v^*}{U_\infty}, \qquad p = \frac{p^*}{\rho U_\infty^2}$$

The two dimensionless Navier-Stokes equations in terms of dimensionless variables are given by:

$$\begin{aligned} &\frac{\partial u}{\partial x} + \frac{\partial v}{\partial y} = 0 \\ &u\frac{\partial u}{\partial x} + v\frac{\partial u}{\partial y} = -\frac{\partial p}{\partial x} + \frac{1}{R}\frac{\partial^2 u}{\partial x^2} + \frac{1}{R}\frac{\partial^2 u}{\partial y^2} \\ &u\frac{\partial v}{\partial x} + v\frac{\partial v}{\partial y} = -\frac{\partial p}{\partial y} + \frac{1}{R}\frac{\partial^2 v}{\partial x^2} + \frac{1}{R}\frac{\partial^2 v}{\partial y^2} \end{aligned} \tag{5.1}$$

The Reynolds number Re defined by $Re = \rho_\infty U_\infty L_0/\mu_\infty$ is assumed to be large. Here ρ_∞, U_∞ and μ_∞ are the density, the streamwise velocity and the dynamic viscosity

coefficient, respectively, in the undisturbed flow above the surface where the surface waviness is located. The no-slip condition for the fluid at the body surface $u(x,0) = v(x,0) = 0$ and the condition of matching the solutions for the boundary layer and the outer inviscid flow field, which can be written as

$\lim_{y\to\infty} u(x,y) = \lim_{y\to 0} U(x,y) = U_e(x)$

$\frac{\partial p}{\partial x} |_{y=0} = p_e^{'}(x) = -U_e(x)U_e^{'}(x)$ The perturbations are caused by the rippled surface $y_0(x) = \varepsilon sin\alpha x$ (Figure 5.1) where ε is amplitude and $\alpha = 2\pi/L$ the reciprocal wave length. Consequently the flow properties may be expressed as the sum of a mean value and a small perturbation harmonic in αx The small parameter ε is defined by:

$$\varepsilon = \frac{1}{R^m}, \quad where \quad m \quad is \quad arbitrary \quad (m > 0) \tag{5.2}$$

In the inviscid flow region, the Navier-Stokes equations reduce to the Euler equations. In this region, the flow velocity components and the pressure are expanded as:

$$u = u_1(x,y) + ..., \quad v = v_1(x,y) + ..., \quad p = p_1(x,y) + ..., \tag{5.3}$$

and the Euler equation can be written as:

$$\begin{aligned} &\frac{\partial u_1}{\partial x} + \frac{\partial v_1}{\partial y} = 0 \\ &u_1\frac{\partial u_1}{\partial x} + v_1\frac{\partial u_1}{\partial y} = -\frac{\partial p_1}{\partial x} \\ &u_1\frac{\partial v_1}{\partial x} + v_1\frac{\partial v_1}{\partial y} = -\frac{\partial p_1}{\partial y} \end{aligned} \tag{5.4}$$

The no-slip conditions at the wall cannot be satisfied, it is necessary to introduce a boundary layer structure. The dependent variables are resolved into a mean undisturbed component denoted by the subscript 0 and a disturbed component which is identified by a tilde:

$$\begin{aligned} u^{'} &= u_0(Y) + \varepsilon\tilde{u}(x^{'},y^{'};\varepsilon)..., \\ v^{'} &= \varepsilon\tilde{v}(x^{'},y^{'};\varepsilon) + ..., \\ p^{'} &= p_0 + \varepsilon\tilde{p}(x^{'},y^{'};\varepsilon) + ..., \end{aligned} \tag{5.5}$$

where Y is the local variable $Y = \frac{y^{'}}{\varepsilon}$. All the scales and asymptotic structures are discussed in [12]. Then substituting these expressions into the incompressible Navier-Stokes equations, applying the aforementioned simplifying assumptions and retaining only first order perturbations, the boundary layer equations are given:

$$\begin{aligned} &\frac{\partial u^{'}}{\partial x^{'}}+\frac{\partial v^{'}}{\partial Y}=0 \\ &u^{'}\frac{\partial u^{'}}{\partial x^{'}}+v\frac{\partial u^{'}}{\partial Y}=-\frac{\partial p^{'}}{\partial x^{'}}+\frac{\partial^2 u^{'}}{\partial Y^2} \\ &0=-\frac{\partial p^{'}}{\partial Y} \end{aligned} \tag{5.6}$$

$$\begin{aligned} &at \quad Y=0 \quad \Rightarrow \quad u^{'}=0, \quad v^{'}=0 \\ &\lim_{Y\longrightarrow\infty} u^{'}(x^{'},Y)=u_1(x,0) \\ &v_1(x,0)=0 \\ &\lim_{Y\longrightarrow\infty} p^{'}(x^{'},Y)=p_1(x,0) \end{aligned} \tag{5.7}$$

The Prandtl's transposition theorem can be applied to Eqs. 5.6, 5.7 in order to make the longitudinal axis coincide with the body surface by defining new longitudinal and vertical independent variables and a new normal velocity component as:

$$(x^{'},y^{'})\longmapsto [x=x^{'} \quad ,y=y^{'}-F(x^{'})] \tag{5.8}$$

where $F(x^{'})$ is the equation of the surface waviness.
The following change on the velocity components is also introduced:

$$u=u^{'}, \quad v=v^{'}-\frac{dF}{dx^{'}}u^{'}, \quad p=p^{'} \tag{5.9}$$

Applying the chain rule:

$$\begin{aligned} &\frac{\partial p}{\partial x}=\frac{\partial p^{'}}{\partial x^{'}}\frac{\partial x^{'}}{\partial x}+\frac{\partial p^{'}}{\partial y^{'}}\frac{\partial y^{'}}{\partial x}=\frac{\partial p^{'}}{\partial x^{'}}-F^{'}(x)\frac{\partial p^{'}}{\partial y^{'}} \\ &\frac{\partial p}{\partial y}=\frac{\partial p^{'}}{\partial x^{'}}\frac{\partial x^{'}}{\partial y}+\frac{\partial p^{'}}{\partial y^{'}}\frac{\partial y^{'}}{\partial y}=\frac{\partial p^{'}}{\partial y^{'}} \end{aligned} \tag{5.10}$$

The Navier-Stokes equations become [12]:

- Continuity equation
  $\frac{\partial u}{\partial x}+\frac{\partial v}{\partial y}=0,$
- x-momentum equation
  $u\frac{\partial u}{\partial x}+v\frac{\partial u}{\partial y}=-\frac{\partial p}{\partial x}+\frac{\partial p}{\partial y}\frac{dF}{dx}+\varepsilon^m\frac{\partial^2 u}{\partial x^2}-2\varepsilon^m\frac{\partial^2 u}{\partial x\partial y}\frac{dF}{dx}+\varepsilon^m\frac{\partial^2 u}{\partial y^2}(\frac{dF}{dx})^2-\varepsilon^m\frac{\partial u}{\partial y}\frac{d^2F}{dx^2}+$
  $\varepsilon^m\frac{\partial^2 u}{\partial y^2},$

- y-momentum equation

$$u\frac{\partial v}{\partial x}+u^2\frac{d^2F}{dx^2}+v\frac{\partial v}{\partial y}+u\frac{dF}{dx}\frac{\partial u}{\partial x}+v\frac{\partial u}{\partial y}\frac{dF}{dx}=-\frac{\partial p}{\partial y}+2\varepsilon^m\frac{d^2F}{dx^2}\frac{\partial u}{\partial x}+\varepsilon^m\frac{\partial^2 u}{\partial y^2}(\frac{dF}{dx})^3-2\varepsilon^m\frac{\partial^2 v}{\partial x\partial y}(\frac{dF}{dx})+$$
$$\varepsilon^m u\frac{d^3F}{dx^3}-\varepsilon^m\frac{\partial v}{\partial y}\frac{d^2F}{dx^2}-2\varepsilon^m\frac{\partial^2 u}{\partial x\partial y}(\frac{dF}{dx})^2+\varepsilon^m\frac{\partial^2 u}{\partial y^2}\frac{dF}{dx}+\varepsilon^m\frac{dF}{dx}\frac{\partial^2 u}{\partial x^2}+\varepsilon^m\frac{\partial^2 v}{\partial y^2}(\frac{dF}{dx})^2-$$
$$3\varepsilon^m\frac{d^2F}{dx^2}\frac{\partial u}{\partial y}\frac{dF}{dx}+\varepsilon^m\frac{\partial^2 v}{\partial x^2}+\varepsilon^m\frac{\partial^2 v}{\partial y^2}$$

The streamwise extent of the perturbation is ε^α so that the variable adapted to the study is

$$X=\frac{x}{\varepsilon^\alpha},\qquad Y=\frac{y}{\varepsilon^{m/2}}$$

The Blasius solution U_b, can then be approximated using a Taylor expansion around $x\simeq 0$:

$U_{b(x\simeq 0,Y)}=U_0(Y)+O(\varepsilon^\alpha)$ Where $U_0(Y)=U_b(0,Y)$.

The boundary layer perturbations are sought in the general form

$u=U_0(Y)+\mu\overline{U}(X,Y)\quad \mu\ll 1$ where the gauge μ is unknown a priori.

The scalings of this problem require a division of the vertical structure into a Triple-Deck regime as shown in Figure 5.2: a viscous sublayer ('Lower Deck') and an inviscid main part of the boundary layer ('Main Deck'), where the third tier is an inviscid potential flow ('Upper Deck') outside of the boundary layer. The Triple-Deck structure establishes a link between the unperturbed upstream flow and the downstream flow.

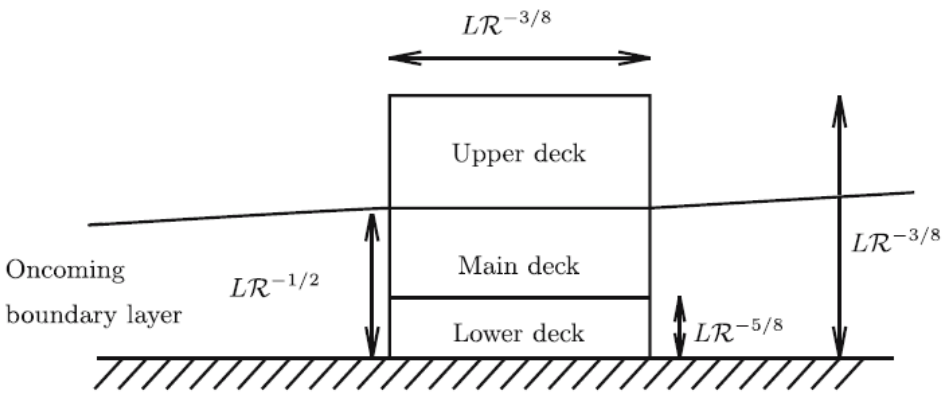

Figure 5.2: Triple deck structure [12]

The streamwise and transverse length scales of the perturbed region are $LR^{\frac{-3}{8}}$. Inside the perturbed region, there are three decks.

- Lower Deck: The "Lower Deck" or viscous sublayer: the thickness of the lower deck is $LR^{\frac{-5}{8}}$, is comprised of the stream filaments immediately adjacent to the wall. Even a small variation of pressure along the wall may cause significant deceleration/acceleration of fluid particles there. As a result the flow filaments change their thickness leading to a deformation of streamlines. This process is termed the displacement effect of the boundary layer. The perturbations in this lower layer called are transmitted through the "Main Deck".
- Main Deck: The basic boundary layer, which is now the "Main Deck". The main part of the boundary layer, the middle tier of the interactive structure, represents a continuation of the conventional boundary layer developing along the plate. Its thickness is estimated as $LR^{\frac{-1}{8}}$. The flow in this tier is significantly less sensitive to the pressure variations. It does not produce any noticeable contribution to the displacement effect of the boundary layer, which means that all the streamlines in the middle tier are parallel to each other and carry the deformation produced by the displacement effect of the viscous sublayer.
- Upper Deck: The upper tier is situated in the potential flow region outside the boundary layer. It serves to convert the perturbations in the form of the streamlines into perturbations of pressure. These are then transmitted through the main part of the boundary layer back to the "Lower Deck", enhancing the process of fluid deceleration. This process is self-sustained, and it drives the boundary layer towards the separation.

As in all Triple-Deck problems, it reduces to solving the lower-deck equations. These, in turn, will furnish solutions for the main and upper decks.

We consider the surface waviness on the wall $y = 0$ of equation $y = \varepsilon^{\beta} f(\frac{x}{\varepsilon^{\alpha}})$. To determine the layer thicknesses and the gauge functions, depending on the values of the two parameters α, β. Four zones have been identified Figure 5.3 shows the limits of these four zones depending on the hump's height (h) and horizontal size (L). Two conditions are imposed : $\beta > \frac{m}{2}$, $\beta > \alpha$. Physically, this means that the protuberance height is less than the incident boundary layer thickness, and less than

its dimensions in the x direction.
In the map (α, β), four significant zones are defined [52]:

- Zones 1 and 2 have linear equations in the lower deck;
- Zones 3 and 4, corresponding to higher protuberances, have non-linear ones;
- Zones 1 and 3 the lower-deck equations are solved in direct mode with prescribed pressure;
- Zones 2 and 4, they are solved in inverse mode with the displacement thickness is prescribed and the pressure is deduced from the resulting solution.

They are delimited by different straight lines whose meaning is given below (Fig. 5.3).

- D1: $\beta = \alpha$. The height of the surface waviness must be smaller than its length.
- $\beta = m/2$. For $\beta > m/2$, the hump height is smaller than the thickness of the oncoming boundary layer.
- $\beta = m/2$. For $\beta > m/2$, the hump height is smaller than the thickness of the oncoming boundary layer.
- $\alpha = 3m/8$. This line defines the boundary between zone 1 and zone 2 wh ch differ by the mode of resolution. The direct mode applies in zone 1 and the inverse mode in zone 2.

- D5: $\beta = \alpha + m/2$. If $\beta > \alpha + m/2$, the perturbations are small with respect to the second order of the standard boundary layer theory. For example, the first order of the pressure in zone 1 is $\varepsilon^{\beta-\alpha}$ whereas the second order in the boundary layer is $\varepsilon^{m/2}$.

- $\alpha = 3m/10$. This boundary is given by the study of second order terms and defines the hierarchy between U_1^* and $\bar{U}_2$. Along the straight line D6, the point of abscissa $\alpha = 3m/10$ corresponds to $\beta = m/2$ which is the limit of the hump height.

- D6: $\beta = 5\alpha/3$. This line defines the boundary for the linearity of lower deck equations between zones 1 and 3. In zone 1, the lower deck equations are linear whereas in zone 3, they are non linear.

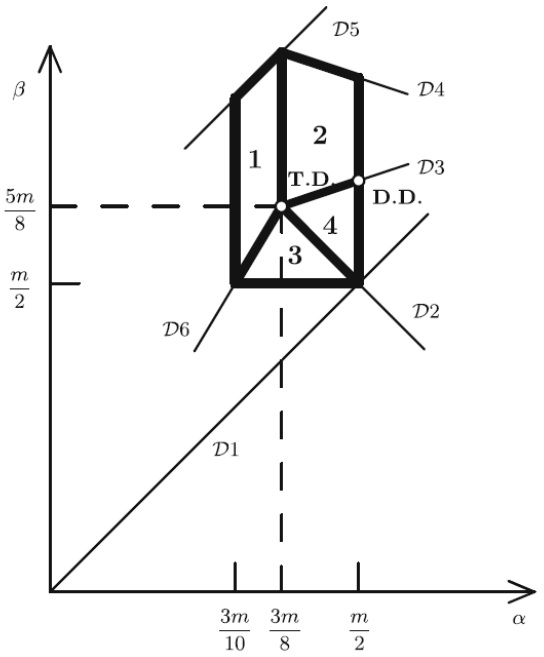

Figure 5.3: Delimitation of different zones around the Triple-Deck; T.D.: Triple-Deck, D.D.: double deck [12],[11]

- D3: $\beta = \alpha/3 + m/2$. This line defines the boundary for the linearity of lower deck equations between zones 2 and 4. In zone 2, the lower deck equations are linear whereas in zone 4, they are non linear.

- $\alpha = m/2$. The upper deck dimension is of order ε^{α}. The line $4\alpha = m/2$ defines the minimum of the streamwise hump extent which is supposed to be larger than the thickness of the oncoming boundary layer; this condition implies the existence of an upper deck thicker than Blasius boundary layer which is of order $\varepsilon^{m/2}$.

- D4: $\beta = m - \alpha/3$. If $\beta > m - \alpha/3$ the perturbations are large compared to the second order of the standard boundary layer theory. For example, the first order of the pressure in zone 2 is $\varepsilon^{\beta+\alpha/3-m/2}$ whereas the second order of the standard boundary layer is $\varepsilon^{m/2}$.

- D2: $\beta = -\alpha + m$. This line defines the boundary of zones 3 and 4 which differ by the mode of resolution of equations: direct mode in zone 3 and inverse mode in

zone 4.

Zone 1

$$Y^* = \frac{y}{\varepsilon^{\alpha}}\ , \quad \bar{Y} = Y = \frac{y}{\varepsilon^{m/2}}, \quad \tilde{Y} = \frac{y}{\varepsilon^{\alpha/3+m/2}}$$

Upper deck

- $u = 1 + \varepsilon^{\beta-\alpha} U_1^* + ...,$
- $v = \varepsilon^{\beta-\alpha} V_1^* + ...,$
- $p = \varepsilon^{\beta-\alpha} P_1^* + ...,$

- $\dfrac{\partial U_1^*}{\partial X} + \dfrac{\partial V_1^*}{\partial Y^*} = 0,$
- $\dfrac{\partial U_1^*}{\partial X} = -\dfrac{\partial P_1^*}{\partial X},$
- $\dfrac{\partial V_1^*}{\partial X} + \dfrac{d^2 f}{dX^2} = -\dfrac{\partial P_1^*}{\partial Y^*}.$

Main deck

- $u = U_0(Y) + \varepsilon^{\beta-4\alpha/3}\overline{U}_1 + \varepsilon^{\beta-8\alpha/3}\overline{U}_2 + ...,$
- $v = \varepsilon^{\beta-7\alpha/3+m/2}\overline{V}_1 + ...,$
- $p = \varepsilon^{\beta-\alpha}\overline{P}_1,$

- $\dfrac{\partial \overline{U}_1}{\partial X} + \dfrac{\partial \overline{V}_1}{\partial \overline{Y}} = 0,$
- $U_0 \dfrac{\partial \overline{U}_1}{\partial X} + \overline{V}_1 \dfrac{dU_0}{d\overline{Y}} = 0,$
- $\dfrac{\partial \overline{P}_1}{\partial \overline{Y}} = 0.$

Lower deck

- $u = \varepsilon^{\beta/3}\lambda\tilde{Y} + \varepsilon^{\beta-4\alpha/3}\tilde{U}_1 + ...,$
- $v = \varepsilon^{m/2-2\alpha+\beta}\tilde{V}_1 + ...,$
- $p = \varepsilon^{\beta-\alpha}\tilde{P}_1 + ...,$

- $\dfrac{\partial \tilde{U}_1}{\partial X} + \dfrac{\partial \tilde{V}_1}{\partial \tilde{Y}} = 0,$
- $\lambda\tilde{Y}\dfrac{\partial \tilde{U}_1}{\partial X} + \lambda\tilde{V}_1 = -\dfrac{\partial \tilde{P}_1}{\partial X} + \dfrac{\partial^2 \tilde{U}_1}{\partial \tilde{Y}^2}$
- $\dfrac{\partial \tilde{P}_1}{\partial \tilde{Y}} = 0.$

Zone 2

$$Y^* = \frac{y}{\varepsilon^{\alpha}}, \quad \bar{Y} = Y = \frac{y}{\varepsilon^{m/2}}, \quad \tilde{Y} = \frac{y}{\varepsilon^{\alpha/3+m/2}}$$

Upper deck

- $u = 1 + \varepsilon^{\beta+\alpha/3-m/2} U_2^* + ...,$
- $v = -\varepsilon^{\beta-\alpha}\dfrac{df}{dX} + \varepsilon^{\beta+\alpha/3-m/2} V_2^* + ...,$
- $p = \varepsilon^{\beta+\alpha/3-m/2} P_2^* + ...,$

- $\dfrac{\partial U_2^*}{\partial X} + \dfrac{\partial V_2^*}{\partial Y^*} = 0,$
- $\dfrac{\partial U_2^*}{\partial X} = -\dfrac{\partial P_2^*}{\partial X},$
- $\dfrac{\partial V_2^*}{\partial X} = -\dfrac{\partial P_2^*}{\partial Y^*}.$

Main deck

- $u = U_0(Y) + \varepsilon^{\beta-m/2} f(X)\dfrac{dU_0}{dY} + \varepsilon^{\beta+4\alpha/3-m}\overline{U}_2 + ...,$
- $v = -\varepsilon^{\beta-\alpha}\dfrac{df}{dX}U_0(Y) + \varepsilon^{\beta+\alpha/3-m/2}\overline{V}_2 + ...,$
- $p = \varepsilon^{\beta+\alpha/3-m/2}\overline{P}_2 + ...,$

- $\dfrac{\partial \overline{U}_2}{\partial X} + \dfrac{\partial \overline{V}_2}{\partial \overline{Y}} = 0,$
- $U_0\dfrac{\partial \overline{U}_2}{\partial X} + \overline{V}_2\dfrac{dU_0}{d\overline{Y}} = 0,$
- $\dfrac{\partial \overline{P}_2}{\partial \overline{Y}} = 0.$

Lower deck

- $u = \varepsilon^{\alpha/3}\lambda\widetilde{Y} + \varepsilon^{\beta-m/2}\widetilde{U}_1 + ...,$
- $v = \varepsilon^{\beta-2\alpha/3}\widetilde{V}_1 + ...,$
- $p = \varepsilon^{\beta+\alpha/3-m/2}\widetilde{P}_1 + ...,$

- $\dfrac{\partial \widetilde{U}_1}{\partial X} + \dfrac{\partial \widetilde{V}_1}{\partial \widetilde{Y}} = 0,$
- $\lambda\widetilde{Y}\dfrac{\partial \widetilde{U}_1}{\partial X} + \lambda\widetilde{V}_1 = -\dfrac{\partial \widetilde{P}_1}{\partial X} + \dfrac{\partial^2 \widetilde{U}_1}{\partial \widetilde{Y}^2}$
- $\dfrac{\partial \widetilde{P}_1}{\partial \widetilde{Y}} = 0.$

Zone 3

$$Y^* = \frac{y}{\varepsilon^{\alpha}}, \quad \bar{Y} = Y = \frac{y}{\varepsilon^{m/2}}, \quad \tilde{Y} = \frac{y}{\varepsilon^{(3\alpha-\beta+2m)/4}}$$

Upper deck

- $u = 1 + \varepsilon^{\beta-\alpha}U_1^* + ...,$
- $v = \varepsilon^{\beta-\alpha}V_1^* + ...,$
- $p = \varepsilon^{\beta-\alpha}P_1^* + ...,$

- $\dfrac{\partial U_1^*}{\partial X} + \dfrac{\partial V_1^*}{\partial Y^*} = 0,$
- $\dfrac{\partial U_1^*}{\partial X} = -\dfrac{\partial P_1^*}{\partial X},$
- $\dfrac{\partial V_1^*}{\partial X} + \dfrac{d^2 f}{dX^2} = -\dfrac{\partial P_1^*}{\partial Y^*}.$

Main deck

- $u = U_0 + \varepsilon^{(\beta-\alpha)/2}\overline{U}_1 + ...,$
- $v = \varepsilon^{(\beta-3\alpha+m)/2}\overline{V}_1 + ...,$
- $p = \varepsilon^{\beta-\alpha}\overline{P}_1,$

- $\dfrac{\partial \overline{U}_1}{\partial X} + \dfrac{\partial \overline{V}_1}{\partial \overline{Y}} = 0,$
- $U_0\dfrac{\partial \overline{U}_1}{\partial X} + \overline{V}_1\dfrac{dU_0}{d\overline{Y}} = 0,$
- $\dfrac{\partial \overline{P}_1}{\partial \overline{Y}} = 0.$

Lower deck

- $u = \varepsilon^{(\beta-\alpha)/2}\widetilde{U}_1 + \varepsilon^{(3\alpha-\beta)/4}\lambda\widetilde{Y} + ...,$
- $v = \varepsilon^{(\beta-3\alpha+2m)/4}\widetilde{V}_1 + ...,$
- $p = \varepsilon^{\beta-\alpha}\widetilde{P}_1 + ...,$

- $\dfrac{\partial \widetilde{U}_1}{\partial X} + \dfrac{\partial \widetilde{V}_1}{\partial \widetilde{Y}} = 0,$
- $\widetilde{U}_1\dfrac{\partial \widetilde{U}_1}{\partial X} + \widetilde{V}_1\dfrac{\partial \widetilde{U}_1}{\partial \widetilde{Y}} = -\dfrac{\partial \widetilde{P}_1}{\partial X} + \dfrac{\partial^2 \widetilde{U}_1}{\partial \widetilde{Y}^2}$
- $\dfrac{\partial \widetilde{P}_1}{\partial \widetilde{Y}} = 0.$

Zone 4

$$Y^* = \frac{y}{\varepsilon^{\alpha}}, \quad \bar{Y} = Y = \frac{y}{\varepsilon^{m/2}}, \quad \tilde{Y} = \frac{y}{\varepsilon^{(2\alpha-2\beta+3m)/4}}$$

Upper deck

- $u = 1 + \varepsilon^{2\beta-m} U_2^* + ...,$
- $v = -\varepsilon^{\beta-\alpha}\frac{df}{dX} + \varepsilon^{2\beta-m} V_2^* + ...,$
- $p = \varepsilon^{2\beta-m} P_2^* + ...,$

- $\frac{\partial U_2^*}{\partial X} + \frac{\partial V_2^*}{\partial Y^*} = 0,$
- $\frac{\partial U_2^*}{\partial X} = -\frac{\partial P_2^*}{\partial X},$
- $\frac{\partial V_2^*}{\partial X} = -\frac{\partial P_2^*}{\partial Y^*}.$

Main deck

- $u = U_0 + \varepsilon^{\beta-m/2} f(X)\frac{dU_0}{d\overline{Y}} + \varepsilon^{2\beta+\alpha-3m/2}\overline{U}_2 ...,,$
- $v = -\varepsilon^{\beta-\alpha}\frac{df}{dX} U_0 + \varepsilon^{2\beta-m}\overline{V}_2 + ...,$
- $p = \varepsilon^{2\beta-m}\overline{P}_2.$

- $\frac{\partial \overline{U}_2}{\partial X} + \frac{\partial \overline{V}_2}{\partial \overline{Y}} = 0,$
- $U_0\frac{\partial \overline{U}_2}{\partial X} + \overline{V}_2\frac{dU_0}{d\overline{Y}} = 0,$
- $\frac{\partial \overline{P}_2}{\partial \overline{Y}} = 0.$

Lower deck

- $u = \varepsilon^{\beta-\alpha/2}\widetilde{U}_1 + \varepsilon^{(2\alpha-2\beta+m)/4}\lambda\widetilde{Y} + ...,$
- $v = \varepsilon^{(2\beta-2\alpha+2m)/4}\widetilde{V}_1 + ...,$
- $p = \varepsilon^{2\beta-m}\widetilde{P}_1 + ...,$

- $\frac{\partial \widetilde{U}_1}{\partial X} + \frac{\partial \widetilde{V}_1}{\partial \widetilde{Y}} = 0,$
- $\widetilde{U}_1\frac{\partial \widetilde{U}_1}{\partial X} + \widetilde{V}_1\frac{\partial \widetilde{U}_1}{\partial \widetilde{Y}} = -\frac{\partial \widetilde{P}_1}{\partial X} + \frac{\partial^2 \widetilde{U}_1}{\partial \widetilde{Y}^2}.$
- $\frac{\partial \widetilde{P}_1}{\partial \widetilde{Y}} = 0.$

5.3 Methodology of analytical solution

In this work, the structure of the flow is studied along the line $\beta = -\alpha + m$ (D2), with $3m/8 < \alpha < m/2$, (Figure 5.3), corresponding to the model delimited by zone number 3:

$$Y^* = \frac{y}{\varepsilon^{\alpha}} \quad \bar{Y} = Y = \frac{y}{\varepsilon^{m/2}} \quad \tilde{Y} = \frac{y}{\varepsilon^{(4\alpha+m)/4}}$$

Upper deck	• $u = 1 + \varepsilon^{m-2\alpha} U_1^* + ...,$ • $v = \varepsilon^{m-2\alpha} V_1^* + ...,$ • $p = \varepsilon^{m\alpha-2\alpha} P_1^* + ...,$	• $\frac{\partial U_1^*}{\partial X} + \frac{\partial V_1^*}{\partial Y^*} = 0,$ • $\frac{\partial U_1^*}{\partial X} = -\frac{\partial P_1^*}{\partial X},$ • $\frac{\partial V_1^*}{\partial X} + \frac{d^2 f}{dX^2} = -\frac{\partial P_1^*}{\partial Y^*}.$
Main deck	• $u = U_0 + \varepsilon^{(m-2\alpha)/2} \overline{U}_1 + ...,$ • $v = \varepsilon^{m-2\alpha} \overline{V}_1 + ...,$ • $p = \varepsilon^{m-2\alpha} \overline{P}_1,$	• $\frac{\partial \overline{U}_1}{\partial X} + \frac{\partial \overline{V}_1}{\partial \overline{Y}} = 0,$ • $U_0 \frac{\partial \overline{U}_1}{\partial X} + \overline{V}_1 \frac{dU_0}{d\overline{Y}} = 0,$ • $\frac{\partial \overline{P}_1}{\partial \overline{Y}} = 0.$
Lower deck	• $u = \varepsilon^{(m-2\alpha)/2} \widetilde{U}_1 + \varepsilon^{(3\alpha-\beta)/4} \lambda \widetilde{Y} + ...,$ • $v = \varepsilon^{(3m-4\alpha)/4} \widetilde{V}_1 + ...,$ • $p = \varepsilon^{m-2\alpha} \widetilde{P}_1 + ...,$	• $\frac{\partial \widetilde{U}_1}{\partial X} + \frac{\partial \widetilde{V}_1}{\partial \widetilde{Y}} = 0,$ • $\widetilde{U}_1 \frac{\partial \widetilde{U}_1}{\partial X} + \widetilde{V}_1 \frac{\partial \widetilde{U}_1}{\partial \widetilde{Y}} = -\frac{\partial \widetilde{P}_1}{\partial X} + \frac{\partial^2 \widetilde{U}_1}{\partial \widetilde{Y}^2}$ • $\frac{\partial \widetilde{P}_1}{\partial \widetilde{Y}} = 0.$

5.3.1 Main Deck

In this deck, the first terms denote by $U_0(Y)$, the non perturbed velocity profile of the boundary layer at point $x = x_0$ and its slope at the wall, which does not depend on X, this means that, to the considered order, the basic velocity profile does not vary significantly in the perturbation domain. The upstream boundary condition results from matching to the Blasius solution. The non perturbed flow is described by the equation $2f_B''' + f_B f_B'' = 0$ with $U_0(x,Y) = f_B'(\eta)$ and $\eta = Y x^{\frac{-1}{2}}$.

The equation as follows are solved.

Using: $\frac{\partial \overline{U}_1}{\partial X} + \frac{\partial \overline{V}_1}{\partial \overline{Y}} = 0$ and $U_0 \frac{\partial \overline{U}_1}{\partial X} + \overline{V}_1 \frac{dU_0}{d\overline{Y}} = 0$

give:

$$-U_0 \frac{\partial \overline{V}_1}{\partial Y} + \overline{V}_1 \frac{dU_0}{d\overline{Y}} = 0 \tag{5.11}$$

Dividing both terms by U_0^2, the Equ. 5.11 become $-\frac{1}{U_0}\frac{\partial \overline{V}_1}{\partial Y} + \overline{V}_1 \frac{U_0^{'}}{U_0^2} = 0$ or equivalently $\frac{\partial}{\partial Y}(\frac{\overline{V}_1}{U_0}) = 0$

The ratio $\frac{\overline{V}_1}{U_0}$ is a function of X only, $\overline{V}_1$ become $-\frac{dA}{dX}U_0$ where $A(X)$ is an unknown displacement function.

The velocity-Blasius profile is given by: $U_0 \cong \lambda \overline{Y} + \frac{1}{2}\lambda_2 \overline{Y}^2$ as $\overline{Y} \to 0$. where the constant λ is defined by $\lambda = (\frac{dU_0}{dY})_{Y=0}$, is the local scaled skin friction of the oncoming boundary layer. Also the constant λ_2, is equal to the local externally produced pressure gradient $\frac{dp}{dx}$ driving the boundary layer in the absence of the surface waviness.

In the main deck, the solution is:

- $\overline{U}_1 = A(X)U_0^{'}(\overline{Y})$ with $U_0^{'}(\overline{Y}) = \frac{dU_0}{d\overline{Y}}$;
- $\overline{V}_1 = -A^{'}(X)U_0(\overline{Y})$ with $A^{'}(X) = \frac{dA}{dX}$;
- $P_1 = \overline{P}_1(X)$.

The appropriate form of the solution to the resulting equations is:

$$\begin{aligned} u &= U_0 + \varepsilon^{(m-2\alpha)/2} A(X) U_0^{'}(\overline{Y}) + ..., \\ v &= -\varepsilon^{m-2\alpha} A^{'}(X) U_0(\overline{Y}) + ..., \\ p &= \varepsilon^{m-2\alpha} \overline{P}_1. \end{aligned} \tag{5.12}$$

Where the displacement function A and P are unknown of the problem function of X. $A(X)$ can be interpreted as the velocity slip at the base of the main deck corresponding to the inviscid perturbation of the upstream Blasius solution by the induced pressure gradient. Another useful interpretation of $A(X)$ can be seen by noting that to second order the stream wise velocity in the main deck can be written in the form $U_0(y + \varepsilon A)$, where $U_0(y)$ is the Blasius solution and y the main-deck coordinate. Thus, can be regarded as a displacement thickness. By continuity, the transverse velocity at the top of the main deck is $-\varepsilon^2 A^{'}(X)$, which must match the potential flow at the base of the upper deck [31].

5.3.2 Lower Deck

The initial conditions are given by:

- $X \to -\infty$ is satisfied provided $A(-\infty) = 0$.
- On the surface waviness $Y = f(X)$ no-slip conditions $\widetilde{U}_1 = 0, \quad \widetilde{V}_1 = 0, \quad \dfrac{\partial \widetilde{U}_1}{\partial \widetilde{Y}} = 0$
- $\lim\limits_{\widetilde{Y}\to\infty} (\widetilde{U}_1 - \lambda \widetilde{Y}) = \lambda(A + f), \quad$ or $\quad \widetilde{U}_1 \to \lambda(\widetilde{Y} + A + f), \quad$ as $\quad \widetilde{Y} \to \infty.$

The conditions which relate the displacement thickness with the longitudinal vilocity are supplied with the interaction condition, which, in turn, relates the displacement thickness with th pressure and thus expresses the interaction of the viscous sublayer with the outer inviscid flow [36].

5.3.3 Upper Deck

The first term in the upper deck is 1, the value of the first approximation for the inviscid flow outside the boundary layer. from matching the solutions between the upper layer (as $Y^* \to 0$) and main layer (as $\overline{Y} \to \infty$):

$$
\begin{aligned}
&a) \quad Y^* \to 0: \quad U_0 \to 1 \quad U_1^* = 0;\\
&b) \quad V_1^* = -\frac{\partial f}{\partial X};\\
&c) \quad V_1^*(X,0) = \lim_{\overline{Y}\to\infty} \overline{V}_1(X,\overline{Y});\\
&d) \quad V_1^*(X,0) = -\frac{dA}{dX};\\
&e) \quad P_1^*(X,0) = -U_1^*(X,0);\\
&f) \quad P_1^*(X,0) = \lim_{\widetilde{Y}\to\infty} \widetilde{P}_1(X,\widetilde{Y}).
\end{aligned}
\tag{5.13}
$$

The Fourier transform $\hat{G}(\alpha, Y)$ of a function $g(X,Y)$ and the inversion integral are defined by the following formulas:

- $\widehat{G}(\alpha, Y^*) = \int\limits_{-\infty}^{\infty} g(X,Y^*) e^{-2i\pi X\alpha} dX,$
- $g(X,Y^*) = \int\limits_{-\infty}^{\infty} \widehat{G}(\alpha,Y^*) e^{2i\pi X\alpha} d\alpha,$

- $\widehat{\frac{\partial g}{\partial X}} = 2i\pi\alpha\widehat{G}.$

The equation for $\widehat{V}_1^*$ is deduced

$$-4\pi^2\alpha^2\widehat{V}_1^* + \frac{\partial^2\widehat{V}_1^*}{\partial Y^{*2}} = 2i\pi\alpha\frac{d^2\widehat{f}}{dX^2} \tag{5.14}$$

The solution of homogeneous linear equations $-4\pi^2\alpha^2\widehat{V}_1^* + \frac{\partial^2\widehat{V}_1^*}{\partial Y^{*2}} = 0$ are given by:

$$\widehat{V}_1^* = K_1 e^{2\pi\alpha Y_1^*} + K_2 e^{-2\pi\alpha Y_1^*} \tag{5.15}$$

Let $\widehat{V}_0^*(\alpha)$ be the Fourier transform of the velocity component V_1^* at $Y_1^* = 0$. In order that the velocity component V_1^* vanish as $Y_1^* \to \infty$, the solution writes:

- $\alpha \le 0 \quad : \quad \widehat{V}_1^* = \widehat{V}_0^* e^{2\pi\alpha Y_1^*}$ or $\widehat{V}_1^* = \widehat{V}_0^* e^{-2\pi|\alpha|Y_1^*}$
- $\alpha \ge 0 \quad : \quad \widehat{V}_1^* = \widehat{V}_0^* e^{-2\pi\alpha Y_1^*}$

and we obtain:

$$\widehat{U}_1^* = -isgn(\alpha)\widehat{V}_0^* e^{-2\pi|\alpha|Y_1^*} \tag{5.16}$$

The Method of Variation of Parameters:

$V_p = G_1(K_1 e^{2\pi\alpha Y_1^*}) + G_2(K_2 e^{-2\pi\alpha Y_1^*})$

Differentiating this equation

$V_p' = (G_1'(K_1 e^{2\pi\alpha Y_1^*}) + G_2'(K_2 e^{-2\pi\alpha Y_1^*})) + (G_1(K_1 e^{2\pi\alpha Y_1^*})' + G_2(K_2 e^{-2\pi\alpha Y_1^*})')$

Let's impose the condition that

- $G_1'(K_1 e^{2\pi\alpha Y_1^*}) + G_2'(K_2 e^{-2\pi\alpha Y_1^*}) = 0$

and we obtain:

- $V_p'' = G_1'(K_1 e^{2\pi\alpha Y_1^*})' + G_2'(K_2 e^{-2\pi\alpha Y_1^*})' + G_1(K_1 e^{2\pi\alpha Y_1^*})'' + G_2(K_2 e^{-2\pi\alpha Y_1^*})''$

Substituting in the differential

- $G_1^{'}(K_1 e^{2\pi\alpha Y_1^*})^{'} + G_2^{'}(K_2 e^{-2\pi\alpha Y_1^*})^{'} = 2i\pi\alpha \dfrac{d^2\widehat{f}}{dX^2}$

After solving the system of two equations in the unknown functions $G_1^{'}$ and $G_2^{'}$, the variables G_1 and G_2 are given. The general solution of the nonhomogeneous differential equation can be written as:

$$V_1^* = V_{1p}^* + V_{1c}^* \tag{5.17}$$

Where V_{1p}^* ia a solution particular and V_{1c}^* is called the complementary solution. To return to physical space, it is required to know the following formulas:

- $-isgn(\alpha)e^{-2\pi|\alpha|Y_1^*} = \int_{-\infty}^{\infty} \dfrac{X}{X^2 + Y_1^{*2}} e^{-2i\pi\alpha X} dX,$
- $\pi e^{-2\pi|\alpha|Y_1^*} = \int_{-\infty}^{\infty} \dfrac{Y_1^*}{X^2 + Y_1^{*2}} e^{-2i\pi\alpha X} dX.$

For $Y_1^* \neq 0$:

- $U_1^*(X, Y_1^*) = \dfrac{1}{\pi} \int_{-\infty}^{\infty} \dfrac{(V_1^*(\xi, 0) + \dfrac{\partial f}{\partial \xi})(X - \xi)}{(X - \xi)^2 + Y_1^{*2}} d\xi$
- $V_1^*(X, Y_1^*) + \dfrac{\partial f(X)}{\partial X} = \dfrac{1}{\pi} \int_{-\infty}^{\infty} \dfrac{U_1^* Y_1^*}{(X - \xi)^2 + Y_1^{*2}} d\xi$

In the above formulas, the velocity component U_1^* can be replaced by $-P_1^*$.

Along the ling $Y = 0$, the pressure and the velocity normal to the wall are related by Cauchy-Hilbert integral

$$P_1^*(X, 0) = -\frac{1}{\pi} \fint_{-\infty}^{\infty} \frac{(V_1^*(\xi, 0) + \dfrac{\partial f}{\partial \xi})}{X - \xi} d\xi \tag{5.18}$$

Using Equ.5.13-a) the Equ. 5.18 become:

$$P_1^*(X,0) = \frac{1}{\pi} \int_{-\infty}^{\infty} \frac{\frac{\partial}{\partial \xi}(A-f)}{X-\xi} d\xi \tag{5.19}$$

Moreover, as we have $\frac{\partial \overline{P}_1}{\partial \overline{Y}} = 0$ and $\frac{\partial \widetilde{P}_1}{\partial \widetilde{Y}} = 0$, we deduce $P_1^*(X,0) = \overline{P}_1(X) = \widetilde{P}_1(X)$.

The Triple-Deck displacement function, $A(X)$, is related to the air pressure through the Cauchy-Hilbert integral:

$$\widetilde{P}_1(X) = \frac{1}{\pi} \int_{-\infty}^{\infty} \frac{\frac{\partial}{\partial \xi}(A-f)}{X-\xi} d\xi \tag{5.20}$$

5.4 Numerical solution of Tripl Deck

Several techniques have been devised in recent years in an attempt to solve the above problem. Apart from the non-linearity of the governing equations, complications arise from the elliptic nature of the Hilbert integral pressure displacement relationship.

One relationship between the unknown pressure P and displacement A is obtained from the potential flow properties holding in the upper deck outside the boundary layer (Smith 1973; Stewartson 1974) [60], Equ. 5.20.

5.4.1 Discretisation of the interaction Law

In this subsection a brief method to discretise the Hilbert integral Equ.5.19 are presented. This method is presented by Kravtsova et al. [38]. The interaction equation can be written as:

$$\frac{\partial P}{\partial X}(X) = -\frac{1}{\pi} \int_{-\infty}^{\infty} \frac{A''(\xi) - f''(\xi)}{\xi - X} d\xi \tag{5.21}$$

We introduce a non-uniform mesh

$$(X_i, Y_m) \begin{cases} i = 1, ..., N \\ m = 1, ..., M \end{cases} \tag{5.22}$$

and denote the values of function $A(X)$ at points X_i by A_i. A_i are calculated in the 'inviscid pressure gradient', $\frac{\partial P}{\partial X}|_{inv}$. For the same A_i, we can calculate the 'viscous pressure gradient', $\frac{\partial P}{\partial X}|_v(X_i)$ based on Lower Deck equations. The task is to find function A_i that satisfies the following implicit set of equations:

$$G_j(A_i) = \frac{\partial P}{\partial X}|_{inv} - \frac{\partial P}{\partial X}|_v = 0, \quad j = 1,...,N \tag{5.23}$$

In order to solve these equations Newton Raphson linearization has been used, with an improved approximation written as $A_i + \delta A_i$. The correction function δA_i is determined by solving the matrix equation

$$G_j(A_i) + \frac{\partial G_j}{\partial A_i}\delta A_i = 0 \tag{5.24}$$

The general strategy is to suppose an approximation value for $A(\xi)$ to obtain an approximation value of $P(X)$ and that being done, an improved guess for A can be found from the Hilbert integral relating P and A. For additional details, the interested reader can also refer to Sychev et al. [67] and Korolev et al. [**?**].

5.4.2 Calculation of the Hilbert integral

The interaction below requires special manipulations due to the singularity of the integral.

$$\frac{\partial P}{\partial X}(X) = -\frac{1}{\pi}\int_{-\infty}^{\infty}\frac{A''(\xi)}{\xi - X}d\xi + \frac{1}{\pi}\int_{-\infty}^{\infty}\frac{f''(\xi)}{\xi - X}d\xi \tag{5.25}$$

The first integral Equ.5.25 is truncated at N and represented for each $X = X_i$ in the form:

$$\int_{X_1}^{X_N}\frac{A''(\xi)}{\xi - X_i}d\xi = \sum_{k=1}^{i-2}\int_{X_k}^{X_{k+1}}\frac{A''(\xi)}{\xi - X_i}d\xi + \int_{X_{i-1}}^{X_{i+1}}\frac{A''(\xi)}{\xi - X_i}d\xi + \sum_{k=i+1}^{N-1}\int_{X_k}^{X_{k+1}}\frac{A''(\xi)}{\xi - X_i}d\xi \tag{5.26}$$

using the Taylor expansion for $A(\xi)$ the Equ. 5.25 become:

$$\begin{aligned}
&\frac{\partial P}{\partial X}(X_i) = \beta(X_i) = A_i'''(X_{i+1} - X_{i-1})A_i'' \ln\frac{X_{i+1} - X_i}{X_i - X_{i-1}} \\
&+\sum_{k=1}^{i-2}\{A_{k+1}'''(X_{k+1} - X_k) + [A_{k+1}'' + (X_i - X_{k+1})A_{k+1}''']\ln\frac{X_i - X_{k+1}}{X_i - X_k}\} \\
&+\sum_{k=i+1}^{N-1}\{A_k'''(X_{k+1} - X_k) + [A_k'' + (X_i - X_k)A_k''']\ln\frac{X_{k+i} - X_i}{X_k - X_i}\} \\
&+\frac{1}{\pi}\int_{X_1}^{X_N}\frac{f''(\xi)}{\xi - X_i}d\xi
\end{aligned} \tag{5.27}$$

5.4.3 Solution of Lower Deck

The Lower Deck equations taking into account the asymptotic scales are:

$$\begin{aligned}
&\frac{\partial \widetilde{U}_1}{\partial X} + \frac{\partial \widetilde{V}_1}{\partial \widetilde{Y}} = 0 \\
&\widetilde{U}_1\frac{\partial \widetilde{U}_1}{\partial X} + \widetilde{V}_1\frac{\partial \widetilde{U}_1}{\partial \widetilde{Y}} = -\frac{\partial \widetilde{P}_1}{\partial X} + \frac{\partial^2 \widetilde{U}_1}{\widetilde{Y}^2} \\
&\frac{\partial \widetilde{P}_1}{\partial \widetilde{Y}} = 0
\end{aligned} \tag{5.28}$$

Here $\widetilde{U}_1$ and $\widetilde{V}_1$ are longitudinal and transverse components of velosity, $\widetilde{P}_1$ is the pressure which only depends on x and consequently is constant across the Desks, the pressure gradient is not a prescribed function as in the classical boundary-layer theory, but is determined through interaction with the displacement A, (Equ. 5.19).

The Lower Deck equations were calculated marching from position X_i to the next position X_{i+1}. For a set of the operator equations: $\phi_m = 0, \quad m = 1,...,M-1$. Provided that $\widetilde{U}_{j,m} \geq 0$, for $m = 2,...,M-2$ the momentum equation form become:

$$\begin{aligned}
\phi_m = &-\widetilde{U}_{i,m}\frac{C_1\widetilde{U}_{i-2,m} + C_2\widetilde{U}_{i-1,m} + C_3\widetilde{U}_{i,m}}{X_i - X_{i-2}} \\
&-\widetilde{V}_{i,m}\frac{d_1\widetilde{U}_{i,m-1} + d_2\widetilde{U}_{i,m} + d_3\widetilde{U}_{i,m+1}}{\widetilde{Y}_{m+1} - \widetilde{Y}_{m-1}} - \frac{d\widetilde{P}}{dX}|_i \\
&+\frac{b_1\widetilde{U}_{i,m-2} + b_2\widetilde{U}_{i,m-1} + b_3\widetilde{U}_{i,m} + b_4\widetilde{U}_{i,m+1}}{(\widetilde{Y}_{m+1} - \widetilde{Y}_{m-2})(\widetilde{Y}_{m+1} - \widetilde{Y}_m)}
\end{aligned} \tag{5.29}$$

Where $C_1 = \frac{X_{i-1} - X_i}{X_{i-2} - X_{i-1}}$ $C_2 = \frac{(X_i - X_{i-2})^2}{(X_{i-1} - X_i)(X_{i-2} - X_{i-1})}$ $C_3 = -(C_1 + C_2)$

$d_1 = -\frac{1}{d_3}$ $d_2 = -(d_1 + d_3)$ $d_3 = \frac{\widetilde{Y}_m - \widetilde{Y}_{m-1}}{\widetilde{Y}_{m+1} - \widetilde{Y}_m}$

$b_1 = -b_2\frac{\widetilde{Y}_{m-1} - \widetilde{Y}_m}{\widetilde{Y}_{m-2} - \widetilde{Y}_m} - b_4\frac{\widetilde{Y}_{m+1} - \widetilde{Y}_m}{\widetilde{Y}_{m-2} - \widetilde{Y}_m}$ $b_2 = -b_4\frac{(\widetilde{Y}_{m+1} - \widetilde{Y}_m)(\widetilde{Y}_{m+1} - \widetilde{Y}_{m-2})(\widetilde{Y}_{m+1} - 2\widetilde{Y}_m + \widetilde{Y}_{m-2})}{(\widetilde{Y}_{m-1} - \widetilde{Y}_m)(\widetilde{Y}_{m-1} - \widetilde{Y}_{m-2})(\widetilde{Y}_{m-1} - 2\widetilde{Y}_m + \widetilde{Y}_{m-2})}$

$$b_3 = -(b_1 + b_2 + b_4) \qquad b_4 = 2\frac{\widetilde{Y}_{m-1} - 2\widetilde{Y}_m + \widetilde{Y}_{m-2}}{\widetilde{Y}_{m-1} - \widetilde{Y}_{m+1}}$$

The y-component of the velocity vector is calculated using the continuity equation. It is written in finite difference form as follows:

$$\frac{1}{2}\left(\frac{C_1U_{i-2,m} + C_2U_{i-1,m} + C_3U_{i,m}}{X_i - X_{i-2}} + \frac{C_1U_{i-2,m-1} + C_2U_{i-1,m-1} + C_3U_{i,m-1}}{X_i - X_{i-2}}\right) + \frac{V_{i,m} - V_{i,m-1}}{\widetilde{Y}_m - \widetilde{Y}_{m-1}} = 0 \tag{5.30}$$

The introduction of central differences scheme to the boundary layer momentum equation results in a matrix equation of the form:

$$\sum_j H_{i,j}U_j = R_i \tag{5.31}$$

The $H_{i,j}$ matrix is tridiagonal with elements that contain the initially unknown U_j.

$$A_iU_{i-1,m} + B_iU_{i,m} + C_iU_{i+1,m} = R_{i,m} \tag{5.32}$$

by used the uniform grid

$$\begin{aligned}
A(i) &= -\frac{nu}{(Y(i+1,m) - Y(i,m))^2} - \frac{v(i,m)}{2(Y(i+1,m) - Y(i,m))} \\
B(i) &= \frac{2nu}{(Y(i+1,m) - Y(i,m))^2} + \frac{u(i,m)}{(X(i,m+1) - X(i,m))} \\
C(i) &= \frac{-nu}{(Y(i+1,m) - Y(i,m))^2} + \frac{v(i,m)}{2(Y(i+1,m) - Y(i,m))} \\
D(i) &= \frac{u(i,m)^2}{(X(i,m+1) - X(i,m))} + Px(m)
\end{aligned} \tag{5.33}$$

The basic problem was solved by using an iterative schemes in Triple Deck approach developed by Jobe and Burggraf [31]. A flow chart of the computer program is shown in Figure 5.4, the main program contains three nested loops: an inner loop in which the velocity profile and pressure are calculated for a given displacement function A(X), a middle loop in which the computation is advanced through the complete range of X, and an outer loop in which A(X) is recomputed according to the Hilbert integral until convergence is obtained to the desired degree of accuracy.

The inner loop of the main program solve the boundary layer equations of the lower deck for that pressure gradient $P'(X)$ which will produce the velocity, U_e, and thereby $A(X) = U_e - Y_e$ with Y_e fixed. The method of solution is to compute the velocity profile

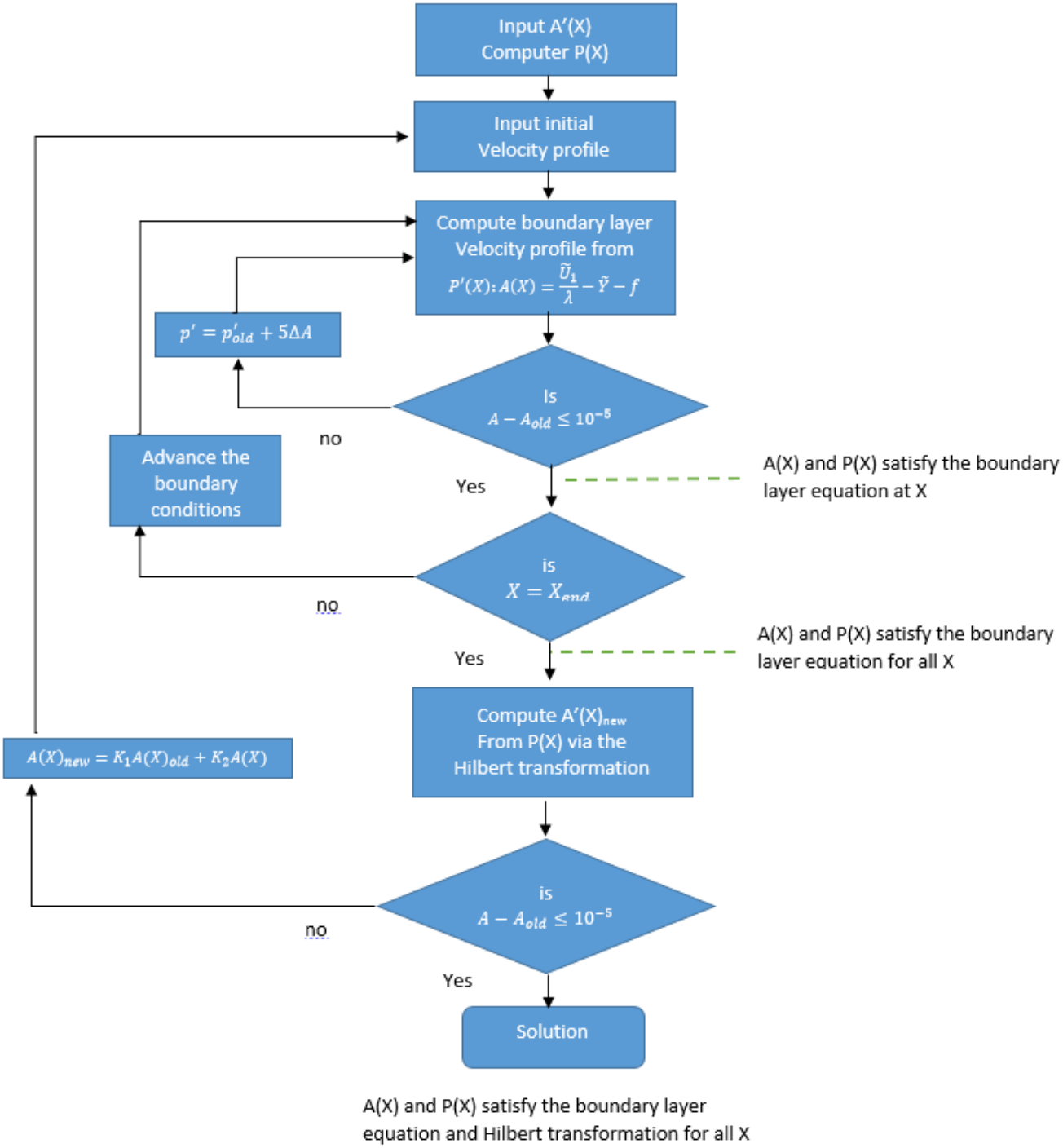

Figure 5.4: A flow chart of the program, [31]

by means of the iterative boundary layer subroutine with the input $P^{'}(X)$, determine the difference between the computed $A(X)$ and the requested $A(X)$, and then use this difference to correct $P^{'}(X)$.
$P^{'}(X)_{new} = P^{'}(X)_{old} + 5\Delta A(X)$. After several iterations, the program exits from the inner loop with the $P^{'}(X)$ required to produce the requested $A(X)$, and proceeds stepwise downstream via the middle loop. If we know the approximation of $A^{n}(x)$, then at each line $x = x_i$ the equation for vorticity is solved by the tridiagonal matrix method consecutively from the bottom to the top of the grid with the boundary conditions of the Lower Deck. Then the computations are transferred to the next line x. At the completion of the middle loop, the $P^{'}(X)$ required to produce the requested $A(X)$ has been determined for all X. The outer loop now computes the $A^{'}(X)$ corresponding to the new P(X) from the Hilbert transformation subroutine. Comparing the new $A(X)$ with the $A(X)$ from the previous iteration determines if the program has converged. If not, A(X) is replaced according to the formula, $A(X) = kA(X)_{old} + (1-k)A(X)_{new}$, and the outer loop reinitiates the streamwise traverse of the lower deck until the differences between succeeding A(X) iterates is less than 10^{-5}.

5.5 Numerical results and discussion

In this section we present results from the numerical solution of the non-linear Triple-Deck problem for subsonic flow past a surface waviness. The results depend on the rippled shape Figure 5.5 which is chosen as.

$$Y(x) = hsin(\frac{2\pi}{L}x) \tag{5.34}$$

With h are the amplitude of he wave and L its wavelength.

To find the resulting flow field and in particular the deplacement function and pressure it is necessary to solve the non-linear lower-deck equation. The solution of Lower Deck equations requires special numerical techniques. Now we discussed the numerical data for the two functions, $A(X)$ and $P(X)^{'}$, with the predicted asymptotic method (Triple Deck). The satisfaction of the asymptotic boundary conditions is of major importance in assessing the accuracy of the numerical procedure. As shown by Mengaldo [44] to compared two substantially different approaches, namely DNS and asymptotic Triple-Deck theory, for calculating the flow past an isolated roughness element on a flat plate with separation behind the element in some situations, they

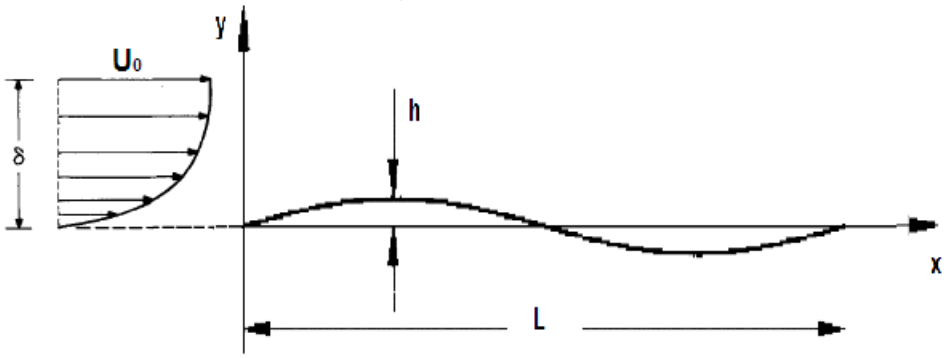

Figure 5.5: Parameters for a pure sinusoidal surface

demonstrates that the asymptotic Triple-Deck theory captures correctly the qualitative physics and the main flow as well as the DNS approaches.

Several tests are imposed to determine whether the mesh spacing and precision is adequate to resolve details of the flow. The calculations were performed using a non-uniform mesh (400×400) a concentration of the mesh points was arranged: $dx = 8.18 \times 10^{-5}$, $dy = 3.75 \times 10^{-6}$ and gradually reduced to 4.17×10^{-7}.

The results of the calculations are summarized in Figure 5.6, which shows the comparison of the velocity upper the surface waviness, the displacement function A(x) and the pressure p(x) as a function of the scaled length.

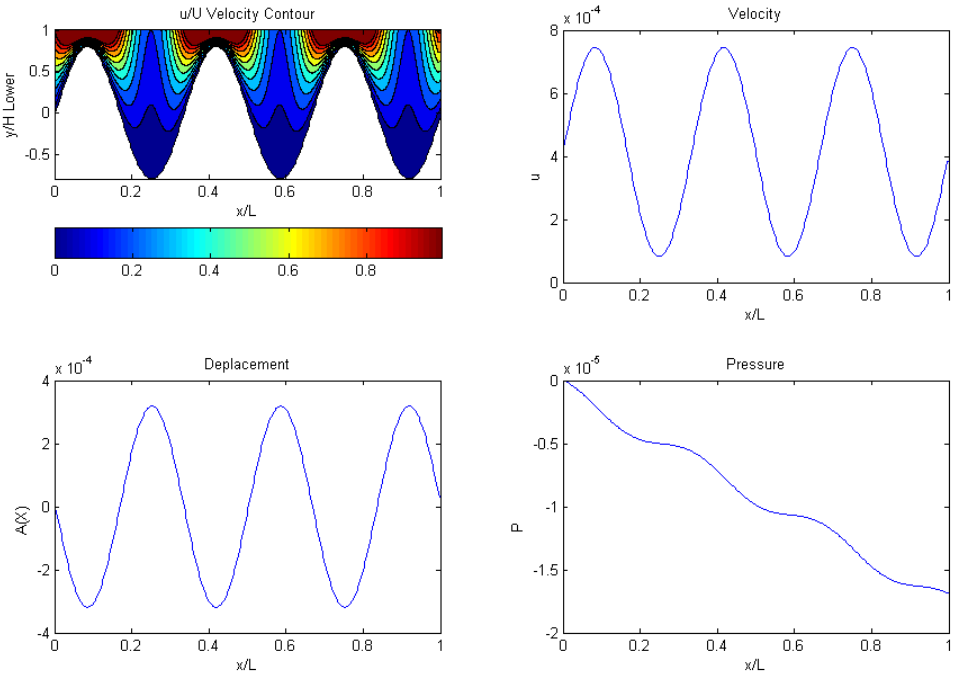

Figure 5.6: A summary of the numerical results for h/Lower Deck = 0.8, Cycle = 3 and U = 5 ms^{-1}

The detailed results of the Triple-Teck analysis show that the predominant effect of the surface waviness on the boundary layer is to cause a local distortion in the impressed pressure. We seen that far upstream, where the interaction region matches with the unperturbed boundary layer, the deplacement and the pressure perturbation are null. As the pressure starts to decrease in the interaction region, it cause the flow in the viscous sublayer to "decelerate". This is revealed by the observed "increase" of the deplacement function.

The displacement A(x), pressure P(x) and velocity u(x) are predicted by present theory for various height $h/H_{LowerDeck}$ ratios and cycle of the surface waviness for different cases: [U_0 = 5, 50 m/s].

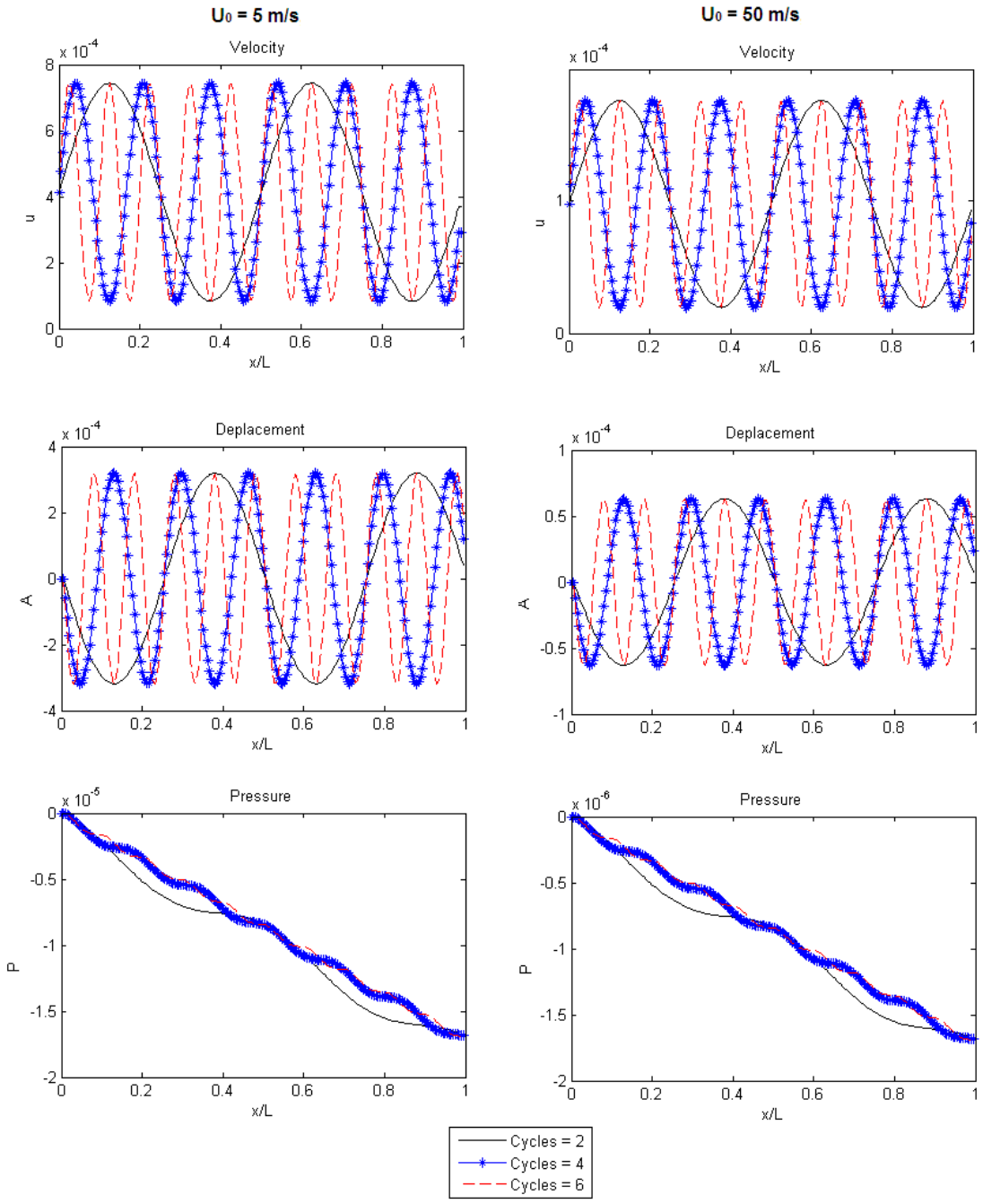

Figure 5.7: Lower deck displacement function, A(X)

In Figure 5.7, a detailed comparison of the displacement function A(x), pressure and velocity is conducted for the tree solutions with different cycle and incoming flow. In Figure 5.8 we show the same quantities for different height $h/H_{LowerDeck}$ ratios. In the surface waviness produces a favourable pressure gradient, followed by an adverse

pressure gradient, the distortion becomes greater as the heigh increases.

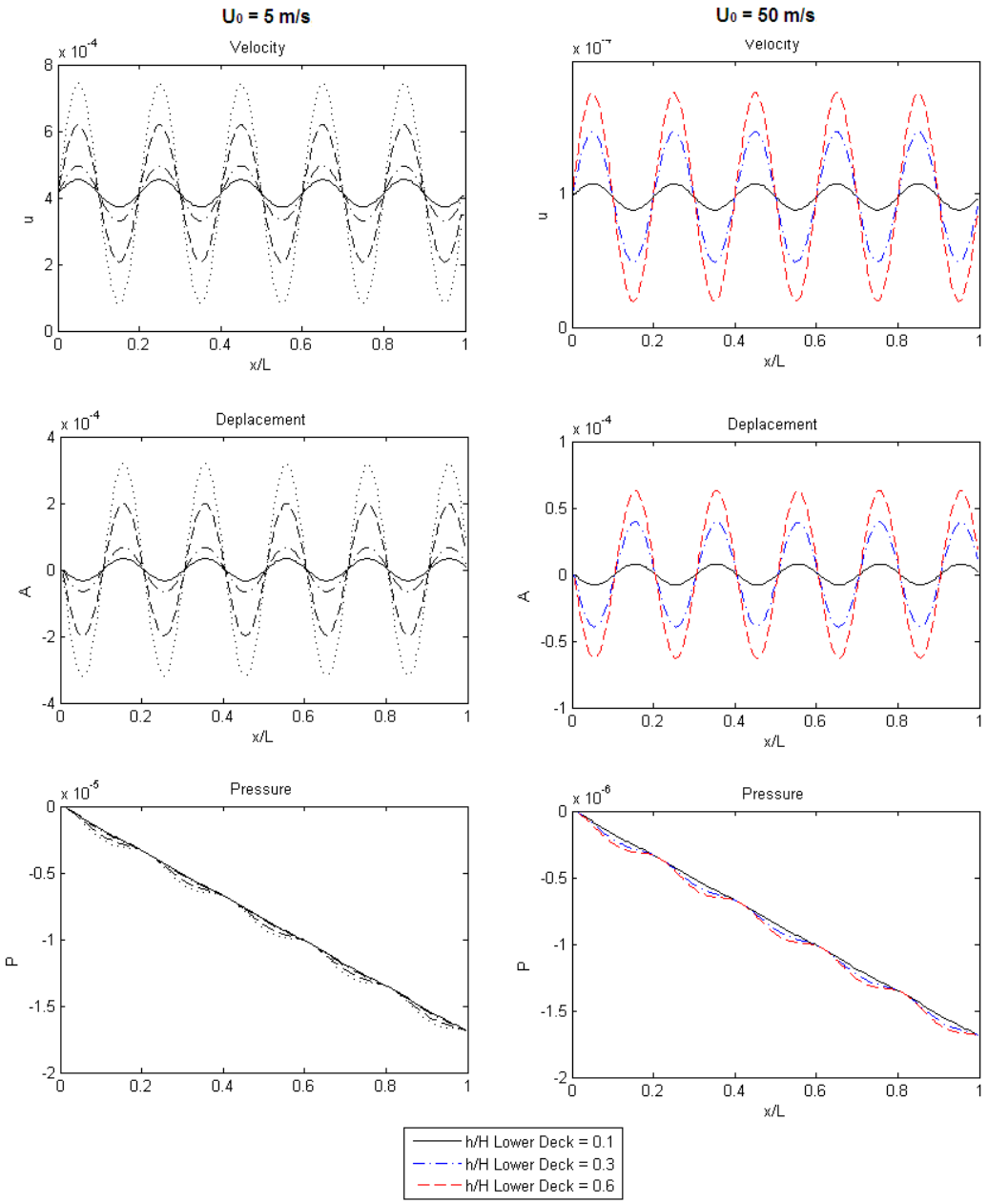

Figure 5.8: Numerical solution for A, P and u with various amplitudes of surface waviness

At low and high values of the free-stream Reynolds number Re based on the distance from the leading edge to the surface waviness L_0, the effect of the surface

waviness on the displacement A diminishes. The effect continues when Re is varied by hanging either the free-stream unit Reynolds number or the distance L_0.

5.6 Closure

We have formulated the problem of subsonic flow past a surface waviness placed on a flat plate. New results have been presented, obtained by numerical solution of the non-linear Triple-deck equations, which serve to identify the effects of frequency and the height (Amplitude) of the wave in the distribution of the displacement and pressure. They also constitute a concrete step towards understanding the mechanism of momentum transfer between inviscid flow outside and viscous sub-layer.

The Mach and Reynolds numbers were chosen to be relevant for aeronautical applications, while the shape and the related parameters can be seen as simple models of small deformation placed at the leading edge of the aircraft landing gear cavity.

Clearly the size and shape of the surface waviness are important factors to be taken into consideration in designing suitable forms which can be used to control the flow and separation of the boundary layer. Although for this particular application it is understood that effects of turbulence, unsteadiness of the flow may also be important, and should be included when considering the full problem.

CHAPTER 6

RESULTS

6.1 Results for Two Dimensional simulations

Numerical simulations are used to investigate the self-sustained oscillating flows past an open cavity. The two-dimensional incompressible Navier-Stokes equations are solved directly by using the finite difference method. A series of simulations are performed for a variety of surface waviness amplitudes and frequencies.

6.1.1 Aerodynamics

Flow dynamics inside the cavity is driven by the shear layer, developing above the cavity, and a main vortex, developing along the whole cavity span. The predictions of instantaneous velocity flow field from LES simulations are shown in Figure 6.1.

Shear mode The test case (Ampl. 0 Cyc. 0) oscillates in shear mode. Figure 6.2 illustrates instantaneous vorticity contours in the cavity flow-field at different flow time after 60 computational periods. The turbulent boundary layer which separates from the leading edge of cavity forms an oscillating shear layer. Figure 6.2(a) shows the shear layer stretching from the upstream of the cavity and is parallel to the bottom of the cavity. Over the right upper corner of the cavity, shear layer with a tongue like structure extends to the downstream of the cavity from the vortex near to the vertical wall of the cavity. Figure 6.2(b) describes the complex interaction between the shear

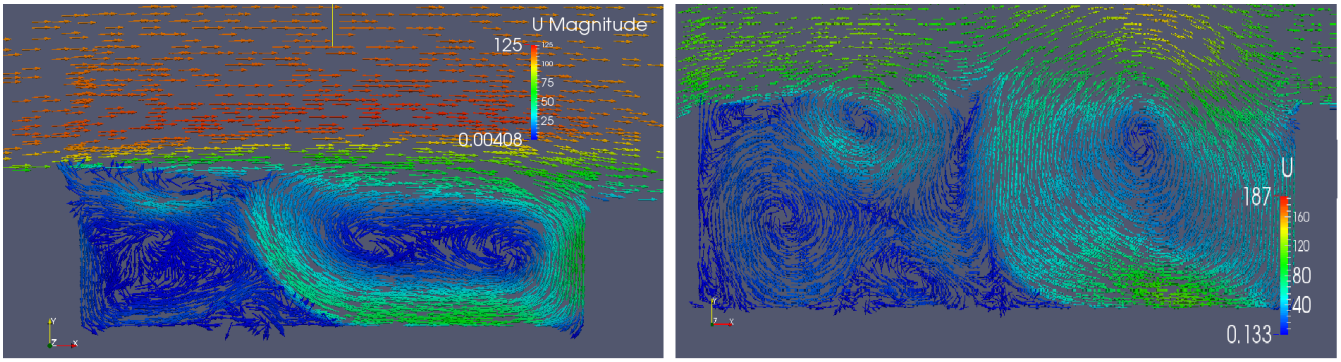

a) Baseline cavity **b) Wavy cavity with Ampl. 3.25 Cyc. 3**

Figure 6.1: Instantaneous flow field from LES simulations

layer and the vortex at the downstream wall of the cavity. The incoming shear layer extends until the middle of the cavity region and the lip of the shear layer swipes on the vertical wall at the trailing edge of the cavity. (The swiping action cuts the tongue like shear layer to travel downstream of the cavity.) The shear layer which extends due to the oscillation, impinges on the upper right corner of cavity and breaks into two (see Fig. 6.2(c)) and at time period 3T/4 i.e in the Figure 6.2(d), one part of the lip of the broken shear layer enters the cavity creating a eddy close to the downstream wall with the size of cavity depth, while the other part of the shear layer moves downstream of the cavity with less energetic eddies.

Wake mode Figure 6.3 shows the instantaneous vorticity fields U over a period. A vortex is formed from the trailing edge and fills the cavity region is shown in Figure 6.3(a). In Figure 6.3(b), the vortex detaches and impinges on the downstream corner of the cavity. Due to the impingement, is ruptured and moves out of the cavity, while another eddy enter the cavity from the leading edge of the cavity (see Fig. 6.3(c)). The eddy which is broken at this point of time moves downstream of the cavity, while another new eddy grows to fill the cavity is shown in the Figure 6.3(d). The flow above the cavity region is affected by the flow from the cavity.

6.1.2 Aeroacoustic

Acoustic Parameters The pressure perturbations $p^{'}$ ($p^{'} = p - p_0$) which propagate as waves and which can be detected by the human ear. For harmonic pressure

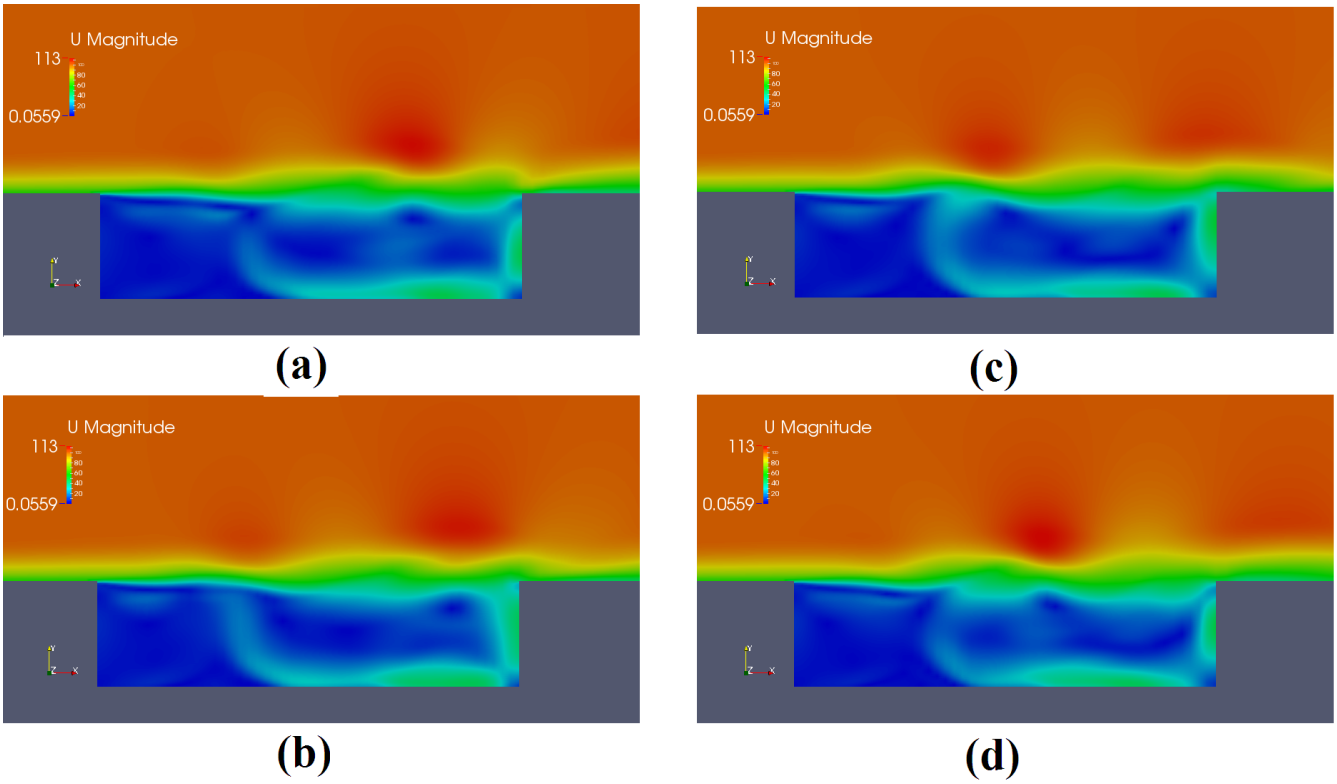

Figure 6.2: Instantaneous vorticity contours in the baseline cavity. (a) 60.25T; (b) 60.5T; (c) 60.75T (d) 70T; (T is numerical simulation period).

fluctuations the audio range is:

$$20Hz \leq f \leq 20kHz \tag{6.1}$$

The Sound Pressure Level (SPL) is a logarithmic scale measure of the pressure unsteadiness in which the minimum pressure fluctuation detected by the human ear $p_{ref} = 2 \times 10^{-5} Pa$ is taken as the reference. For continuous pressure signals, the SPL is defined by:

$$SPL = 10\log(\frac{PSD}{p_{ref}}) \tag{6.2}$$

The PSD describes how the power of a signal or time series, in our case the time dependent pressure, is distributed with frequency. The PSD spectrum is determined by means of a Fast Fourier Transform (FFT) utilizing windowing as to smoothen the PSD estimate, in our case the Hanning window. The FFT of a signal P(t) is defined as

$$FFT(t,f) = \int_{-\infty}^{\infty} P(\tau) w(\tau - t) e^{-j2\pi f \tau} d\tau \tag{6.3}$$

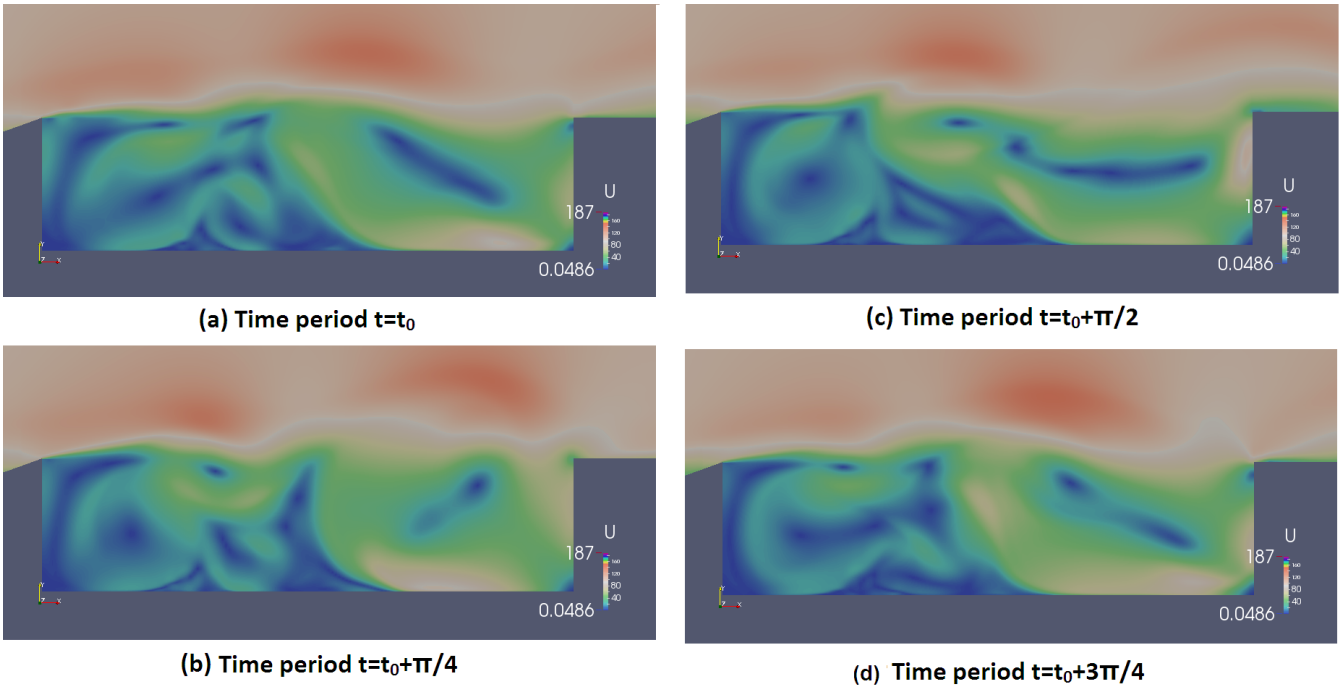

Figure 6.3: Instantaneous vorticity fields U for wake mode at four different times (a-d) corresponding to approximately a quarter of a period of oscillations. Only a small portion of the computational domain near the cavity is shown.

where w(t) is the Hanning window function, applied to obtain a clear definition of the fundamental frequencies. Time averaging the pressure fluctuations one would obtain the mean pressure $\bar{P} = \frac{1}{N-N_0}\sum_{k=N_0}^{N} P_k(t)$ where N is the total number of samples taken and N_0 is the first sample number at which the time averaging starts. The root mean square pressure is therefore calculated via the equation: $P_{rms} = \frac{1}{N-N_0}\sum_{k=N_0}^{N}\left(P_k(t)-\bar{P}\right)^2$ Using the acoustic spectrum results, an overall sound pressure level (OASPL) can be obtained by adding all noise amplitudes of the spectrum, the OASPL can be obtained applying the following expression:

$$OASPL = 20log\sqrt{\sum_i (10^{SPL_i/20})^2} \tag{6.4}$$

Sound pressure levels (SPL) for the acoustic field above the cavity predicted by Rowley, et al [56] and paper are shown in Figure 6.4, peak radiation to the far field occurs at an angle of about 135^0 from the downstream axis.

The setup of Curle's acoustic analogy The setup is done in the file named "CurleAnalogy" in the directory "system". The start and end time of sensing acoustic quantities,

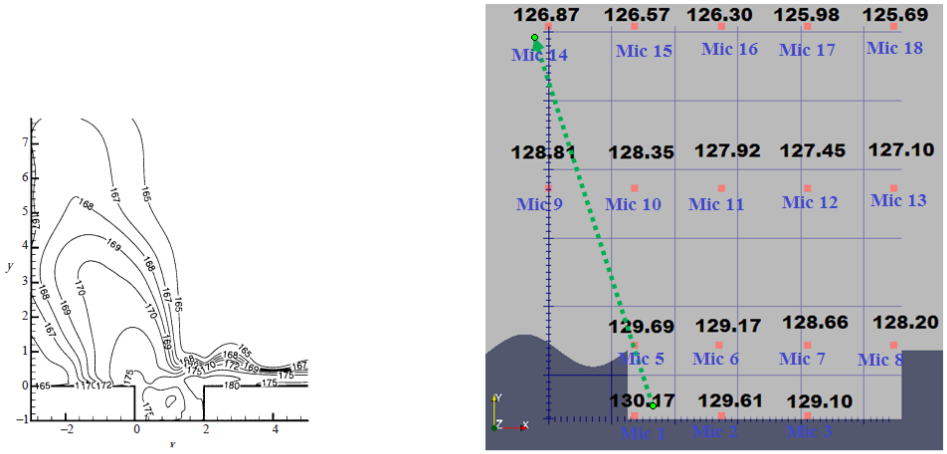

(a) (b)

Figure 6.4: SPL distributions. (a) 2D-DNS predicted by Rowley, et al. [56]; (b) 2D-LES with surface wavy

the source object cavity, the speed of sound in the medium c, the reference density ρ, pressure p and the reference sound pressure p_A are defined in this file. Furthermore, receivers' (the probes) positioning, the sampling frequency for evaluating a fast Fourier transform are defined. The aeroacoustic simulation result is shown in the following chart. Figure 6.5 shows the sound pressure level of the computed acoustic signal at $M_\infty = 0.3$ (flow velocity 99.44 m/s). The spectral resolution of these results is 6.97 Hz. over the whole frequency range [0-10000] Hz. From the acoustic analysis it can be seen that the significant peak of the sound pressure level is at the frequency 2000 Hz correspond to the 2^{nd} Rossiter mode. The highest sound pressure level at this frequency is 129 dB (for receiver A, Figure 4.12). the peaks at 840 Hz, 2000 Hz, 4080 Hz, 6122 Hz, 80150 HZ and 10300 HZ correspond very well to the results predicted by Rossiter, Eq. 2.6. (see Table 6.1) We now discuss the results obtained for $M_\infty = 0.3$ cavity flow: It is seen that in Figure 6.6 the cavity for an applied surface waviness with frequency of 19.7×10^{-3} and 11.8×10^{-3} cycles per mm increase the resonance peak by 9 dB compared to the baseline case and also the peak of the sound pressure level is at the frequency 1000 Hz correspond to the 1^{st} Rossiter mode for wake mode. Figure 6.7 shows frequencies of the two most energetic peaks in the spectra for the series of run with $\frac{L}{D} = 4$, compared to experimental data and predictions from Eq. 2.6, the transition to wake mode oscillations for M > 0.3. The results for surface wavy control, Figure 6.8, show a considerable attenuation of the dominant Rossiter peak, it was clarified that

m	St	f(Hz)
1	0.412	807.60
2	0.962	1884.39
3	1.512	2961.19
4	2.068	4037.98
5	2.612	5114.78
6	3.163	6191.57
7	3.713	7268.37
8	4.263	8345.16
9	4.813	9421.96
10	5.363	10498.75

Table 6.1: Longitudinal Rossiter modal frequencies for cavity length of 50.8 mm with associated Strouhal Numbers [54]

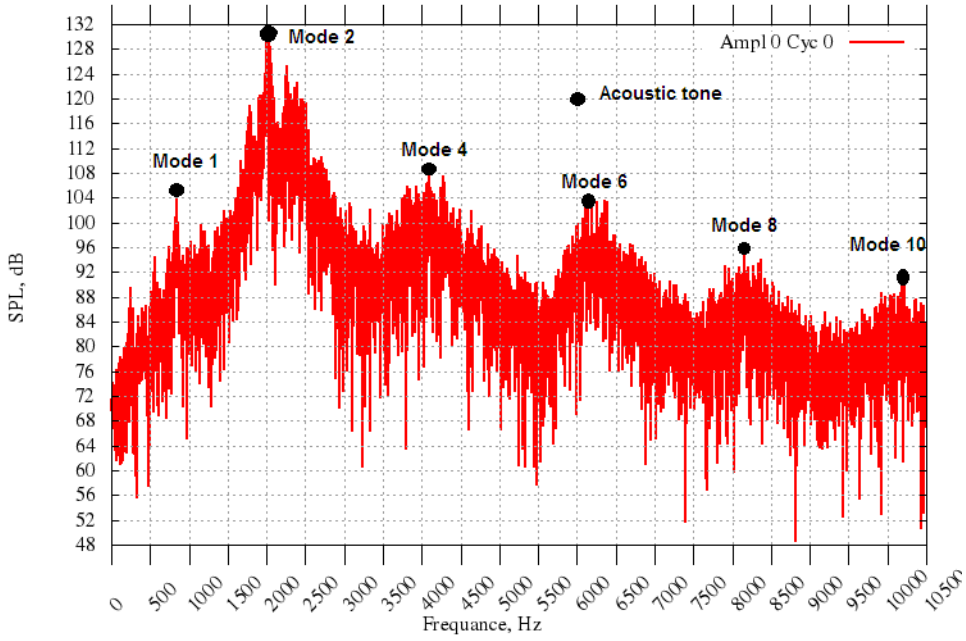

Figure 6.5: SPL at one receiver for baseline cavity

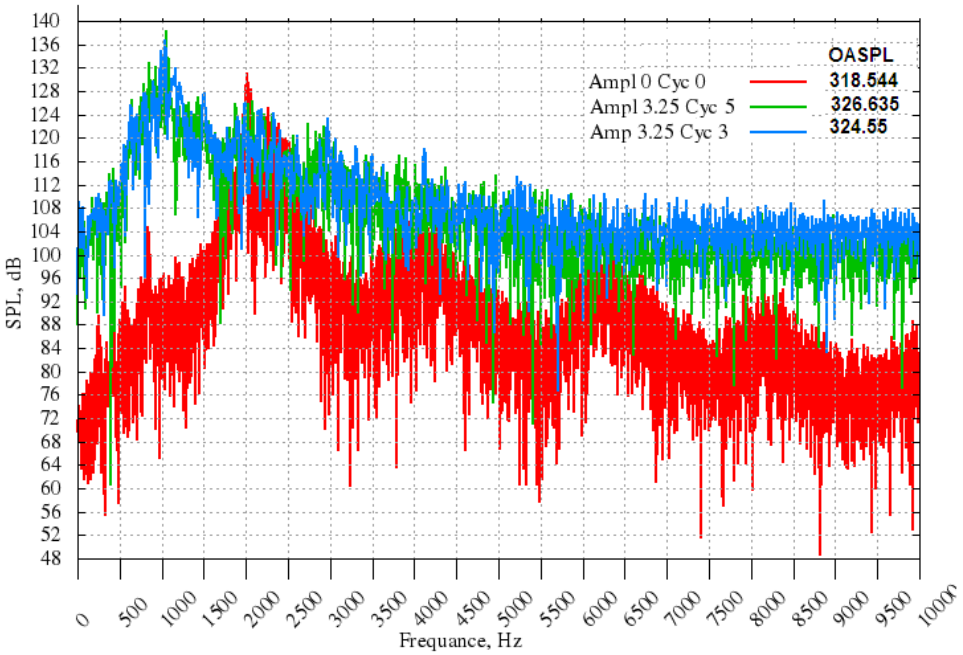

Figure 6.6: Sound pressure level with and without surface waviness

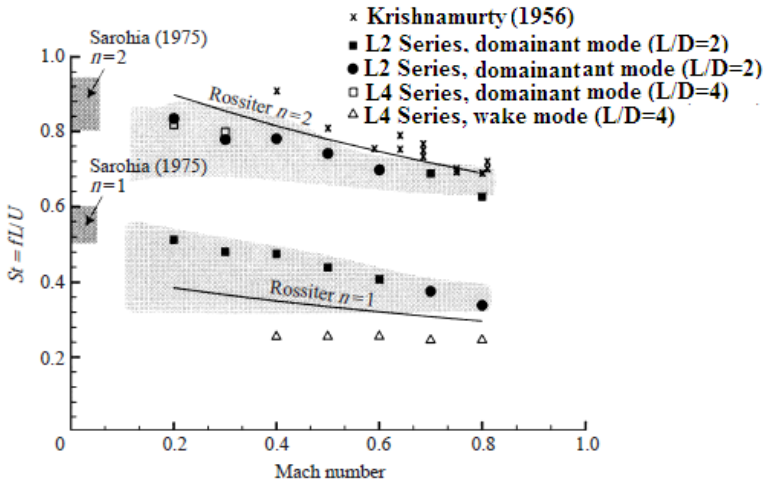

Figure 6.7: Strouhal numbers for peaks in spectra for the shear-layer mode and wake modes

the tonal sound reduced for frequency of 4.92×10^{-3}, 9.84×10^{-3} cycles per mm. The maximum noise level of 116 dB was observed at f= 625 Hz for frequency 4.92×10^{-3} cycles per mm and the maximum noise level of 127.8 dB was observed at f = 1095 Hz for frequency 9.84×10^{-3} cycles per mm. It was observed that the attenuation achieved using this configuration was of the highest value, giving an overall reduction in SPL of 14 dB.

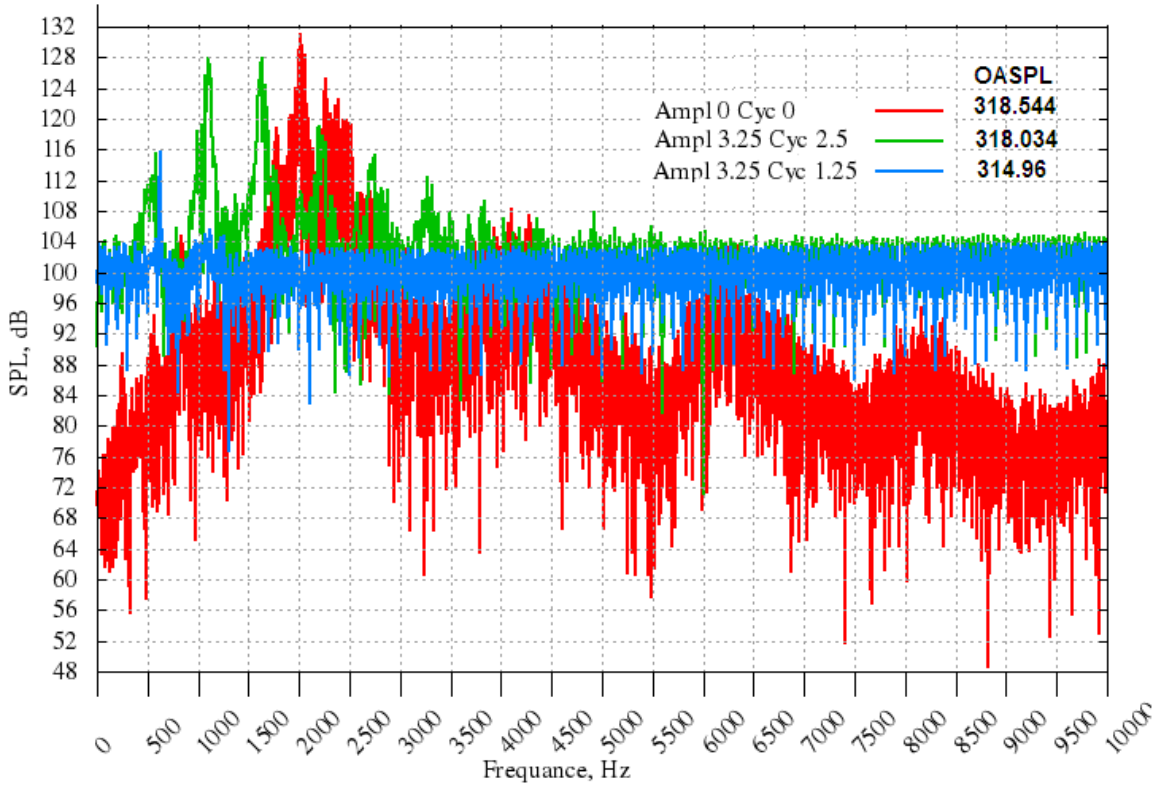

Figure 6.8: Sound pressure level with and without surface waviness

6.1.3 Closure

A complete two-dimensional analysis of both the baseline and the modified configuration were carried out. Additionally the flow regime was demonstrated with success by the use of CFD code (OpenFOAM). The results of different geometry modifications applied to the leading edge of a cavity with length to depth ratio of 4, in order to reduce the resonance of flow at $M_\infty = 0.3$ have been presented. The amplitude of 3.25 mm and the frequency of 4.92×10^{-3} cycles per mm was observed as achieving the best reduction in cavity resonance.

"At this stage a quantitative comparison (with the experimental) is still not possible because of the 2D acoustic simulation. In fact, due to the 2D propagation, the pressure intensity is overestimated intrinsically".

6.2 Results for three Dimensional simulations

6.2.1 Flow Results

Figures 6.9 show the flow structures generated by both cases with and without surface waviness. The reference case (baseline) is located on the left hand side and the wavy cases are located on the right hand side. One of the major differences between the two cases is the fact that the applied surface waviness accelerated the flow ahead of the cavity. The flow field clearly oscillates in a shear layer mode. The visualisation of the free shear layer over the cavity shows a marked decrease in the recirculation of flow structures in the case with the surface waviness.

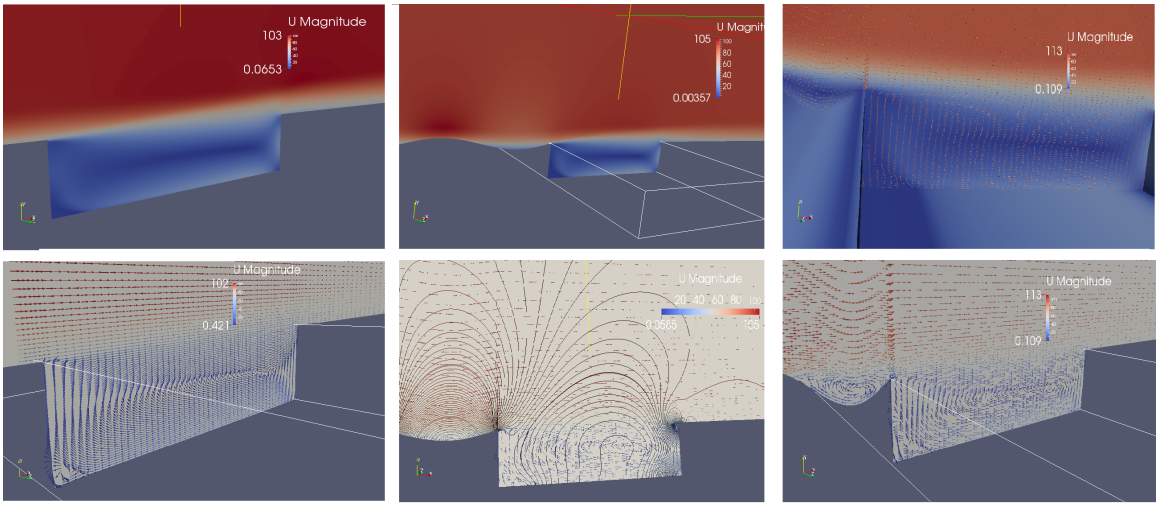

Figure 6.9: Velocity contour for both: a) Flat Case (left) and b) Wavy Case (right) located at the cavity central line

The computed flow inside the cavity was found to be highly unsteady and dominated by periodic phenomena. Tubular vortical structures inside the cavity were seen to affect the shear layer (Fig. 6.10), but overall the shear layer spanning the cavity width is found to be more stable in the case with the surface waviness. In addition, Tubular

structures are seen to arrive at the cavity leading edge but these structures do not have sufficient energy to cause the violent flapping of the streaks of the separated shear layer.

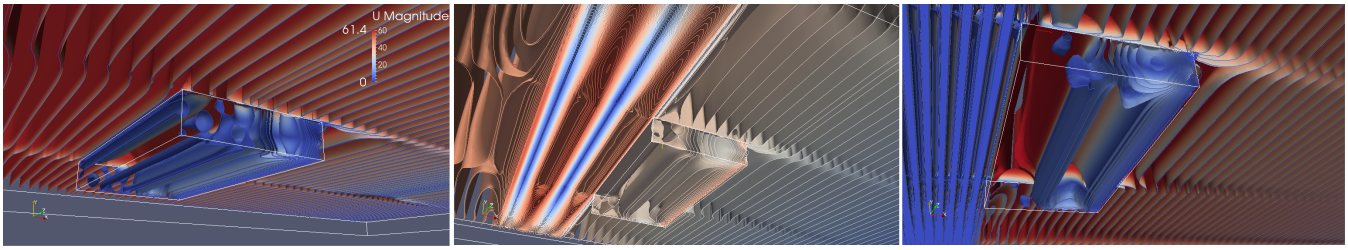

Figure 6.10: Pressure iso-surfaces, coloured by velocity, showing flow structures in the cavity; L/D=4, $M_\infty = 0.3$; (a) clean cavity and (b) cavities with surface waviness

To understand the effect of the control method on the cavity flow, the streamwise velocity component together with the associated streamlines are plotted in Figure 6.11. For appropriate form of surface waviness, a slow circular motion can be observed inside the cavity. From the baseline case, as the surface waviness parameters (Amplitude and cycle) were increased, the major changes in the structure of the flow field were concentrated in the region close to the rear wall. In other side the strength of this vortex velocities increase with reduction of those parameters. As the flow separates at the upstream edge of the cavity, a large-scale vortical structure grows as it travels downstream, and impinges on the downstream edge of the cavity. Part of the vortex spills over the cavity, while the rest of the vortex rolls underneath the downstream cavity edge. The rolled-up vortex inside the cavity interacts with the next vortical structure inside the shear layer and the unsteady motion of the shear layer, causes the formation of compression wave due to the inflow/outflow of the external fluid into the cavity. These waves propagate outward as acoustic wave and travel upstream. It can be seen that a larger recirculation bubble forms which is approximately 70% of the cavity length starting from the aft wall. At the upstream edge of the cavity, the pressure difference inside and outside of the cavity further excites the shear layer. This external excitation provides the link to the feedback mechanism.

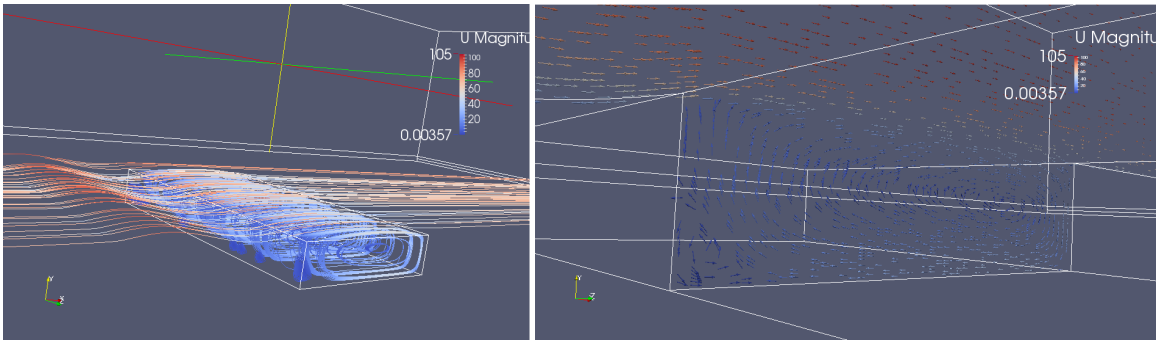

Figure 6.11: Streamline and streamwise Velocity for Wavy Case

6.2.2 Acoustic Results

In order to validate the results obtained, a comparison between Ahuja's [5] experiments and the DES simulation (Fig. 6.12), for the L/D = 3.75, M= 0.4. The second-mode feedback frequency appears to be the most dominant tone.

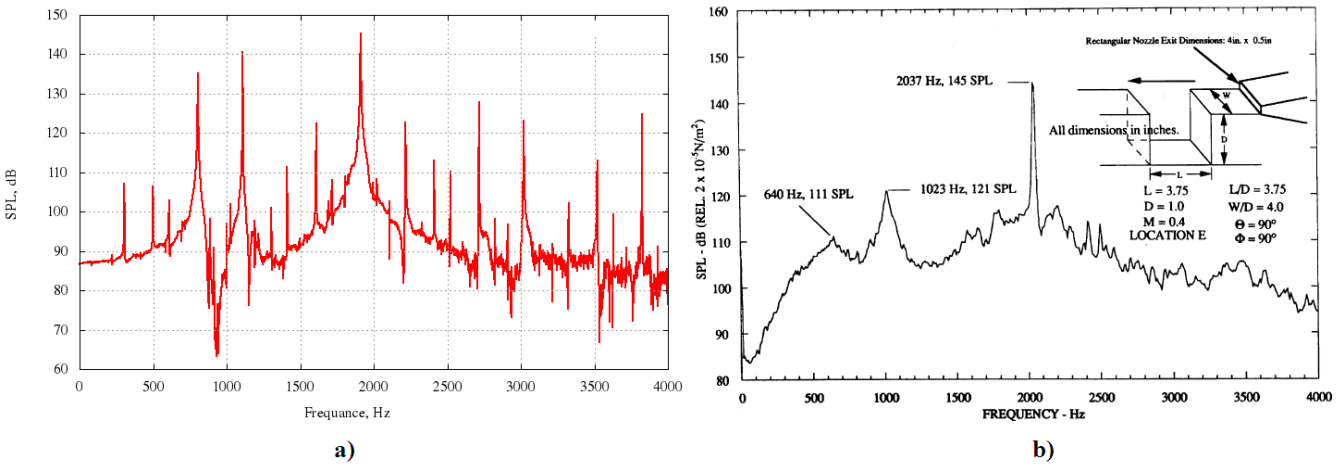

Figure 6.12: Case for L/D=3.75 and $M_\infty = 0.4$. a) clean cavity DES simulation, b) Ahuja experience [5]

It can be seen that the sound pressure level appear to be highest in the simulation because there's some interferences between the jet and the sound field of the cavity in the Ahuja experience.

Figure 6.13 show the numerous sum or difference interactions between the mode I, f_a, and the mode II, f_b of the Rossiter feedback loop (Table 6.2) [24]. The sound field appears to be a result of constructive and destructive interference between pressure waves of the same frequency with potentially different origins.

$f_a + (f_b - f_a) \rightarrow f_a$	$(f_b - f_a) + 2f_b \rightarrow (3f_b - f_a)$
$f_a + f_b \rightarrow (f_b + f_a)$	$2f_b - (f_b - f_a) \rightarrow (f_b + f_a)$
$f_b - f_a \rightarrow (f_b - f_a)$	$f_b + (f_b + f_a) \rightarrow (2f_b + f_a)$
$(f_b + f_a) - f_a \rightarrow f_b$	$f_b - (2f_b - f_a) \rightarrow (3f_b - f_a)$
$f_a + (2f_b - f_a) \rightarrow 2f_b$	$(2f_b - f_a) - f_b \rightarrow (f_b - f_a)$
$f_b - (f_b - f_a) \rightarrow f_a$	$f_b + 2f_b \rightarrow 3f_b$
$(f_b - f_a) + (f_b + f_a) \rightarrow 2f_b$	.....

Table 6.2: Multiple tones interaction in cavity [24]

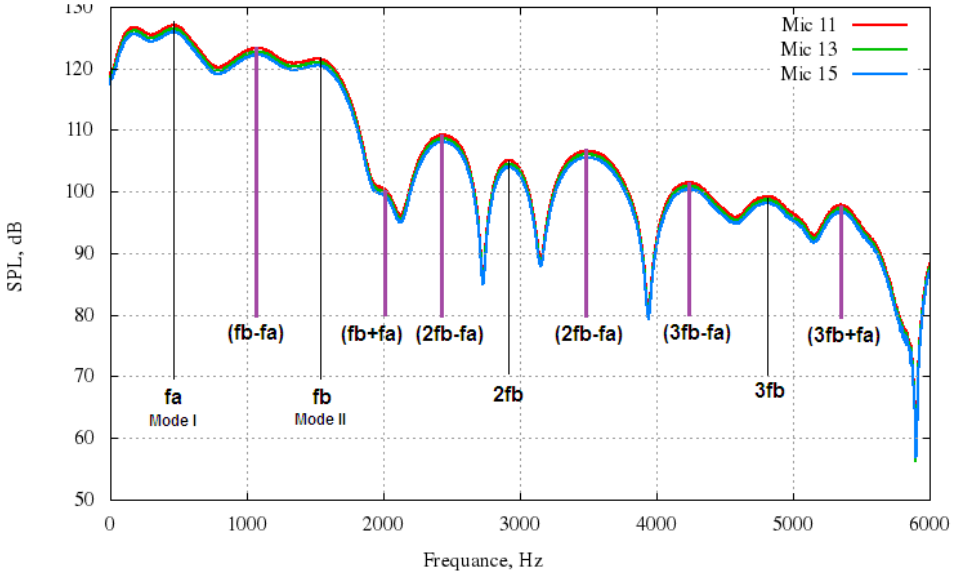

Figure 6.13: Three dimensional cavity frequency multiple interaction for L/D=4, $M_\infty = 0.3$ [24]

Many tones are visible, with the first tone mode clearly having the highest amplitude. This first-mode dominance was also seen in various microphone locations around the cavity, as shown in Figure 6.14 (see Fig. 4.19 for positioning).

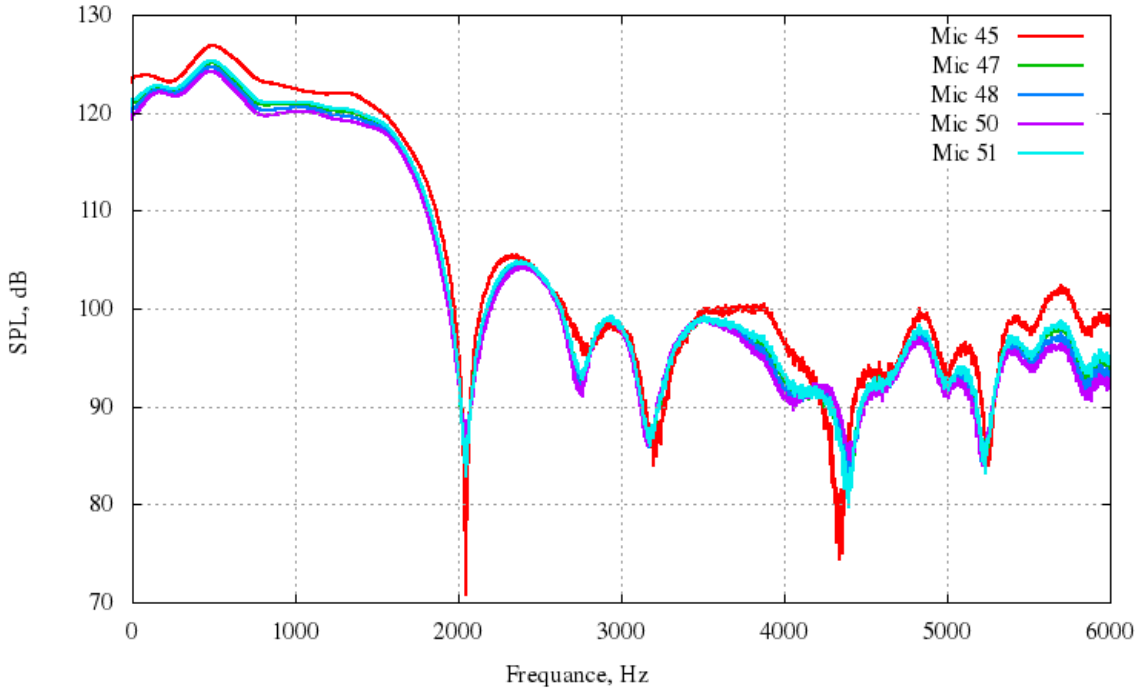

Figure 6.14: SPL at different microphones positions

Figure 6.15 show a comparison of the two and three dimensional SPL spectrograms. we seen the presence of high intensity peaks within the signal, the frequencies of which are compared with the theoretical Rossiter frequencies calculated using equation (2.6) are indicated as R1, R2, R3 and R4 corresponding to the first, second, third and fourth feedback mode tone frequency, respectively. It can be seen in this figure that the frequencies of the simulated tones (3D case) are somewhat smaller than those predicted by Rossiter's equation. Also, the second and the third mode feedback tones are not as strong as the first mode tone. The fundamental mode agrees very well with Rossiter's formula, but the frequencies of the harmonic modes are under-predicted in the analysis. However, there is a wide scatter in the experimental data of Rossiter [54] and Tam and Bloc [7]. At a distance about four cavity depths along the peak radiation, the sound pressure level is about (10 dB) louder for the three-dimensional than two-dimensional cavity. The 2nd Rossiter mode has been reduced significantly, though the tonal peak which occurred at 2000 Hz in the two-dimensional case. For the three-dimensional case, the dominant frequency corresponding to mode 1 appears at around 500 Hz. As the width increases, the frequency of mode 1 appears very weak.

Such reduction in SPL is due to a dissipation in the 3rd dimension.

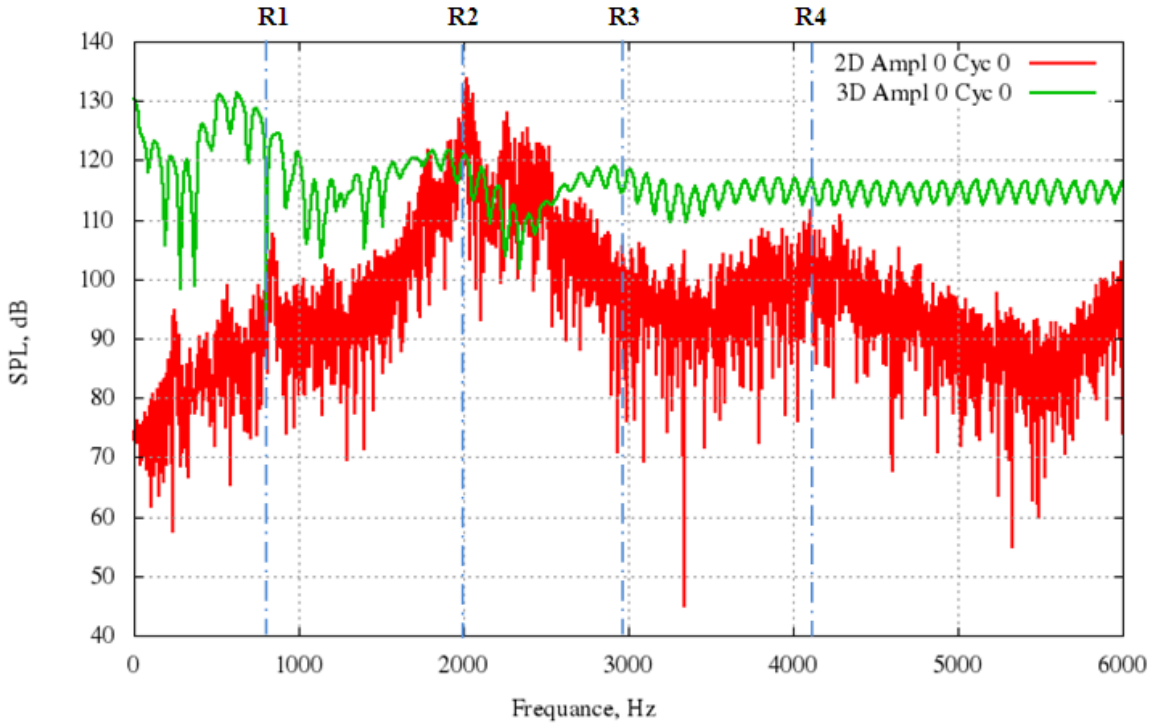

Figure 6.15: 2D/3D Comparison for clean cavity case, SPL spectrograms

OASPL's along the centerline of the cavity for the baseline case at different microphones positions are shown in Figure 6.16. There is a strong acoustic radiation in the upstream direction, about 135 degrees from the downstream axis. The source of the feedback sound for all modes is at the trailing edge.

Sound Pressure Level spectra, comparing the baseline case to the controlled cases for different surface waviness forms, are displayed in figure 6.17. The addition of the surface waviness controls the flow by modifying the stability of the mean velocity field. Once compared, three dimensional SPL spectrograms of cavity with and without surface waviness showed similar repartition in peak tones SPL.

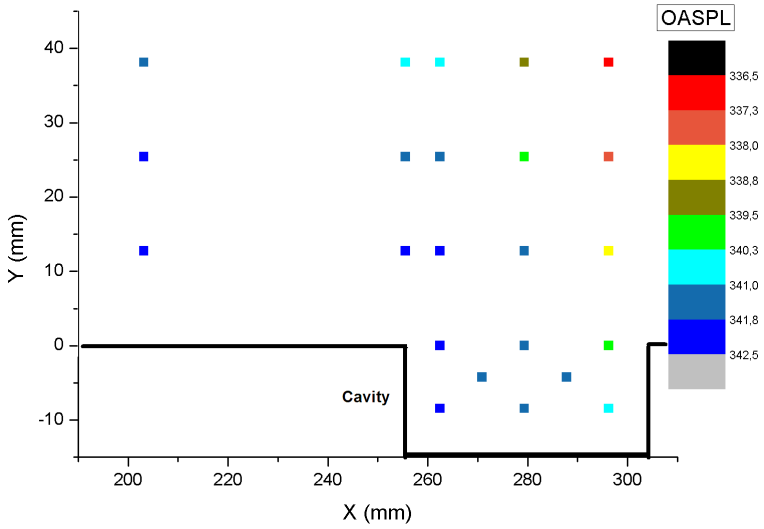

Figure 6.16: OASPL, in the centerline of the clean cavity

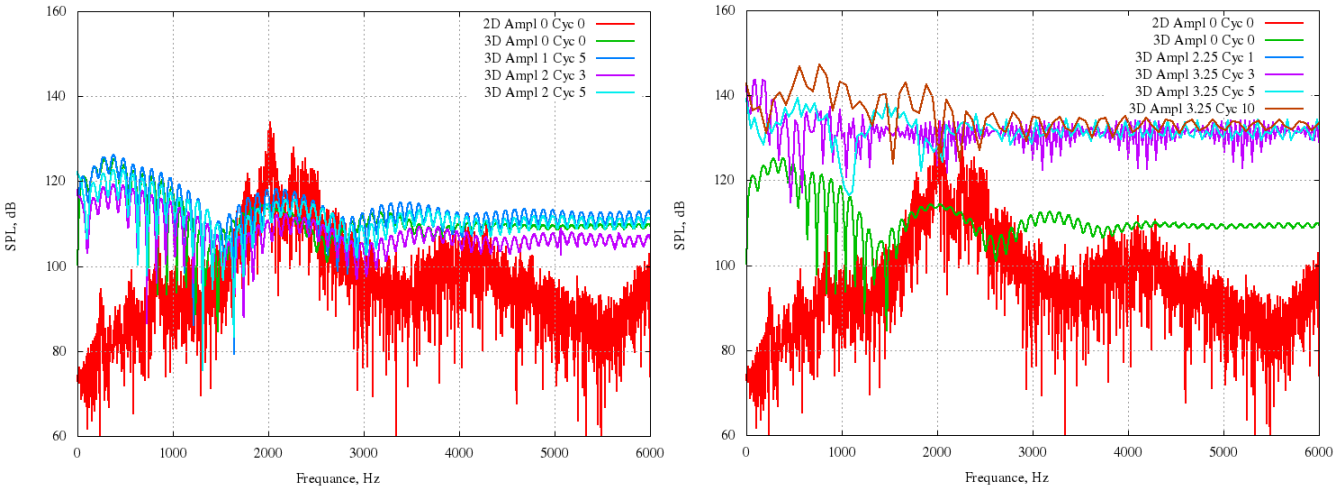

Figure 6.17: 2D/3D Comparison, SPL spectrograms

Table 6.3 shows the acoustic performance of each of the passive devices tested and compared to the baseline.

Over the plotted frequency range, the pressure fluctuations for (Ampl. 2, Cyc. 3) are on average about 8 dB greater than those that the baseline case. It can be seen that for the relatively values of surface waviness parameters, the method leads to a rapid attenuation of the SPL. In general, as the surface waviness parameters increased the peak tones were more sufficiently reduced. The overall suppression increased sharply when the amplitude of surface waviness takes 15-16 % of the cavity depth.

Surface waviness	OASPL dB	Delta OASPL dB	Peak Frequency dB
Ampl. 0 Cyc. 0	329.056	0	123.816
Ampl. 2 Cyc. 3	317.097	11.959	115.918
Ampl. 2 Cyc. 5	324.198	4.858	121.657
Ampl. 2.25 Cyc. 1	360.754	-31.698	136.276
Ampl. 3.25 Cyc. 3	361.448	-32.392	136.639

Table 6.3: acoustic performance of Wavy cases compared to baseline

In addition to those obtained at $M_\infty = 0.3$, the SPL are compared to the experimental data of Maureen's [43] in Figure 6.16 for $M_\infty = 0.6$. It can be seen that the presence of the wavy surface reaching a significant SPL in comparison to the empty cavity case.

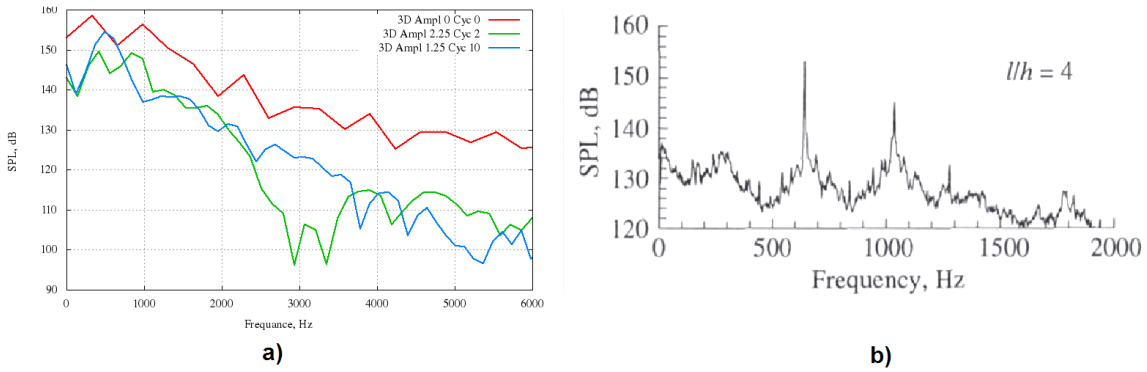

Figure 6.18: Case for L/D=4, W/D=1 and $M_\infty = 0.6$. a) clean cavity, b) Maureen experience [43]

6.3 closure

The results obtained from the use of surface waviness as a means of reducing the tones produced by the L/D=4 cavity at $M_\infty = 0.3$ are now considered. The objective of the surface wavy was to introduce disturbances into the shear layer in order to disrupt the resonant mechanism that sustains the cavity oscillations. The dominant frequency is changed from Mode 2 for the two-dimensional cavity to Mode 1 for three-dimensional cavity. Though more wavy surface where tested the three that was discussed in this thesis shown a performance extreme in the acoustic results and therefore a detailed analysis of how these wavy surface change the flow physics for the better or worst are done.

CHAPTER 7

CONCLUSIONS AND FURTHER WORK

The objective of this thesis is to study numerically the aeroacoustics of different geometry modifications applied to the leading edge of a cavity, in order to reduce the resonance of flow at low Mach number (M < 0.3) based on hybrid method.

The numerical approach is based on Large Eddy Simulations (LES) and Detached eddy simulation (DES) which are resolved using the OpenFOAM code. The acoustic analysis based on the Lighthill-Curle analogy has been performed to present the influence of the surface waviness on the mode of oscillation in the shallow cavity.

The flow over a cavity can be divided into three regions : An incoming turbulent boundary layer which develops and grows before reaching the cavity, the turbulent flow inside and above the cavity which can be distinguished into a wake mode and a shear layer mode, and the flow downstream of the cavity which is with or without surface waviness.

Two-dimensional and three-dimensional cavity flows were simulated with incoming thick turbulent boundary layer, with an constant aspect ratio of 4. The thickness of the boundary layer introduces a strong shear flow in the cavity which can oscillate at a dominant frequency, with a shear layer mode and wake mode with and without surface waviness respectively.

The aeroacoustic study has been done to analyse the acoustic sources. A large set of instantaneous pressure field was determined from large eddy simulation(LES) or Detached eddy simulation (DES) and used as an input to the Curle's analogy, to

compute the acoustic pressure of an observer region. The Sound Pressure Level (SPL), is related to the upstream velocity and the oscillating mode of the shear layer.

For two-dimensional case the amplitude of the surface waviness was first altered and tested and an amplitude of 3.25 mm was observed as achieving the best reduction in cavity resonance. After achieving an optimum amplitude the frequency was analysed achieving an optimal value of 1,25 cycles. Pressure fluctuations were extracted from a total of 18 points for each case. However, for three-dimensional case the optimal amplitude and frequency are 2 and 3 respectively.

Then, results from numerical simulations, including global modes, steady simulations , were compared to Rossiter mode, with and without the passive control surface waviness. Finally, the sensitivity analysis succeeded to control the flow means of a small control waves.

Mean SPL were compared for both clean cavity and cavity with surface waviness cases. The comparison of the numerical simulation with the experimental measurements for acoustic part has not been carried out yet. But this study proves the influence of the surface wavy in the attenuation or amplification of sound and its intensity.

By use the Triple Deck theory we can seen that for fixed upstream Reynolds number , a change in the geometry will cause an associated change in the boundary layer at the leading edge of the cavity. So it is possible that sufficiently large changes in geometry may still indirectly effect the nature of the resonance through a change in the upstream boundary layer.

To fully understand the wavy surface impact on the cavity flow control, the following further work is required:

- Application of Multi-Objective Genetic Algorithm (MOGA)to determine the cavity acoustic control device parameters;
- Study the surface waviness effect on cavity acoustic at supersonic flow;
- Effects of landing gear door in cavity noise;
- Study the cavity noise with full Landing Gear;
- Wind Tunnel testing of an optimum 3D model.

BIBLIOGRAPHY

[1] *Fluent, urlhttp://www.ansys.com/products/ansys-fluent*, Official website, (2018).

[2] *General public licence, urlhttp://www.gnu.org/licenses/gpl-3.0.en.html*, Official website, (2018).

[3] *Openfoam, urlhttp://www.openfoam.com/*, Official website, (2018).

[4] *Star-cd, urlhttp://www.cd-adapco.com/products/star-cd*, Official website, (2018).

[5] K. AHUJA AND J. MENDOZA, *Effects of cavity dimensions, boundary layer, and temperature on cavity noise with emphasis on benchmark data to validate computational aeroacoustic codes*, (1995).

[6] A. J. BILANIN AND E. COVERT, *Estimation of possible excitation frequencies for shallow rectangular cavities.*, AIAA journal, 11 (1973), pp. 347–351.

[7] P. J. BLOCK, *Noise response of cavities of varying dimensions at subsonic speeds*, (1976).

[8] K. S. BRENTNER AND F. FARASSAT, *Modeling aerodynamically generated sound of helicopter rotors*, Progress in Aerospace Sciences, 39 (2003), pp. 83–120.

[9] G. B. BROWN, *The vortex motion causing edge tones*, Proceedings of the Physical Society, 49 (1937), p. 493.

[10] T. COLONIUS AND S. K. LELE, *Computational aeroacoustics: progress on nonlinear problems of sound generation*, Progress in Aerospace sciences, 40 (2004), pp. 345–416.

[11] J. COUSTEIX, J.-P. BRAZIER, AND J. MAUSS, *Perturbation tridimensionnelle d'une couche limite de blasius*, Comptes Rendus de l'Académie des Sciences-Series IIB-Mechanics, 329 (2001), pp. 213–219.

[12] J. COUSTEIX AND J. MAUSS, *Asymptotic analysis and boundary layers*, Springer Science & Business Media, 2007.

[13] N. CURLE, *The influence of solid boundaries upon aerodynamic sound*, Proceedings of the Royal Society of London. Series A. Mathematical and Physical Sciences, 231 (1955), pp. 505–514.

[14] R. DIX AND R. BAUER, *Experimental and predicted acoustic amplitudes in a rectangular cavity*, in 38th Aerospace Sciences Meeting and Exhibit, 2000, p. 472.

[15] D. DRIKAKIS, M. HAHN, A. MOSEDALE, AND B. THORNBER, *Large eddy simulation using high-resolution and high-order methods*, Philosophical Transactions of the Royal Society A: Mathematical, Physical and Engineering Sciences, 367 (2009), pp. 2985–2997.

[16] A. EPIKHIN, I. EVDOKIMOV, M. KRAPOSHIN, M. KALUGIN, AND S. STRIJHAK, *Development of a dynamic library for computational aeroacoustics applications using the openfoam open source package*, Procedia Computer Science, 66 (2015), pp. 150–157.

[17] ESDU, *Aerodynamics and aeroacoustics of rectangular planform cavities. part 1: Time averaged flow*, Data Item 02008 (2004).

[18] E.S.D.U, *Aerodynamics and aeroacoustics of rectangular planform cavities. part 2: Unsteady flow and aeroacoustics*, Data sheet 04023 (2005).

[19] F. FARASSANT, *Derivation of formulation 1 and 1a of farassant*, Tech., TM-2007-214853 (2007).

[20] J. FOX, *Flow regimes in transverse rectangular cavities.*, (1965).

[21] J. FOX, *A criterion for the transition between flow regimes in turbulent cavity flow.*, AIAA Journal, 4 (1966), pp. 364–365.

[22] T. GANDHI, *Numerical investigation of aeroacoustic interaction in the turbulent subsonic fow past an open cavity*, PhD thesis, Institut National Polytechnique de Toulouse, 2010.

[23] M. GHARIB AND A. ROSHKO, *The effect of flow oscillations on cavity drag*, Fluid Mech, 177 (1987), pp. 501–530.

[24] X. GLOERFELT, C. BOGEY, AND C. BAILLY, *Numerical investigation of the coexistence of multiple tones in flow-induced cavity noise*, in 9th AIAA/CEAS Aeroacoustics Conference and Exhibit, 2003, p. 3234.

[25] S. M. GRACE, W. G. DEWAR, AND D. E. WROBLEWSKI, *Experimental investigation of the flow characteristics within a shallow wall cavity for both laminar and turbulent upstream boundary layers*, Experiments in fluids, 36 (2004), pp. 791–804.

[26] F. F. GRINSTEIN, L. G. MARGOLIN, AND W. J. RIDER, *Implicit large eddy simulation: computing turbulent fluid dynamics*, Cambridge university press, 2007.

[27] H. HELLER, D. HOLMES, AND E. COVERT, *Flow-induced pressure oscillations in shallow cavities*, Sound Vib., 18 (1971), pp. 545–553.

[28] H. H. HELLER AND D. B. BLISS, *Flow-induced pressure fluctuations in cavities and concepts for their suppression*, Aeroacoustics: STOL Noise; Airframe and Airfoil Noise, 45 (1976), pp. 281–296.

[29] G. HUGHES, M. T., AND D. L., *Use of active surface waviness for control of cavity acoustics in subsonic flows*, 15 th AIAA/CEAS Aeroacoustics Conference (30th AIAA Aeroacoustics Conference), Miami ,Florida, AIAA-2009-3202 (2009).

[30] J. HUNT, *A theory for the laminar wake of a two-dimensional body in a boundary layer*, Journal of Fluid Mechanics, 49 (1971), pp. 159–178.

[31] C. E. JOBE AND O. BURGGRAF, *The numerical solution of the asymptotic equations of trailing edge flow*, Proceedings of the Royal Society of London. A. Mathematical and Physical Sciences, 340 (1974), pp. 91–111.

[32] K. KARAMCHETI, *Acoustic radiation from two-dimensional rectangular cutouts in aerodynamic surfaces*, NACA-TN-3487 (1955), p. 17.

[33] K. KARAMCHETI, *Sound radiation from surface cutouts in high speed flow*, PhD thesis, California Institute of Technology, 1956.

[34] G. KOROLEV, J. GAJJAR, AND A. RUBAN, *Once again on the supersonic flow separation near a corner*, Journal of Fluid Mechanics, 463 (2002), pp. 173–199.

[35] M. KOROTEEV AND I. LIPATOV, *Supersonic boundary layer in regions with small temperature perturbations on the wall*, SIAM Journal on Applied Mathematics, 70 (2009), pp. 1139–1156.

[36] M. KOROTEEV AND I. LIPATOV, *Local temperature perturbations of the boundary layer in the regime of free viscous–inviscid interaction*, Journal of Fluid Mechanics, 707 (2012), pp. 595–605.

[37] M. KOROTEYEV AND I. LIPATOV, *Steady subsonic boundary layer in domains of local surface heating*, Journal of Applied Mathematics and Mechanics, 77 (2013), pp. 486–493.

[38] M. A. KRAVTSOVA, V. B. ZAMETAEV, AND A. I. RUBAN, *An effective numerical method for solving viscous–inviscid interaction problems*, Philosophical Transactions of the Royal Society A: Mathematical, Physical and Engineering Sciences, 363 (2005), pp. 1157–1167.

[39] K. KRISHNAMURTY, *Acoustic radiation from two-dimensional rectangular cutouts in aerodynamic surfaces*, (1955).

[40] M. J. LIGHTHILL, *On sound generated aerodynamically i. general theory*, Proceedings of the Royal Society of London. Series A. Mathematical and Physical Sciences, 211 (1952), pp. 564–587.

[41] M. J. LIGHTHILL, *On boundary layers and upstream influence ii. supersonic flows without separation*, Proceedings of the Royal Society of London. Series A. Mathematical and Physical Sciences, 217 (1953), pp. 478–507.

[42] I. LIPATOV, *Disturbed boundary layer flow with local time-dependent surface heating*, Fluid Dynamics, 41 (2006), pp. 725–735.

[43] T. MAUREEN B AND P. EB, *Cavity unsteady-pressure measurements at subsonic and transonic speeds*, (1997).

[44] G. MENGALDO, M. KRAVTSOVA, A. RUBAN, AND S. SHERWIN, *Triple-deck and direct numerical simulation analyses of high-speed subsonic flows past a roughness element*, Journal of Fluid Mechanics, 774 (2015), pp. 311–323.

[45] A. MESSITER, *Boundary-layer flow near the trailing edge of a flat plate*, SIAM Journal on Applied Mathematics, 18 (1970), pp. 241–257.

[46] S. V. PATANKAR AND D. B. SPALDING, *A calculation procedure for heat, mass and momentum transfer in three-dimensional parabolic flows*, in Numerical Prediction of Flow, Heat Transfer, Turbulence and Combustion, Elsevier, 1983, pp. 54–73.

[47] E. B. PLENTOVICH, *Three-dimensional cavity flow fields at subsonic and transonic speeds*, (1990).

[48] E. B. PLENTOVICH, R. L. STALLINGS JR, AND M. B. TRACY, *Experimental cavity pressure measurements at subsonic and transonic speeds. static-pressure results*, (1993).

[49] H. PLUMBLEE, J. GIBSON, AND L. LASSITER, *A theoretical and experimental investigation of the acoustic response of cavities in an aerodynamic flow*, tech. report, LOCKHEED AIRCRAFT CORP MARIETTA GA, 1962.

[50] D. ROCKWELL AND C. KNISELY, *Vortex-edge interaction: Mechanisms for generating low frequency components*, The Physics of Fluids, 23 (1980), pp. 239–240.

[51] D. ROCKWELL AND E. NAUDASCHER, *Self-sustaining oscillations of flow past cavities*, Journal of Fluids Engineering, 100 (1978), pp. 152–165.

[52] C. ROGET, J. P. BRAZIER, J. COUSTEIX, AND J. MAUSS, *A contribution to the physical analysis of separated flows past three-dimensional humps*, European Journal of Mechanics-B/Fluids, 17 (1998), pp. 307–329.

[53] A. ROSHKO, *Some measurements of flow in a rectangular cutout*, 3488 (1955).

[54] J. ROSSITER, *Wind tunnel experiments on the flow over rectangular cavities at subsonic and transonic speeds*, tech. report, Ministry of Aviation; Royal Aircraft Establishment; RAE Farnborough, 1964.

[55] C. W. ROWLEY, *Modeling, simulation, and control of cavity flow oscillations*, PhD thesis, California Institute of Technology, 2002.

[56] C. W. ROWLEY, T. COLONIUS, AND A. J. BASU, *On self-sustained oscillations in two-dimensional compressible flow over rectangular cavities*, Journal of Fluid Mechanics, 455 (2002), pp. 315–346.

[57] V. SAROHIA, *Experimental and analytical investigation of oscillations in flows over cavities*, PhD thesis, California Institute of Technology, 1975.

[58] W. SCHNEIDER, *Upstream propagation of unsteady disturbances in supersonic boundary layers*, Journal of Fluid Mechanics, 63 (1974), pp. 465–485.

[59] C. SHIEH AND P. MORRIS, *Parallel computational aeroacoustic simulation of turbulent subsonic cavity flow*, in 6th Aeroacoustics Conference and Exhibit, 2000, p. 1914.

[60] F. SMITH, P. BRIGHTON, P. JACKSON, AND J. HUNT, *On boundary-layer flow past two-dimensional obstacles*, Journal of Fluid Mechanics, 113 (1981), pp. 123–152.

[61] S. SRINIVASAN AND O. BAYSAL, *Navier-stokes calculations of transonic flows past cavities*, Journal of Fluids Engineering, 113 (1991), pp. 368–376.

[62] S. SRINIVASAN, O. BAYSAL, AND E. PLENTOVICH, *Navier-stokes calculations of transonic flows past open and transitional cavities*, (1988).

[63] R. L. STALLINGS JR AND F. J. WILCOX JR, *Experimental cavity pressure distributions at supersonic speeds*, (1987).

[64] K. STEWARTSON, *On the flow near the trailing edge of a flat plate ii*, Mathematika, 16 (1969), pp. 106–121.

[65] K. STEWARTSON AND P. WILIAMS, *Self-induced separation. proc. roy. soc. a., 312*, (1969).

[66] V. SUPONITSKY, E. AVITAL, AND M. GASTER, *On three-dimensionality and control of incompressible cavity flow*, Physics of Fluids, 17 (2005), p. 104103.

[67] V. V. SYCHEV, V. V. SYČËV, V. V. SYCHEV, A. I. RUBAN, AND G. L. KOROLEV, *Asymptotic theory of separated flows*, Cambridge University Press, 1998.

[68] B. THORNBER AND D. DRIKAKIS, *Implicit large-eddy simulation of a deep cavity using high-resolution methods*, AIAA journal, 46 (2008), pp. 2634–2645.

[69] M. B. TRACY, E. B. PLENTOVICH, AND J. CHU, *Measurements of fluctuating pressure in a rectangular cavity in transonic flow at high reynolds numbers*, (1992).

[70] H. VERSTEEG AND W. MALALASEKERA, *An introduction to computational fluid dynamics prentice hall*, (1995).

[71] M. WANG, J. B. FREUND, AND S. K. LELE, *Computational prediction of flow-generated sound*, Annu. Rev. Fluid Mech., 38 (2006), pp. 483–512.

[72] A. YOSHIZAWA, *Statistical theory for compressible turbulent shear flows, with the application to subgrid modeling*, The Physics of fluids, 29 (1986), pp. 2152–2164.

[73] R. K. ZEYTOUNIAN, *Theory and applications of viscous fluid flows*, (2004).